AFYON KOCATEPE ÜNİVERSİTESİ

e-ISSN: 2667-4165 • CİLT / VOLUME: II • SAYI / ISSUE: I • HAZİRAN / JUNE 2019

ULUSLARARASI MÜHENDİSLİK TEKNOLOJİLERİ VE UYGULAMALI BİLİMLER DERGİSİ

International Journal of Engineering Technology and Applied Sciences

www.ijetas.aku.edu.tr

AFYON KOCATEPE ÜNİVERSİTESİ
ULUSLARARASI MÜHENDİSLİK TEKNOLOJİLERİ ve UYGULAMALI BİLİMLER DERGİSİ
Afyon Kocatepe University
International Journal of Engineering Technology and Applied Sciences

Afyon Kocatepe University International Journal of Engineering Technology and Applied Sciences

www.ijetas.aku.edu.tr

e-ISSN:2667-4165

Afyon Kocatepe University
International Journal of Engineering Technology and Applied Sciences (AKU-IJETAS)

Volume: 2 / Number: 1 / June - 2019

Owner / Publisher: Rector Prof. Dr. Mehmet KARAKAŞ for Afyon Kocatepe University

Chief in Chief Prof. Dr. Ayhan EROL

Co- Editor in Chief Assist. Prof. Dr. Ahmet YÖNETKEN

Published Afyon Kocatepe University, June 2019,

ijetas@aku.edu.tr

This work is subject to copyright. All rights are reserved, whether the whole or part of the material is concerned. Nothing from this publication may be translated, reproduced, stored in a computerized system or published in any form or in any manner, including, but not limited to electronic, mechanical, reprographic or photographic, without prior written permission from the Publisher Afyon Kocatepe University www.ijetas.aku.edu.tr ijetas@aku.edu.tr The individual contributions in this publication and any liabilities arising from them remain the responsibility of the authors. The publisher is not responsible for possible damages, which could be a result of content derived from this publication.

CONTACT INFORMATION

Afyon Kocatepe University International Journal of Engineering Technology and Applied Science Afyon Kocatepe University, Technology Faculty, 03200 Afyonkarahisar, TURKEY

Phone: +90-272-2281446 /ext.

Fax: +90-272 228 1449

e-mail : ijetas@aku.edu.tr, aerol@aku.edu.tr

Welcome to AKU-IJETAS

Dear Researchers;

International Journal of Engineering and Applied Sciences ler has been published in Turkish and English since 2018 with 2 issues. Our journal will accept Turkish and English articles as 2 issues a year and the articles will be evaluated by at least two referees with the same system. Our magazine from December 2018; it offers many advantages to readers due to the practical and practical access to the authors as well as the process of publishing and publishing quickly and easily; The electronic journal (e-ISSN:2667-4165) accepts 2 numbers per year (June and December) in Turkish and English. The names of the judges evaluating the articles are not notified to the authors. The referees cannot see the names of the authors. The studies are evaluated as at least two referees. Our authors, who want to send articles, can register their original scientific articles online and follow the process by registering on our magazine page. Our journal is accepted as original and previously published research articles.

We are waiting for your contributions as both referee and writer. I thank you in advance for your support and I wish you success in your work.

Prof. Dr Ayhan EROL

Chief Editor

Danışma Kurulu / Editörler/ Editorial Board

Adem KURT	Gazi University	TURKEY
Ahmet AKSOY	Akdeniz University	TURKEY
Ahmet YILDIZ	Afyon Kocatepe University	TURKEY
Alexander ONUFRAK	Pavol Jozef Safarik University	SLOVAKIA
Anas Sarwar QURESHI	Agriculture University	PAKISTAN
Artay YAGCI	Afyon Kocatepe University	TURKEY
Asım Gokhan YETGIN	Dumlupinar University	TURKEY
Aytekin HITIT	Afyon Kocatepe University	TURKEY
Behçet GULENC	Gazi University	TURKEY
Bojan ZLENDER	Maribor University	SLOVENIA
Cahit GURER	Afyon Kocatepe University,	TURKEY
Dinçer BURAN	Süleyman Demirel University	TURKEY
Dunja PERIC	Kansas State University, Manhattan	ABD
Dusan ORAC	Kosice Technical University	SLOVAKIA
Elena Cristina RADA	Trento University	ITALY
Gabor PAY	University College of Nyiregyhaza	HUNGARY
Gratiela BOCA DANA	Technical University Cluj Napoca	ROMANIA
Hazizan Md AKİL	Sains Malaysia University	MALAYSIA
Huseyin Ali YALIM	Afyon Kocatepe University	TURKEY
Huseyin AKBULUT	Afyon Kocatepe University	TURKEY
Huseyin BAYRAKCEKEN	Afyon Kocatepe University	TURKEY
Ilhan KOŞALAY	Ankara University	TURKEY
Ioan ABRUDAN	Technical University Cluj Napoca	ROMANIA
Ivan KURIK,	Technical University Zilina	SLOVAKIA
Iveta VASKOVA	Kosice Technical University	SLOVAKIA
João Pedro SILVA	Leiria Polytechnic Institute	PORTUGAL
Lucian Ionel CIOCA	Lucian Blaga University of Sibiu	ROMANIA
Marco RAGAZZI	Trento University	ITALY
Martina HRUBOVCAKOVA	Kosice Technical University	SLOVAKIA
Matjaž ŠRAML	Maribor University	SLOVENIA
Merlinda EBIBI	Mother Teresa University	MACEDONIA
Metin OZGUL	Afyon Kocatepe University	TURKEY
Mihai BANICA	Technical University Cluj Napoca	ROMANIA
Mircea HORGOS	Technical University Cluj Napoca	ROMANIA
Monica Lopez ALONSO	University of GRANADA	SPAIN
Muhammed YURUSOY	Afyon Kocatepe University	TURKEY
Mustafa ERSOZ	University of Selcuk	TURKEY
Mustafa TÜRKMEN	Kocaeli University	TURKEY
Mustaque HOSSAIN	Kansas State University, Manhattan	ABD
Nadras OTHMAN	Sains University	MALAYSIA
Nicolae UNGUREANU	Technical University Cluj Napoca	ROMANIA

Neritan TURKESHI	Mother Teresa University	MACEDONIA
Olivera PETKOVSKA	Mother Teresa University	MACEDONIA
Olga OROSOVA	Pavol Jozef Safarik University	SLOVAKIA
Otar ZUMBURIDZE	GeorgiaTechnical University	GEORGIA
P. Trinatha RAO	Gitam University	INDIA
Peter MONKA	Technical University Kosice	SLOVAKIA
Prasanna RAMAKRISNAN	Neo Education Institu	MALAYSIA
Ramazan KAÇAR	Karabük University	TURKEY
Radu COTETIU	Technical University Cluj Napoca	ROMANIA
Regita BENDIKIENĖ	Kaunas Technology University	LİTVANIA
Renata PANOCOVA	Pavol Jozef Safarik Üniversity	SLOVAKIA
Rıdvan UNAL	Usak University	TURKEY
Robert CEP	Technical University Ostrava	CZECH
Selçuk AKTURK	Mugla University	TURKEY
Serdar SALMAN	Marmara University	TURKEY
Serhat BASPINAR	Afyon Kocatepe University	TURKEY
Sermin OZAN	Fırat University	TURKEY
Sezai TAŞKIN	Celal Bayar University	TURKEY
Suleyman GUNDUZ	Karabük University	TURKEY
Sukru TALAS	Afyon Kocatepe University	TURKEY
Stanislaw LEGUTKO	Poznan University of Technology	POLAND
Tomasz NIZNIKOWSKI	Lomza State University Applied Science	POLAND
Tomaz TOLLAZZI	Maribor University	SLOVENIA
Ugur CALIGULU	Firat University	TURKEY
Yılmaz YALCIN	Afyon Kocatepe University	TURKEY
Yuksel OĞUZ	Afyon Kocatepe University	TURKEY
Zeynep OMEROGULLAR	Usak University	TURKEY
Zoran TRIFUNOV	Mother Teresa University	MACEDONIA

CONTENTS

Afyon Kocatepe Üniversitesi Uluslararası Mühendislik Teknolojileri ve Uygulamalı Bilimler Dergisi

Afyon Kocatepe University International Journal of Engineering Technology and Applied Sciences

AKÜ IJETASSayı**2**(2019) Haziran (1-9 s) AKU J.Eng.App.Sci. **Vol 2** (2019) June (1-9 pp)

Araştırma Makalesi / ResearchArticle

Taşınabilir Manyetik Nanoparçacık Spektrometresi

Yeşim Akyürekli[1], Cengiz Akay[2], Elif Uzak[3], Adem Tunçdamar[4]

[1, 2, 3] *Bursa Uludağ Üniversitesi, Fen Edebiyat Fakültesi, Atom ve Molekül Fiziği Anabilim Dalı, 16059 Görükle, Bursa*

[4] *Bursa Uludağ Üniversitesi, Fen Edebiyat Fakültesi, Fizik Bölümü, 16059 Görükle, Bursa*

[1]*beroocan12@gmail.com*

[2]*cenay.akay@gmail.com*

[3]*elifuzak16@gmail.com*

[4] *ademtuncdamarr@gmail.com*

Geliş Tarihi:07.03.2019 ; Kabul Tarihi:29.03.2019

Anahtar kelimeler
Manyetik parçacık spektrometresi; Manyetik nanoparçacık parametreleri, Doğrusal olmayan mıknatıslanma; FFT; Veri analizi

Özet

Manyetik parçacık spektrometresi (MPS), belirli manyetik alan değerlerinde süper paramanyetik demir oksit nanoparçacıklarının doğrusal olmayan tepkisini ve manyetik doygunluğunu kullanır. Zamanla değişen bir manyetik uyarıcı bobinlerin alanı parçacıkların mıknatıslanmasının maksimum ve minimum değer arasında değişmesine neden olur. Genel olarak, uygulanan alan geçici olarak değiştirildiğinde manyetik bir nanoparçacığın yönünü değiştirmenin iki yolu vardır. Parçacığın kendisi Brownian dönüşü adı verilen fiziksel bir dönüş gerçekleştirir veya parçacık içindeki manyetik moment Néel dönüşü adı verilen sabit bir yapıda dönebilir. Viskoz bir ortamda, uygulanan frekansa bağlı olan ve baskın bir işlem olan her iki dönme tipinin kombinasyonu gerçekleşir. Relaksometre olarak da bilinen bu sistem, MPS çalışmalarındaki manyetik nanoparçacıkların yoğunluğunu ve ilgili hesaplamaları yaparak nanoparçacıklarındurulma sürelerinin ölçümünü dikkate alır. Brownian veya Néeldurulma süreleri, kimyasal olarak bağlı veya bağlı olmayan manyetik nanoparçacıkların dış değişken manyetik alana verdiği tepkiye göre hesaplanabilir. Bu çalışmada, nanoparçacıkların durulma zamanları gibi özelliklerinin analiz edilmesini sağlayan bir spektrometre öncelikle tasarlanmış ve yapımı gerçekleştirilmiştir Spektrometreden elde edilen MPS sinyalleri veri toplama kartı ile bilgisayara aktarılabilir ve Python programlama dilinde yazılmış bir yazılımla veri analizi yapılabilir.

Portable Magnetic Nanoparticle Spectrometer

Keywords
Magnetic particle spectrometer;Magnetic nanoparticles Parameters;Nonlinear magnetization; FFT;Data analysis

Abstract

The magnetic particle spectrometer (MPS) uses the nonlinear response of super-paramagnetic iron oxide nanoparticles and magnetic saturation at certain magnetic field values. A time-varying magnetic field of excitation coils causes the magnetization of the particles to vary between the maximum and the minimum value. Generally, there are two ways in which a magnetic nanoparticle can change the direction when the applied area is temporarily changed. The particle itself performs a physical rotation called the Brown return, or the magnetic moment in the particle can rotate in a fixed structure called the Néel return. In a viscous environment, the combination of both types of rotation takes place, which depends on the frequency applied and is a dominant process. This system, also known as the relaxometer, takes into account the density of the magnetic nanoparticles in the MPS studies and the measurement of the relaxation times of the nanoparticles by making the corresponding calculations. Brownian or Néelrelaxation times can be calculated according to the reaction of chemically bound or unbound magnetic nanoparticles to the external variable magnetic field. In this study, a spectrometer was first designed and constructed to analyze the properties of nanoparticles such as relaxation times. MPS signals obtained from the spectrometer can be transferred to the computer with data acquisition card and data analysis can be done with a software written in python programming language.

© Afyon Kocatepe Üniversitesi

1. Introduction

Magnetic particle imaging (MPI), which displays the spatial distribution of super paramagnetic iron oxide nanoparticles, is a new tomographic imaging technique. In this technique, the signal is taken from the iron oxide nanoparticles, which are characterized as tracers. Monitoring the quality of these tracers is important for tissue health, and studies in this area are not yet enough. Based on nonlinear magnetization of magnetic nanoparticles, MPS can accurately measure the high-level harmonic components of the signals it detects with the spectral analysis method. In general, these signals are analyzed using the Langevin function model, which is expanded by a Debye front factor that defines the dynamic magnetic properties of the particles [1]-[2]-[3]. However, this model is a coarse approach that has not only correctly defined the phase of the harmonics [8]. In this study, a magnetic particle spectrometer can be interpreted as a zero-sized MPI scanner containing a drive field coil and a receiver coil. The following sections describe the current setup that can perform MPS measurements with a freely adjustable excitation frequency in the range of 1 kHz to 10 kHz. This setup demonstrates the possibility of identifying the different properties of nanoparticles, such as the effect of Brownian and Néel rotation on signal quality.

2. Methods

MPI relies on the non-linear magnetization curve of magnetic nanoparticles. When a time varying magnetic field $H(t) = H_0 \sin(2\pi f_0 t)$ is applied to the nano-particles, a magnetization *M(H(t))* is observed. Due to the non-linearity of M, the frequency spectrum of the magnetization response does not only consist of the frequency f_0, but also of higher harmonics. Figure 1 shows this process, response of magnetic particles to an external magnetic field theory of nonlinear magnetization [5].

According to the Langevin theory of paramagnetism [6], the magnetization curve of the particles can be described by

$$M(t) = m_s c \left(\coth\left(\frac{m_s \mu_0 H(t)}{k_B T}\right) - \frac{k_B T}{m_s \mu_0 H(t)} \right) \quad (1)$$

where μ_0 denotes the permeability of vacuum, k_B the Boltzmann constant, T the temperature as Kelvin, c the sample concentration, and $m_s = \frac{1}{6} D^3 M_s$ the magnetic moment of the particles at saturation [7]. The particles are characterized by their diameter D and the saturation magnetization M_s [8]. In eq. (1) it is assumed that the concentration c of the nanoparticles is homogeneous within the probe. Furthermore, the magnetic field $H(t)$ is nearly homogeneous in the probe chamber and has only one spatial component. This can be achieved by using a solenoid coil to generate the magnetic field, where the probe chamber lays inside the coil.

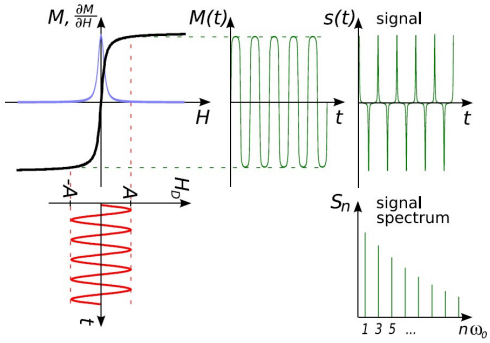

Figure 1. Basic MPI principle. The drive field $H(t)$ generates a particle response $M(t)$ that induces a voltage in the receive coils. The time-dependent voltage is measured and constitutes the raw signals $s(t) \propto d M(t)/dt$. Due to the non-linear magnetization curve, the signal spectrum S_n contains higher harmonics of the drive frequency f_0, which are used for particle detection and imaging. For reference, the derivative of the magnetization curve $\partial M/\partial H$ is also shown (blue curve).

3. Materials and Equipment

Magnetic nanoparticle detector assembly consists of the following components; function signal generator, power amplifier, band-pass filter, coil system, band stop filter, signal amplifier, data acquisition card and PC, Figure 2.

3.1 Function signal generator

Signal generator must be generate a desired frequency sinusoidal signal with constant amplitude and does not contain any harmoniccomponent. Figure 3 shows the complete schematic of the sinus generator performed. The XR-2206 is a function generator that produces high quality sinus, square, triangle, ramp and pulse waves with high stability and accuracy. The amplitude and frequency of the output waveforms can also be modified by an external voltage to be applied. The operating frequency can be selected externally in a range of 0.01 Hz to 1 MHz [9]. The frequency is given as follows:

$$f_0 = \frac{1}{2\pi RC} \quad (Hz) \qquad (2)$$

The sinusoidal generator produces the sinusoidal signal so perfectly that the bandpass filter shown in figure 1 is not used in this study.

3.2Power amplifier

Since the function generator's output signal is not powerful enough to make excitation coil produce oscillation magnetic field with a certain amplitude, power amplifier is necessary for the detection. The output of the power amplifier must be linear and bandwidth wide enough. Figure 4 shows a power amplifier with TDA2050 integrated circuit in this study. The TDA2050 heats up excessively at high currents and is mounted on a fan cooler. According to the manufacturer's data of the TDA2050 integrated circuit, the maximum permissible current value of this unit is limited to 5 A, which can deliver 50 W of output power [10]. The 35 VDC supply source of the cooling fan must be independent of the supply source, otherwise unwanted harmonics may leak into the output of this power amplifier

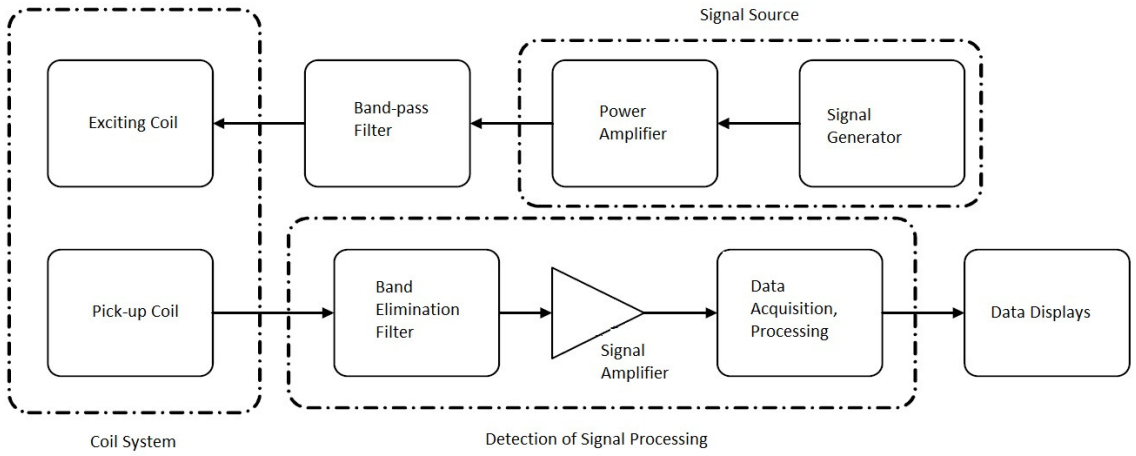

Figure 2. The system schematic of magnetic nanoparticles detection.

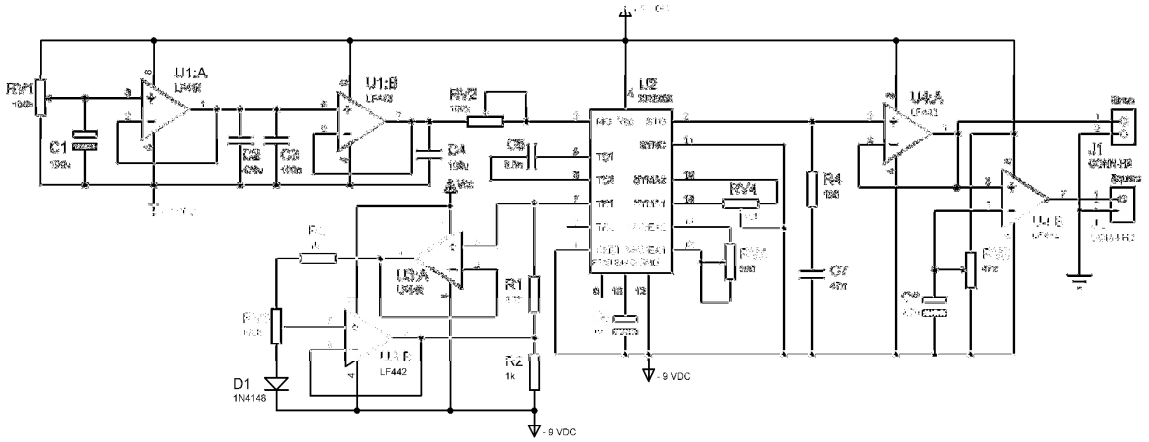

Figure 3. Sinus signal generator with XR2206

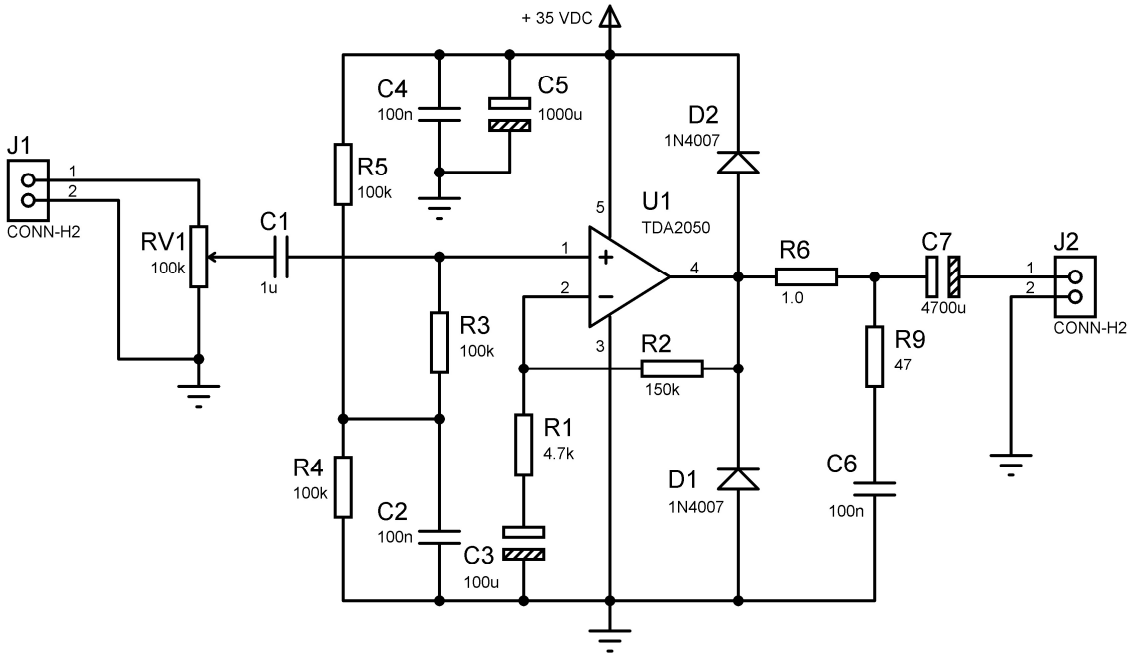

Figure 4. Current drive power amplifier with TDA2050

3.3Band-pass filter

To ensure that the output signal from the detection coil contains only harmonics, a band stop filter should be connected to the output of the detection coil in series. Since the main purpose is to prevent the base band signals, it can be accomplished using high-pass filter or twin t notch filter. Figure 5 shows a twin notch filter made in this study. A notch filter,also known as band limiting circuits, can be used to remove a particular frequency. It is usually fixedfrequency, but some of the notch frequency can be adjusted. Due to the high Q value, the bandwidth

of these filters is very small. An ideal notch filter should give a smooth frequency response on all other frequencies, except for the notch frequency.

In reality, perfection cannot be achieved, but when used with operational amplifier cores, high attenuation and narrow notches can be achieved [11].

3.4 Lownoiseamplifier

It is not possible to perceive because of the amplitude of the MPS signal containing the harmonic frequencies is too small. The output impedance of the gradiometer receiver coil must match the input impedance of the data acquisition board.It is an important solution to improve signal/noise ratio by selecting appropriate electronic design and its components. Figure 6 shows the preamplifier circuit consisting of integrated two operational amplifiers.

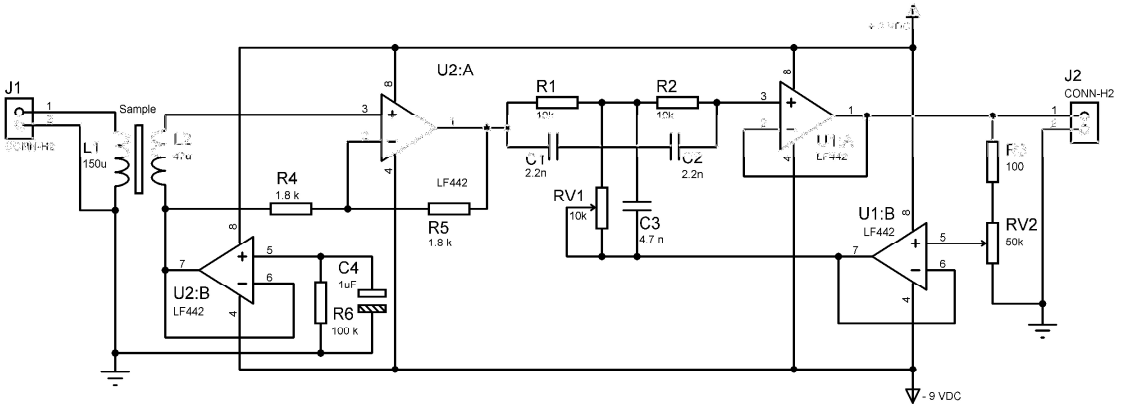

Figure 5. Twin t notch filter with buffers. L1 and L2 are the transmitting and gradiometer receiving coils, respectively

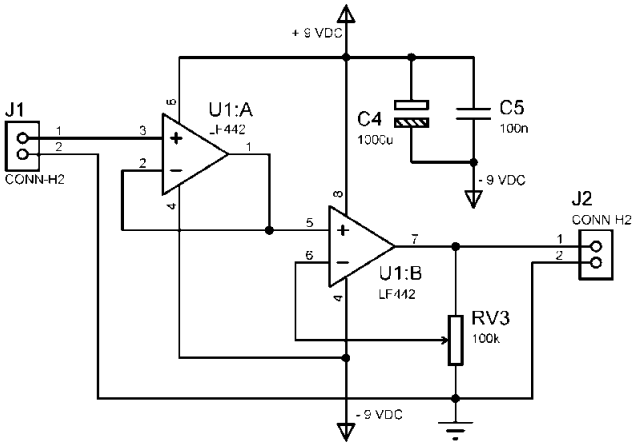

Figure 6. Operational trans conductance amplifier.

In the first, the unit gain is the monitor, in a sense the impedance converter and the output signal monitors the input signal. The second one is the unit that performs the actual amplification of the input signal and is known in the terminology as “operational trans conductance amplifier, (OTA)" [12].The notch filter and the preamplifier together form a signal conditioner. The conditioner amplifies the very small MPS signals sufficiently enough to transmit the signal to the data acquisition card with an improved signal to noise ratio.

3.5 Data acquisitionandprocessing

MPS signals are analog signals and must be converted to digital data encoded in a binary number system in order to process these signals. For this purpose, the sound card embedded in the motherboard of a laptop and the Pythonprogramming language were used to access this sound card. The numerical data obtained from the sound card can be stored and converted into a database with a software written in this language.

3.6 Coilsystem

As mentioned earlier, MPS uses the nonlinear response of super paramagnetic nanoparticles and magnetic saturation in certain magnetic fields, which is why the coil system is required to stimulate nanoparticles and detect their response. Figure 7 shows the coil system consisting of transmitter/driver and gradiometer receiver coil. The upper coil is the driver coil. This coil causes the nanoparticles to be excited by turning the high frequency currents having the known frequency and sufficiently large amplitude into the magneticfield. The inductance of thiscoil made by winding a thin wire on a carcass can be calculated from the following relation:

$$L = \frac{0.8\,\mathcal{N}^2 r^2}{6r + 9.\ell + c} \quad (\mu H) \qquad (3)$$

Here, N is the number of turns, r is the radius of the coil, ℓ is the length of the coil, and c is the thickness of the coil. Units must be taken in mm. The Biot-Savart law can calculate the magnitude of the magnetic field generated by the high frequency current passing through these two solenoid coils along the axis of the coil as

$$H(t) = \frac{N}{2\sqrt{(l/2)^2 + r^2}}\, i(t) \quad A/m \quad (4)$$

The last expression is the rearranged version of the same law and $i(t)$is the value of the current flowing through the coil [1]. In Figure 7, the left-most coil is the gradiometer receiver coil.The windings on both ends of the coil have the same number of turns and winding the same direction.

The total number of windings of both ends is equal to the number of windings of the middle coilbut wound in the opposite direction. Coils with these properties are known as gradiometer or differential coils. This is very important in the MPS study because the amplitude of the excitation signal induced in the receiver coil is much larger than the signal of the nanoparticles,suppressing the signal of the particles and therefore the gradient coil is used to remove thesignal that is caused by the excitation [16].The number of turns of the gradiometer coil made in the study was wrapped around 47 turns for the windings at both ends, 94 for the middle windings but in the reverse direction. In addition, the receiver coil should be placed concentrically inside the exciter coil, and the capsule containing the nanoparticles to be measured should be placed in the middle of this receiver coil. In addition, the drive coil was wound with aluminum foil and grounded. In the thumbnail, there is a superparamagnetic iron oxide Fe_3O_4 solution in the capsule (nanomag® - MIP, surface: NH_2, Size: 100 nm, c(Fe) = 5.0 g/ml).

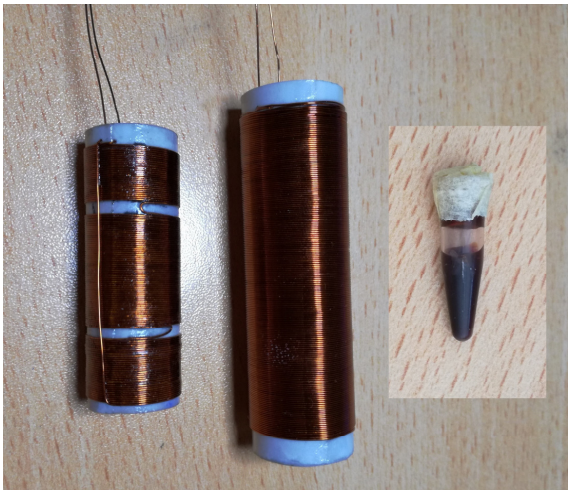

Figure 7. The coil system consisting of transmitter / driver and gradiometer receiver coil.

The accuracy of the signals of super paramagnetic nanoparticles detected in this system as described above for each component was obtained after calibration of the whole system. After ensuring correctness, the obtained signals can be displayed as a spectrum on the screen by performing Fourier transform. The signal flow of the system is shown in Figure 8.

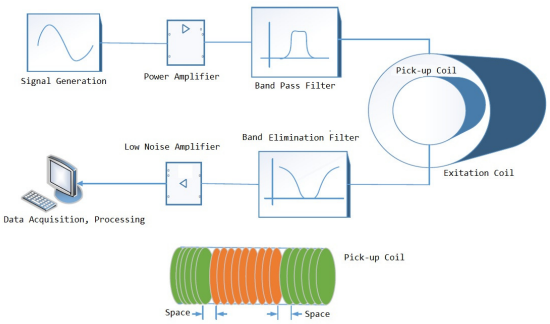

Figure 8. The signal flow of the system.

4.Measurements andResults

Figure 9 shows the finished state of the spectrometer; the operating frequency is 1.556 kHz and this value can be changed according to the expression (2). Figure 10 is a view of the MPS signal received in this spectrometer.

According to the signal processing theory, the sampling frequency must be at least twice as large as the frequency of the signal to be digitized. The sampling frequencies of the sound card we use can be changed via software. In this study, MPS signals obtained with 16 kHz and 38 kHz sampling frequencies and their FFT transformations are given in Figure 11 and Figure 12. The codes used for the FFT conversion of the MPS signal were written in Python version 3.6.8.

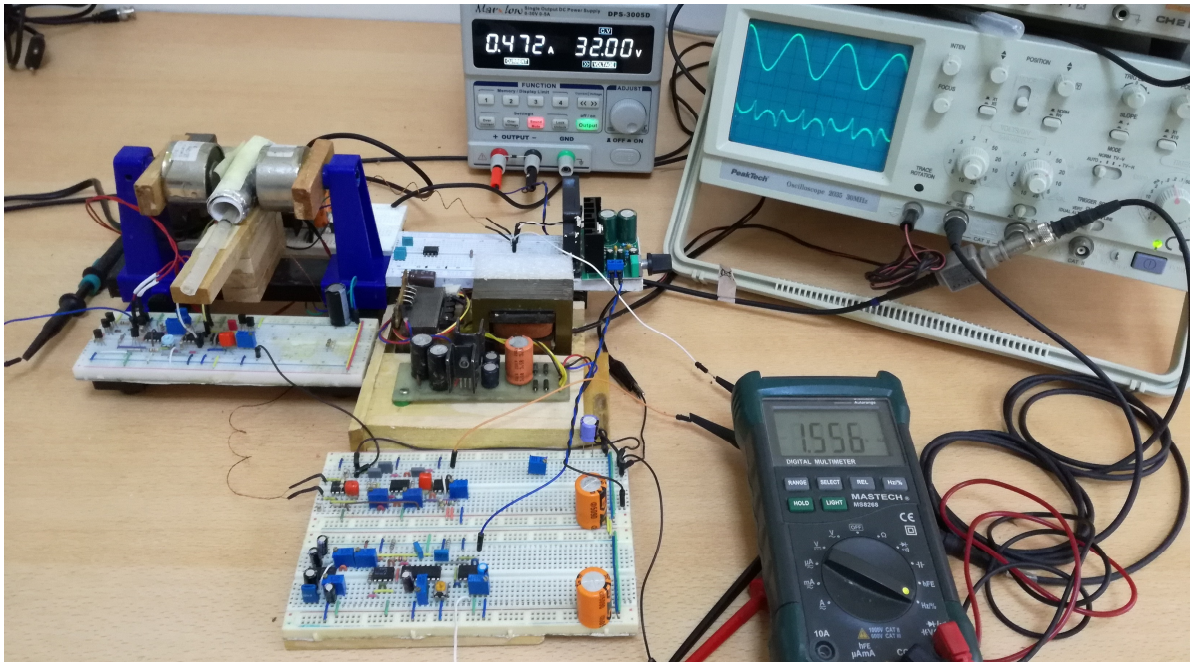

Figure 9. Magnetic nanoparticle detection system based on a sound card embedded on a laptop.

The values of the FFT peaks obtained from both sampling frequencies are the same and these peak values are the monovalent harmonic components of the fundamental frequency matching the nanoparticles. Table 1 summarizes these values and the graph is given in Figure 13.

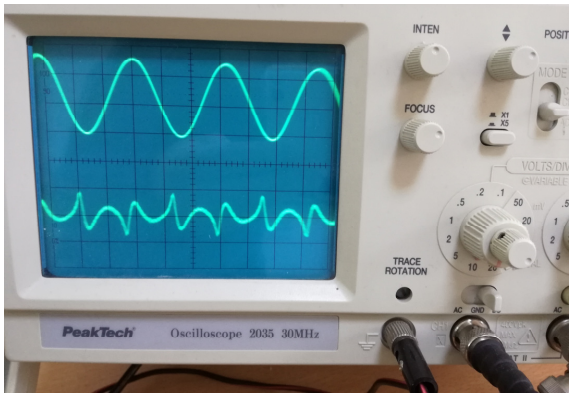

Figure 10. Observed MPS signal

In Figure 13, the upper end of the exponential curve obtained because of the graphical adaptation of the FFT peak points is cut off since the first harmonic in the particle spectrum cannot be used because the band stop filter suppresses the basic frequency.

Table 1. FFT peak values.

Odd frequency harmonics		
2n-1	**Frequencies (kHz)**	**Peaks (dB)**
1f	1.556	4.1856
3f	4.668	2.0750
5f	7.780	1.3899
7f	10.892	0.6984
9f	14.004	0.4199
11f	17.116	0.2264

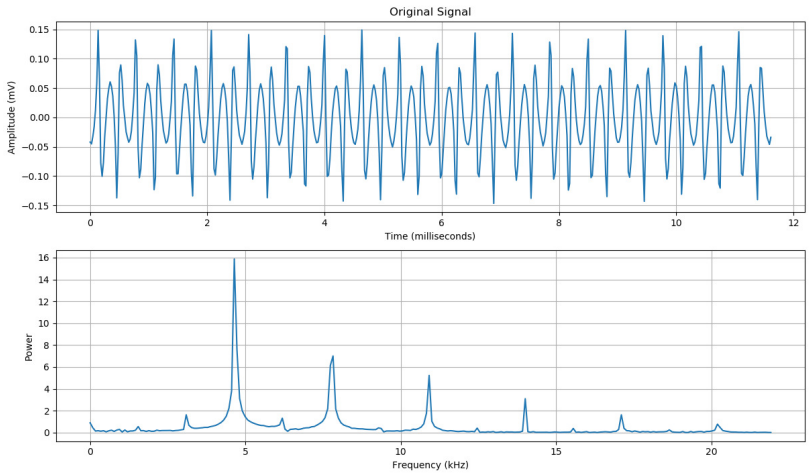

Figure 11. 16 KHz sampled MPS signal and FFT

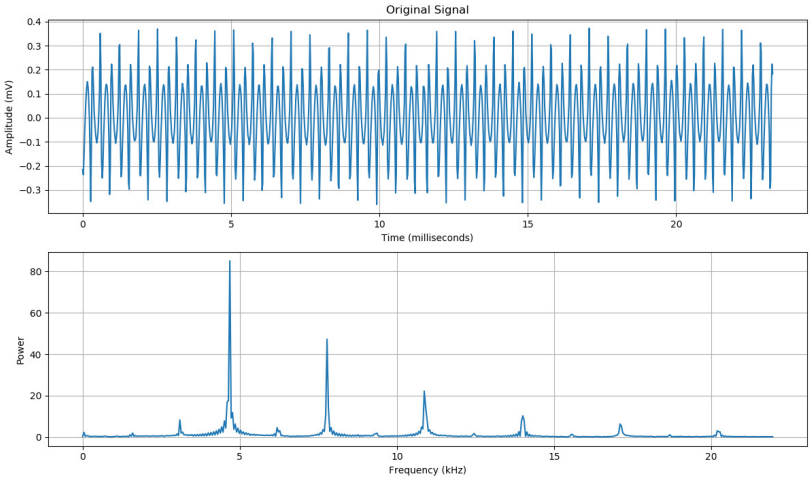

Figure 12. 38 KHz sampled MPS signal and FFT

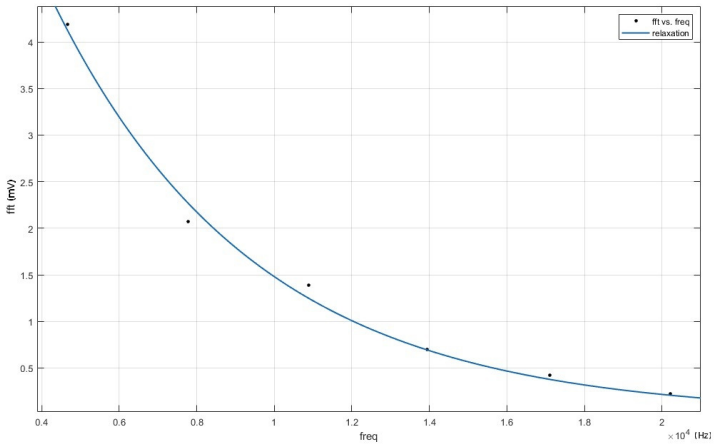

Figure 13. Frequency spectrum decays exponentially with increasing frequency.

5. Conclusions

In this study, the MPS system which is designed and experimentally performed can be interpreted as a zero-dimensional MPI scanner. This system needs to be developed to detect small diameter and low magnetic nanoparticle concentrations. This requires software algorithms with high quality hardware circuits. It also allows the creation of a database in the following stages. As a result, this experimental magnetic particle spectrometer (MPS) is a useful tool for real-time monitoring of its suitability during particle synthesis and for monitoring the imaging quality of the particle.

6. References

Articles

Yan Tan, Yang Yu, Xing Lv, Ming Wang. Design and Simulation of Magnetic Nanoparticles Detector Based on the Nonlinear Magnetization, 2013 6th International Conference on Biomedical Engineering and Informatics (BMEI 2013).

André Behrends, Matthias Graeser and Thorsten M. Buzug. Introducing a frequency-tunable magnetic particle spectrometer, De Gruyyer, Current Directions in Biomedical Engineering 2015; 1:249–253.

Ferguson RM, Khandhar AP, Hamed A, Loc H, Hovorka O, Krishnan KM. Tailoring the magnetic and pharmacokinetic properties of iron oxide magnetic particle imaging tracers. Biomedical Engineering/Biomedizinische Technik 2013; 58(6): 493–507.

Jürgen Rahmer, Jürgen Weizenecker, Bernhard Gleich and JörnBorgert. Signal encoding in magnetic particle imaging: properties of the system function. BMC Medical Imaging 2009, 9:4 doi:10.1186/1471-2342-9-4.

Thorsten M. Buzuga,∗, Gael Bringouta, MarlittErbea, KsenijaGräfea, Matthias Graesera, Mandy Grüttnera, AleksiHalkolaa, Timo F. Sattel a, WiebkeTennera, Hanne Wojtczyka, Julian Haegele b, Florian M. Vogtb,JörgBarkhausenb, Kerstin Lüdtke-Buzuga,Magnetic particle imaging: Introduction to imaging and hardware realization. Z. Med. Phys. 22 (2012) 323–334 http://dx.doi.org/10.1016/j.zemedi.2012.07.004, http://journals.elsevier.de/zemedi

S. Biederer, T. Sattel, T. Knopp, K. Lüdtke-Buzug,B.Gleich, J., Weizenecker, J. Borgert, T.M. Buzug, A Spectrometer for Magnetic Particle Imaging. ECIFMBE 2008, IFMBE Proceedings 22, pp. 2313–2316, 2008

S. Biederer, T. Sattel, T. Knopp, K. Lüdtke-Buzug,B.Gleich, J. Weizenecker, J. Borgert, T.M. Buzug, A Spectrometer for Magnetic Particle Imaging. ECIFMBE 2008, IFMBE Proceedings 22, pp. 2313–2316, 2008

Web pages

Magnetic particle spectroscopy. http://www.nanomag-project.eu/magnetic-particle-spectroscopy.html

XR-2206 Monolithic Function Generator. https://www.sparkfun.com/datasheets/Kits/XR2206_104_020808.pdf

TDA2050 32 W hi-fi audio power amplifier. http://www.alldatasheet.com/datasheet-pdf/pdf/25046/STMICROELECTRONICS/TDA2050.html

Active Filters - Characteristics, Topologies and Examples, http://sound.whsites.net/articles/active-filters.htm

Operational transconductance amplifier, https://en.wikipedia.org/wiki/Operational_transconductance_amplifier

SlawomirTumanski, Induction Coil Sensors – a Review. http://www.tumanski.x.pl/coil.pdf

Afyon Kocatepe Üniversitesi Uluslararası Mühendislik Teknolojileri ve Uygulamalı Bilimler Dergisi

Afyon Kocatepe University International Journal of Engineering Technology and Applied Sciences

AKÜ IJETAS Vol 2 (2019) Haziran (10-18 s) AKU J.Eng.App.Sci. **Vol 2** (2019) June(10-18 pp)

Araştırma Makalesi / Research Article

AISI 420 Paslanmaz Çeliklerin M42 Çelik Tel ile Kaynağı Sonrası Soğuma Ortamına Bağlı Mekanik ve Morfolojik Özelliklerindeki Değişimler

Mehmet Çakmakkaya[1], Şükrü Talaş[2], H. Andaç Yasan[2] , M. İskender Eroğlu[2]
1Afyon Kocatepe Universitesi, Teknoloji Fakultesi, Otomotiv Muhendisliği, 03200 Afyonkarahisar,Turkey
2Afyon Kocatepe Universitesi, Teknoloji Fakultesi, Metallurji ve Malzeme Muhendisliği, 03200 Afyonkarahisar,Turkey

cakmakkaya1964@gmail.com,stalas@aku.edu.tr

Geliş Tarihi: 25.01.2019 ; Kabul Tarihi:30.04.2019

Özet

Bu çalışmada, AISI 420 martenzitik paslanmaz çeliklere TIG kaynak yöntemiyle Argon gazı korumalı ortamda, M42 çelik tel kullanılarak, 75 amper 4.5cm/dk kaynak ilerleme hızıyla kaynak dikişleri çekilmiştir. Bu amaç için Ø 50mm çapında ve 2, 3.5, 5 ve 6.5 mm kalınlıklarında disk şeklinde parçalar hazırlanmıştır. 50 mm boyunca kaynak dikişi oluşturulan bu parçaların kaynaktan hemen sonra farklı soğutma sıvılarına daldırılarak oda sıcaklığına kadar soğumaları sağlanmıştır. Deney numunelerinin sertlik ölçümü kaynak dikişinden esas metale doğru gerçekleştirilmiştir. Mikroyapı karakteristikleri ise optik mikroskop, taramalı elektron mikroskobu (SEM) vasıtasıyla incelenmiştir. Sonuç olarak, östenitik yapının yüksek soğuma hızından etkilenerek martenzitik yapıya dönüşmesi gerçekleşmiştir. Bu tür paslanmaz çeliklerin kritik soğuma hızının altında soğutulmaması için uygun tedbirlerin alınması gereklidir.

Anahtar kelimeler
"TIG kaynağı", "Paslanmaz çelikler", "ITAB" ve "Hızlı soğuma".

Changes in Mechanical and Morphological Properties of AISI 420 Stainless Steels Welded with M42 Steel Wire Associated with Weld Cooling Medium

Abstract

In this study, the method AISI 420 TIG welding of martensitic stainless steels in the protected environment of Ar gas and 75 amps and with a weld speed of 4.5cm/min was carried out using M42 steel wire. For this purpose, specimens of Ø 50mm diameter and thickness of 2, 3.5, 5 and 6 mm was sliced. Weld bead was formed along the specimen for about 50mm long and following the welding, specimens were immersed into a different cooling fluids to cool to room temperature. Microhardness measurement was carried out mainly from the base metal towards the weld seam. Microstructural characteristics were investigated by optical microscope, scanning electron microscopy (SEM). As a result, the martensitic transformation of the austenitic structure has been influenced by the high cooling rate. This type of stainless steel must not be cooled below a critical cooling rate and it is necessary to take the appropriate measures.

Keywords
"TIG welding", "Stainless steels", "HAZ"and "Fast cooling".

© Afyon Kocatepe Üniversitesi

1. Giriş

Genellikle paslanmaz çelikler yüksek krom alaşımlı çelikler olup, paslanmaz olarak nitelendirilebilmeleri için bu malzemelerin kimyasal içeriğinde en az %10,5 Cr bulunması gerekmektedir (Paslanmaz Çelikler 2002). Çeliğin içeriğindeki kromun korozyona karşı koruyucu kabiliyeti, krom ile oksijen arasındaki büyük affiniteden ileri gelmektedir (Anık ve Tülbentçi 1996). Günümüz endüstrisinde yaygın olarak kullanılan paslanmaz çelikler, içerdiği katkı elemanlarına göre değişen ve tamamen östenitik ile tamamen ferritik özellikler aralığında sıralanan beş farklı çeşit paslanmaz çelik türü bulunmaktadır (Odabaş 2004).

Martenzitik paslanmaz çelikler ağ. %10.5–18 arası Cr içeren ancak asıl martenzitik yapıyı içerdiği ağ. %

0.10 ile 1.2 arasındaki C ile kazanan paslanmaz çelik grubudur. En yüksek C oranı genellikle, ağ. %18 Cr ile beraber bulunur. Bazı martensitik çelikler ise mekanik özelliklerini iyileştiren katkıları örneğin, Nb, Mo ve W gibi alaşım elementlerinden %3' e kadar içerirler. Sahip olduğu yüksek miktardaki C miktarı, çeliğin normal ısıl işlemle sertleştirilebilmesini sağlar. Martensitik paslanmaz çelikler yüksek sertlik için, en uygun paslanmaz çelik grubu olup bu sebeple, kaynak kabiliyeti zayıftır ve genellikle kaynak işlemi sonrası tavlama gerektirir. Korozyon dayanımı östenitik gruba göre düşüktür. Tavlanmış haliyle işlenebilirliği gayet iyidir. Ancak sertleştikten sonra işlenebilirliği zorlaşır. Martenzitik paslanmaz çeliklerin kritik soğuma hızlarının çok yavaş olması, yavaş soğuma halinde, örneğin sakin havada soğuma, martenzit oluşumuna neden olur. Martenzitikler ferritiklere göre çatlak oluşumuna daha da duyarlıdır. (Campbell, 1992, Oğuz, 1985, Tülbentçi, 1985, Bilmes et al 2001).

Martenzit paslanmaz çeliklerin korozyon direnci % 12 Cr içeriklerinden dolayı daha zayıftır. Bu Cr düzeyinde ilave edilecek maksimum karbon miktarı % 1,5'dir (Abington Publishing 1994). Ancak bu durumda fazla karbon tane sınırlarında çökeltmekte ve tane sınırlarına yakın bölgelerde krom miktarı % 12'nin altına düşmektedir (Aran ve Temel 2004). Paslanmaz çelikler türlerine göre farklı fiziksel özellikler gösterirler. Bunlar elastisite modülü, ısıl genleşme katsayısı, ısıl iletkenlik, özgül sıcaklık, manyetik geçirgenlik özelikleridir (Odabaş 2004, Tusek and Suban 2000).

Endüstriyel uygulamalarda paslanmaz çeliklerin kaynaklı birleştirilmelerinde ergitmeli kaynak yöntemlerinden gaz korumalı olanlar ön plana çıkmaktadır. Östenitik paslanmaz çeliklerin gaz altı kaynaklarında koruyucu gaz olarak argon + helyum + karbondioksit içeren gazlar kullanılmaktadır. Argon + oksijen karışımı gazlar kaynak banyosunda oksidasyona neden olmasına rağmen, daha iyi ısıtma kabiliyeti ve ark dengesi sağladığı rapor edilmektedir [Liao, and Chen 1998). MIG kaynağında oksijen karbondioksite göre daha etkili olup argon + % 1-2 oksijen kullanıldığında sprey ark geçişi sağlamaktadır (Tülbetçi 1990, Kaluç ve Sarı 1996). Paslanmaz çelikleri birleştirirken en çok koruyucu gaz olarak saf argon kullanılmaktadır. Argona hidrojen ilavesi ile kaynak hızı ve nüfuziyeti artmakta ve kaliteli kaynak dikişleri elde edilmektedir (Ceyhun 1992). Helyum + argon ile argon + hidrojen karışım gazları yüksek kaynak hızları gerektiği hallerde kullanılmaktadır [Ural ve Kaluç 1996, Tusek and Suban 2000). Azot gazı östenit dengeleyici olduğundan kaynaklı birleştirmelerde kaynak metalindeki δ-ferrit oranı kontrol edilmektedir (Lothongkum al. 2001, Lin and Chen 2001).

Östenitik ve ferritik paslanmaz çelik kalitelerinin kaynaklanmasına en temel fark, potansiyel olarak ferritik çeliklerin sert ITAB'ı veren martenzitik yapısı ile beraber çatlama riski taşıması ve östenitik çeliklerin daha kolay kaynaklanmasıdır. Martenzitik paslanmaz çelikler, özellikle kalın kesit bileşenlerinde ve çok kısıtlamalı bağlantılarda, ITAB'ın çatlamasını önlemek için önlemler alınmasını sağlanarak başarıyla kaynaklanabilir. ITAB'daki yüksek sertlik bu tip paslanmaz çeliğin hidrojen kırılmasına çok eğilimli olmasını sağlar. Çatlama riski genellikle karbon içeriği ile artar (Kumar et al 2012, Sun and Han 1994, Kotecki and Lippold, 2005, Srinivasan et al 2004). Riski en aza indirmek için düşük hidrojen işlemi (TIG veya MIG) kullanarak veya sarf malzemelerinin üreticinin talimatlarına göre kurutulmasını (Örtülü elektrod kaynak elektrodları ve Tozaltı kaynağında kullanılan tozlar) sağlayarak kaynak yapılabilir. Yaklaşık 200 ila 300 °C'ye ön ısıtma işlemi özellikle Cr ve C içeriği, kesit kalınlığına ve kaynak metaline giren hidrojen miktarına bağlı olacaktır. Zaman ve sıcaklık, kimyasal bileşim ile belirlenecektir (Sun and Han, 1994, Kumar et al 2012, Lippold, 1981).

İnce kesit, düşük karbonlu malzeme, tipik olarak 3 mm'den az olan, çoğu zaman ön ısıtma yapılmadan kaynaklanabilir. Bu durum düşük difuzedebilen hidrojen girdisinin sağlanabilmesi için birleştirme alanının temizlenmesine dikkat edilmesiyle başarılabilinir. Daha kalın kısım ve daha yüksek karbonlu (>% 0.1) malzeme muhtemelen ön ısıtma ve kaynak sonrası ısıl işlem gerektirecektir. Kaynak

sonrası ısıl işlem kaynaktan hemen sonra sadece yapıyı temperlemek için değil, aynı zamanda hidrojenin kaynak metalinden ve ITAB'dan uzaklaşmasını sağlamak için yapılmalıdır (Lippold 1981, Kumar et al 2012, Bilmes 2001).

Martenzitik paslanmaz çeliklerin TIG kaynaklı birleştirmelerin yapısı ve özelliklerine kaynak sonrası soğuma hızının etkisiyle ilgili etraflıca bir çalışma bulunmadığından dolayı bu çalışmada AISI420 martenzitik paslanmaz çeliğin M42 ilave kaynak teli kullanılarak TIG kaynaklı birleştirmesinin özelliklerine ve mikroyapısına kaynak sonrası soğuma hızının etkisi araştırılmıştır.

2. Materyal ve Metot

Çalışmada kullanılacak paslanmaz çelik, şerit testere yardımı ile ø 50mm çapında AISI420 martenzitik paslanmaz çelik çubuktan kalınlığı 2, 3.5, 5 ve 6.5 mm olacak şekilde kesilmiştir. Disk şeklinde deney numunesi ile beraber her bir kalınlık için 16 adet deney numunesi hazırlanmıştır. Dilimlenen numunelerin üzerine 75 Amper akımda ve 8 lt/dak debide Argon gazı altında TIG yöntemi ile 50mm uzunluğunda, M42 kalite çelikten 2mm kalınlığında ilave çubuk kullanılarak kaynak dikişi çekilmiştir (Şekil 1).

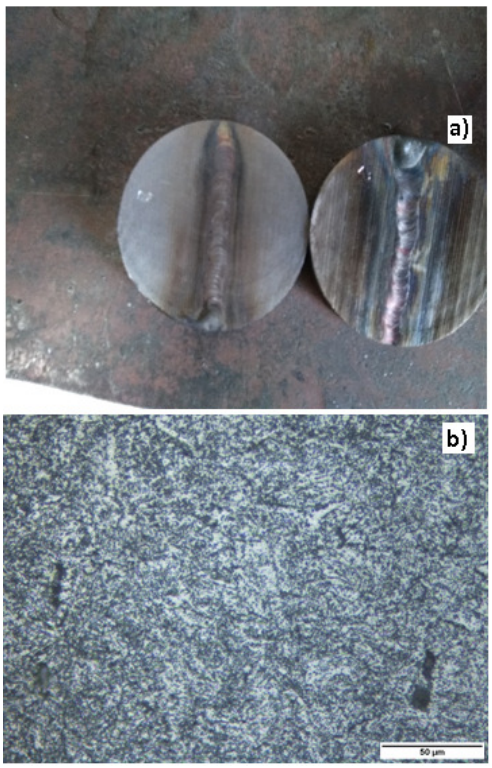

Şekil. 1. a) TIG kaynaklı numune b) esas metal mikroyapı

Tablo 1. AISI 420 ve M42 çeliklerinin nominal bileşimi (M42 de ağ.% 0.9 Mn bulunur)

Kalite	C	Mn	P	S	Si	Cr
420 (1.4021)	0.20	1.0 max	0.04 max	0.03 max	1.0 max	13.0
	C	Co	Mo	Cr	V	W
M42	1.08	8	9.4	3.9	1.2	1.5

Kaynak işleminden sonra zaman kaybetmeden farklı kalınlıktaki (2, 3.5, 5 ve 6.5 mm) numuneler farklı soğutma hızı oluşturabilmek amacıyla, bir grup numune oda sıcaklığında (20^{o}C), diğer bir grup 10°C'deki suda ve bir diğer grup numune ise oda sıcaklığındaki yağda soğutulmuştur. Farklı kalınlıktaki diğer bir grup malzeme ise kaynak sonrası havada soğutulmuştur. Eğe ile tufal temizliği yapıldıktan sonra diskotom kesme cihazı ile kaynaklı disk şeklindeki deney numuneleri ortadan ikiye ayrılmıştır. Kesme işlemi tamamlanan numuneler 90-1200G zımparadan geçirilerek, 1 mikron alumina yardımıyla çuhada parlatılıp alkolle temizlenerek metalografik olarak hazırlanmıştır. Metalografik olarak hazırlanan numunenin kaynak

bölgesi daha az miktarda Cr ve Ni içerdiği için yaklaşık 20s Nital ile dağlandıktan sonra incelemeye hazır hale getirilirken, diğer bölgelerinin paslanmaz çelik olması nedeniyle mikroyapısını yapısını daha belirgin hale getirmek için Kalling 2 solüsyonuna 2s daldırılarak dağlama işlemi gerçekleştirilmiştir. Dağlama işleminden sonra numuneler optik mikroskop ile 500x büyütme işlemi uygulanarak incelenmiştir. Elde edilen fotoğraflar daha sonra photoshop programları yardımıyla düzenlenmiştir. Şekil 1b'de çalışmada kullanılan AISI 420 ana malzemenin yapısı gösterilmiştir.

Nikon marka Optik Mikroskop kullanılarak incelemesi biten numuneler Shimadzu HMV-2 Vickers mikrosertlik cihazı ile 4 adet esas metalden, 2 şer adet ITAB bölgesinden, 1 adet ergime bandından ve 3 adet kaynak metali ortasından olmak üzere 10 adet sertlik ölçümü 100gr yük altında gerçekleştirilmiştir. Her bir ölçümün ortalaması alınarak sertlik hakkına genel eğilimin yansıtılması sağlanmıştır. Çalışmada kullanılan her kalınlık ve soğuma durumu için sertlik ölçümü tüm numunelere tekrarlanmıştır. Test sonuçları kaynak bölgesinden olan mesafe – ölçülen sertlik değeri olarak düzenlenip ana malzeme ve kaynak bölgesinin sertlik değişimleri rapor edilmiştir.

3. Sonuçlar ve İrdelenmesi

3.1 Mikroyapı İncelenmesi.

45 numuneden ana malzeme, ITAB ve kaynak bölgesi olmak üzere yaklaşık 200 adet mikroyapı görüntüsü alınmıştır. Çalışmada 4 farklı soğutma durumu için toplam 4 grup, her grup için 4 farklı deney numunesi kalınlığı vardır. Bu çalışmada 16 adet mikroyapı görüntüsü verilmiştir. Bütün mikroyapılar 500x büyütme altında alınmıştır.

Şekil 2' de yer alan mikroyapılar oda sıcaklığındaki suda soğutulan farklı kalınlıklardaki kaynaklı numunelere aittir. Ana metalde görülen yapı östenit ve martenzit fazlarından oluşmaktadır (Kerr and Leone 1982).

Kaynaklı birleştirmelerin kaynak metali görüntülerinden yapıların soğuma ortamı ve parça kalınlığı ile ilişkili soğuma rejimine bağlı olarak farklı morfolojilerde martenzit fazındaki yapılardan oluştuğu göze çarpmaktadır. Şekil 2 a, lath tipi martenzitik yapıyı gösterirken, Şekil 2 b ve c de ise yoğun bir lentiküler yapı bulunmaktadır. Şekil 2d ise, martenzitik ve beynitik yapılar birbiri içine girmiş şekilde görülmektedir. Ferritik matrisin yokluğu ve aynı zamanda Widmanstatten yapıların bulunmaması, yüksek C miktarı ve soğuma hızının değişkenliğinden dolayıdır. (Lin and Chen 2001, Clark and Guha 1982).

Şekil 3'de yer alan mikroyapı görüntüleri oda sıcaklığında bulunan yağda soğutulan farklı kalınlıktaki kaynaklı numunelere aittir. Şekil 4'de yer alan mikroyapı görüntüleri ise soğuma sıcaklığı 10^{o}C olan suda soğutulan farklı kalınlıktaki numunelere aittir. Son grup mikroyapılar kaynak sonrası havada soğutulan farklı kalınlıktaki numunelere aittir (Şekil 5). İlk 3 grupta gözlemlenen iğnesel martenzitler burada hacimsel olarak daha az dağılım göstermektedir. Şekil 5'deki mikroyapı görüntülerinden anlaşıldığı gibi burada gözlemlenen iğnesel yapılar daha yüksek soğuma rejiminde soğutulan numunelerin yapılarına göre daha kısa ve ince yapılı bir oluşumdadır. Oluşan martenzit yapılar iğnesel morfolojili değildir (Lothongkum al. 2001, Gökmen 2006). Şekil 2, 3 ve 4'de verilen resimlerde, ince kesite çekilmiş numunedeki kaynak bölgesinin martezit ile başlladığı ve kalın kesite doğru martenzit + beynit veya 10 °C lik sogutma suyunda soğutulan numunelerde olduğu gibi ince martenzitten kaba martenzite geçiş olduğu görülmektedir. Buna karşın, yukarıda da ifade edildiği gibi, havada sogutulan numunede ise geçiş daha belirgin bir hal almıştır. Kalın kesitlerdeki mikroyapıların soğuma hıızının düşmesi ile beraber beynitik+ferritik yapıya dönüştüğü görülmektedir. Unutulmamalıdır ki, M42 çeliği ferritik olup martensitik çeliğin mikroyapısını değiştirmesi beklenmelidir. Özellikle Şekil 5b ve c'nin dönüşmüş ferritik (martenzit-ferrit) ve kısmen beynitik yapıda olduğu görülmektedir.

Kaynak ergime bölgesi her numune için değişmektedir. Özellikle kalınlık arttığı takdirde kaynak hızı sabit olduğundan penatrasyon derinliği hızla düşmüştür. Sadece 2mm kalınlıkta tam

penetrasyon gözlemlenmiştir. Ayrıca 2 mm malzemeler aynı grup içerisinde daha kalın parçaları göre daha sert bulunmuştur.

Daha öncede belirtildiği üzere esas metal yapıda görülen mikroyapı (şekil 1) martenzitiktir. Kaynak mikroyapısı ise kalıntı östenit ve martenzitten oluşmaktadır. Esas metalde martenzit olmasına rağmen mekanik özellikleri son derece düşüktür. Bunun nedeni AISI 420 çeliğinin ısıl işlemsiz kullanıma uygun olmamasıdır.

ITAB genişlikleri (Şekil 6) sertlikte olduğu gibi en geniş olarak et kalınlığı 2 mm olan malzemelerde gözlenmiştir. Kalınlık azaldıkça ITAB genişliği son derece artmıştır. Bu etki, ısı dağılımının iki boyutlu olmasından kaynaklanmakta olup, ince kesitli parçalarda, normal koşullarda soğutma yapılmasaydı soğuma hızını düşürücü bir etki yaratması beklenirdi. Ancak, bu çalışmada, kaynak metali ve numune kaynaktan sonra soğumaya müsade edilmediği için, kalınlığın sogumaya etkisi su verme ortamına bağlı olarak, havada soğumaya göre daha hızlı olmaktadır. Dolayısıyla mikroyapı daha ince olmakta ancak ITAB genişliği değişmemektedir. Çünkü, ITAB oluşumu soğutmadan önce tamamlandığı için sogutmanın bir etkisi değil kalınlığın bir sonucu olarak ITAB genişlikleri fazla çıkmaktadır.

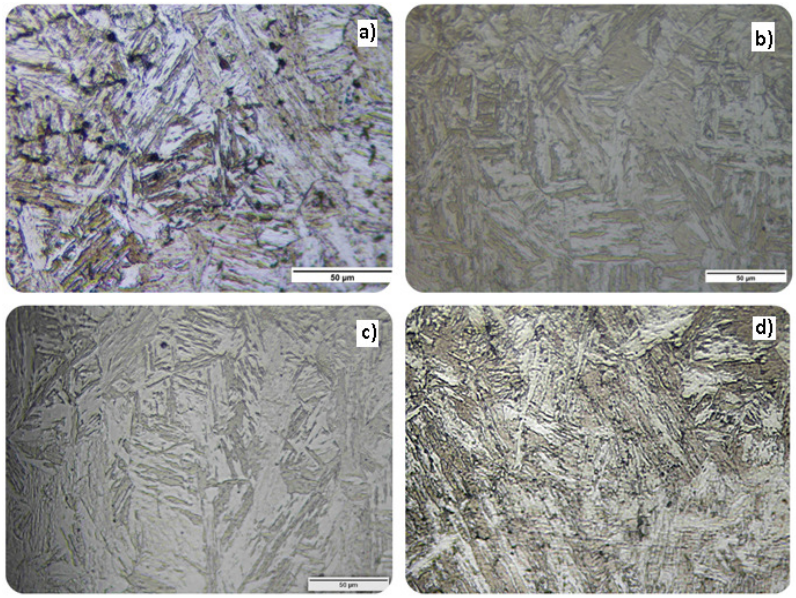

Şekil 2. Farklı kalınlıkta 20°C sıcaklıkta suda soğutulan kaynaklı numunenin mikro yapı görüntüleri (500x), a) 2 b) 3,5 c) 5 d) 6,5 (mm)

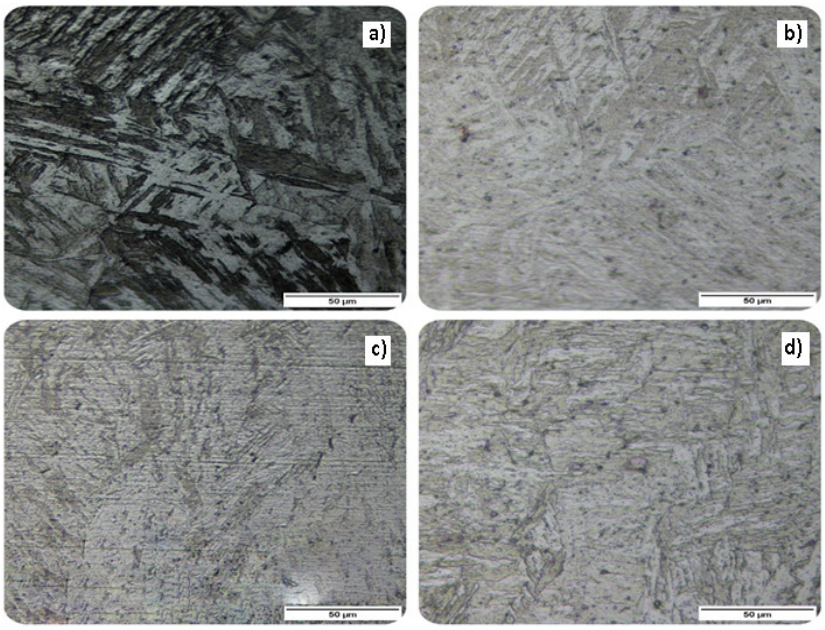

Şekil 3. Farklı kalınlıkta yağda soğutulan kaynaklı numunenin mikroyapı görüntüsü (500x), a) 2 b) 3,5 c) 5 d) 6,5 (mm)

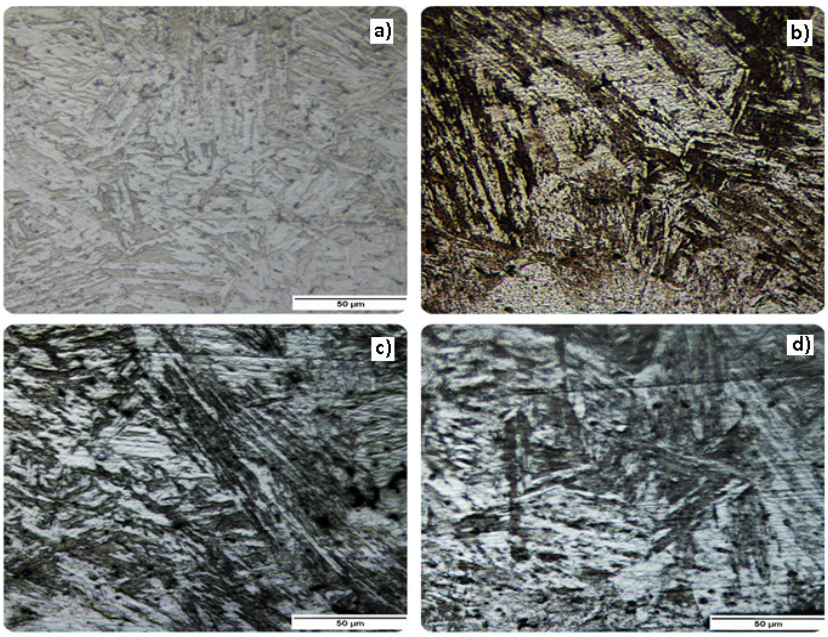

Şekil 4. Farklı kalınlıkta 10°C sıcaklığında suda soğutulan kaynaklı numunenin mikroyapı görüntüsü (500x), a) 2 b) 3,5 c) 5 d) 6,5 (mm)

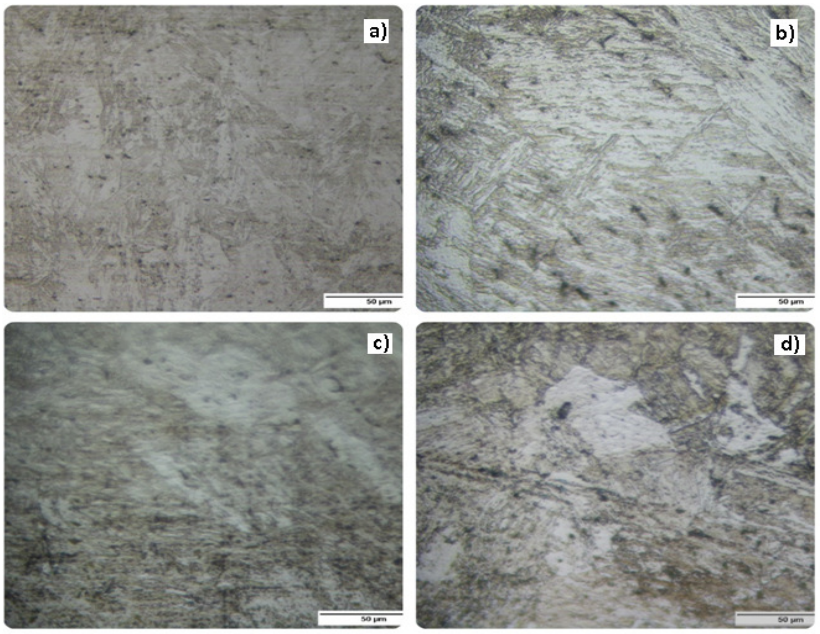

Şekil 5. Farklı kalınlıkta havada soğutulan kaynaklı numunenin mikroyapı görüntüsü (500x), a) 2 b) 3,5 c) 5 d) 6,5 (mm)

3.2. ITAB Genişliğinin Kaynak Sonrası Soğuma Hızıyla İlişkisi

Kaynaklı birleştirmelerin mikroyapı incelemelerine ilaveten numunelerin daha sonra ITAB görüntüleri üzerinden ölçümler alınmış ve ITAB genişlik grafiği oluşturulmuştur. Sonuçlar grafiksel olarak Şekil 6'da grafiksel gösterilmiştir.

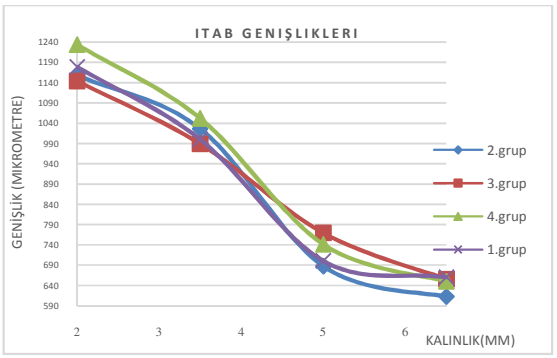

Şekil. 6. ITAB genişliğinin kalınlığa göre değişimi

En yüksek ITAB genişliği; 2mm kalınlıkta ve havada soğuyan deney numunesinde tespit edilmiştir (Şekil 6). 20°C ve 10°C' de suda ve 25°C de yağda soğuyan 2mm kalınlığa sahip numuneler ITAB genişlik değerleri son derece birbirine yakın bulunmuştur. İş parçası kalınlığı arttıkça ITAB genişliği düşmektedir. Düşük kalınlıkta yavaş soğuma hızında görülen en yüksek ITAB genişliği, daha kalın iş parçasında artan kalınlıkla soğuma hızı artışına bağlı ITAB genişliği daralmaktadır. Bunun nedeni yüksek et kalınlığı nedeniyle soğumanın nispeten daha hızlı gerçekleşmesidir.

3.3. Kaynaklı Birleştirmelerin Kaynak Sonrası Soğuma Hızı ile Sertlikleri Arasındaki İlişki

Farklı kesit kalınlığındaki deney malzemelerine TIG kaynak işlemi sonrası uygulanan farklı soğutma rejiminin birleştirmenin sertliği üzerindeki etkisi de çalışmada incelenmiştir.

Şekil 7, kaynak metalinin ortalama sertliğini göstermektedir. Kaynak bölgesinde 2mm kesit kalınlığına sahip numunede en yüksek sertliğe 632HV0.1 ile ulaşmıştır. En düşük sertlik ise 527 HV0.1 ile 6.5mm kesit kalınlığına sahip numunenin kaynak metalinde ulaşılmıştır. Şekil 7'de görüldüğü üzere 20°C suda soğuyan et kalınlığı en düşük (2mm) olan deney numunesinde kaynak metalinde en yüksek sertlik değerine ulaşmıştır. Kesit kalınlığı azaldıkca kaynak sonrası soğumanın en hızlı olduğu bir durum sözkonuzu olup, artan et kalınlığı ile beraber soğuma hızı düşmektedir ve kaynak metalinin genel sertlik değerleri azalmıştır.

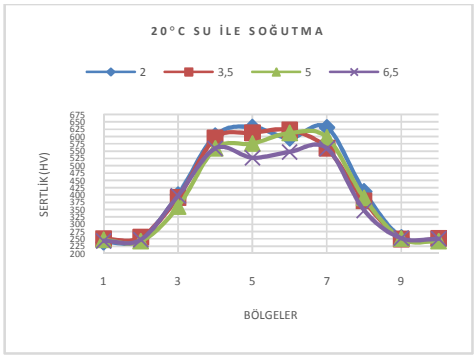

Şekil. 7. 20°C'de soğutulan farklı kalınlıktaki numunelere ait sertlik değerleri.

Şekil 8'de 25°C yağda soğuyan grupta sertlik değerleri 1. gruba göre daha düşük olarak gözlenmiştir. En yüksek sertlik değeri yaklaşık 600$HV_{0.1}$ olarak kaynak metalinde ölçülmüştür. En düşük sertlik ise 567$HV_{0.1}$ ile 6,5 mm lik malzemedir.

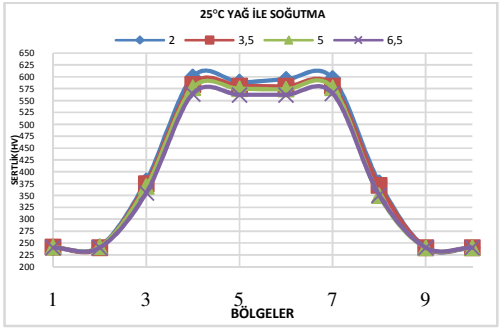

Şekil. 8. 25°C'de yağda soğutulan farklı kalınlıktaki numunelere ait sertlik değerleri.

10°C suda soğuyan numuneye ait sertlik grafiği şekil 9'da verilmiştir. Şekil 9'da verilen sertlik grafiği deneyde en yüksek sertlik değerlerine sahiptir. 2mm kesit kalınlığına sahip numune için sertlik

yaklaşık kaynak bölgesinde 800HV$_{0.1}$ ye kadar ulaşmıştır.

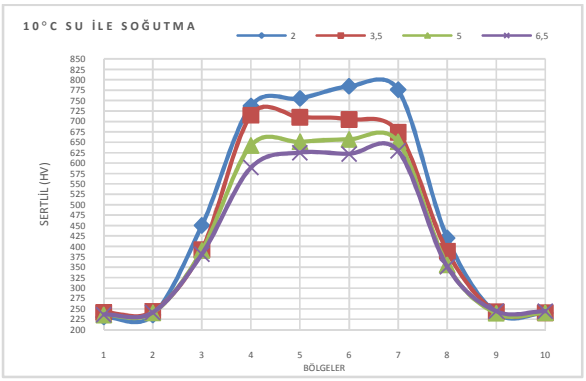

Şekil. 9. 10°C'de su ile soğutulan farklı kalınlıktaki numunelere ait sertlik değerleri.

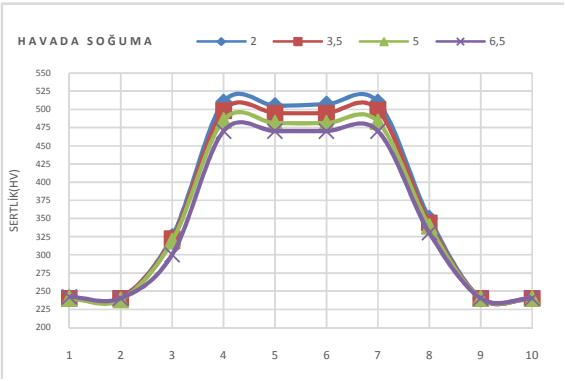

Şekil. 10. Havada soğuyan farklı kalınlıktaki numunelere ait sertlik grafiği.

Şekil 10'da kaynak sonrası havada soğutulan farklı kalınlıktaki numunelere ait sertlik dağılımı grafiksel olarak gösterilmiştir. Şekilden görüldüğü gibi en yüksek sertlik 2 mm kesit kalınlığına sahip numunenin kaynak metalinde yaklaşık 525 HV0.1 ve en düşük sertlik ise kesit kalınlığı 6,5 mm olan numunenin kaynak metalinde yaklaşık 475 HV0.1 bulunmuştur.

Sertlik sonuçları kaynak metali sertliğinin artan et kesit kalınlığına bağlı olarak genel olarak azaldığına işaret ederken, kaynak sonrası soğuma rejimini arttıran soğuma ortamlarına göre de kaynaklı bağlantının sertliğinin arttığına işaret etmektedir.

Şekil 11'de görüldüğü gibi çelik numunede havada soğuma şartlarında bile martenzit yapı elde edilebilmektedir. Havada soğuyan numunelerde yaklaşık 480HV$_{0.1}$ elde edilmiştir. Bu tip çeliklerde Martenzit dışı yapıların eldesi ancak tam tavlama tipi atmosferlerde mümkündür. Normalize, suda, yağda soğutulan çeliklerde martenzitik dönüşümün elde edilmesi kaçınılmazdır, ancak mikroyapıda dönüşmeden kalan kalıntı östenitlerde bulunabilmektedir.

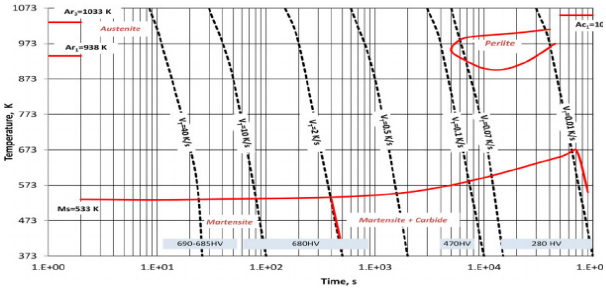

Şekil. 11. AISI 420 martenzitik paslanmaz çeliğe ait TTT diagramı ve CCT eğrileri [16].

4. Genel Sonuçlar

Farklı kesit kalınlığında TIG kaynak yöntemiyle birleştirilen ve kaynak sonrası farklı soğuma ortamlarında soğutulan numunelerin kaynak metali yapısı, ITAB genişliği ve kaynaklı bağlantının sertliği incelenmiştir. Genel olarak değerlendirildiğinde soğuma ortamı ve iş parçası et kesit kalınlığına bağlı olarak artan soğuma rejimiyle ilişkili olarak kaynak metalinin yapısının martenzit fazının yanı sıra kalıntı östenitten oluştuğu görülmektedir. Martenzitin morfolojisi yüksek soğuma hızına sahip numunelerde iğnesel martenzit formunda oluşmaktadır. Kaynak metalinin ITAB genişliği et kesit kalınlığı düşük ve kaynak sonrası soğuma rejiminin endüşük olduğu soğutma ortamında en geniş olarak bulunmuştur. Kaynak metalinin sertliği ise en yüksek en hızlı sğuma rejimine sahip deney numunesinde elde edilmiştir. Sonuç olarak martenzitik paslanmaz çeliklerin kritik soğuma hızının altında soğutulmaması için uygun tedbirlerin alınması gerekli olduğu görülmektedir. Bu bağlamda kaynak öncesi bir ön tav ısıl işleminin yanı sıra kaynak sonrası gerginlikleri giderme ısıl işlemi uygulanması önerilebilir.

KAYNAKLAR

Paslanmaz Çelikler 2002 Teknik Metal Endüstri Malzemeleri Tic. ve San. A.S., Adana,

Ceyhun, V., 1992 Ferritik-Ostenitik Paslanmaz Çeliklerin Karbonlu Çelik ile Nokta Kaynagında Kaynak Parametrelerinin Baglantının Çekme Makaslama Dayanımına ve Taneler Arası Korozyonuna Etkisi, Doktora Tezi, İTÜ., Fen Bilimleri Enstütüsü, istanbul, s. 1-29

Anık S., Tülbentçi K., 1990 Çelikler için Kaynak Metalurjisi", İskender Matbaası, İstanbul.

Abington Publishing, 1994 Welding Metalurgy of Stainless Steels, Abington Welding Training Module, *Cambridge*, pp. 1-45.

Odabas C., 2004 Paslanmaz Çelikler, Temel Özellikleri, Kullanım Alanları, Kaynak Yöntemleri, Askaynak-istanbul, 2. Baskı, Tavaslı Matbaası.

Aran, A., Temel, M.A., 2004 Paslanmaz Çelik, Acar Matbaacılık A.S., İstanbul.

Lıao, M.T.; Chen, P.Y., 1998 The Effect of Shielding-Gas Compositions on The Microstructure and Mechanical Properties of Stainless Steel Weldments", *Materials Chemistry and Physics, 55, 145-151.*

Tülbetçi, K., 1990 Paslanmaz Çeliklerin Kaynagı, MIG-MAG Eriyen Elektrot ile Gazaltı Kaynagı, 137–142, Gedik Holding-istanbul.

Kaluç, E., Sarı, N., 1996 Paslanmaz Çeliklerin MIG Yöntemi ile Kaynagı, *Metal ve Kaynak*, 32-75.

Ural, M., Kaluç, E., 1996 Paslanmaz Çeliklerin TIG Yöntemi ile Kaynagı, *Metal Makine*, 12-20, Mart.

Tusek, J., Suban, M., 2000 Experimental Research of the Effect of Hydrogen in Argon as a Shielding gas in Arc Welding of Highalloy stainless steel, *Int J. Hydrogen Energy*, 25, 4, 369–376.

Lothongkum, G., Vıyanıt, E., Bhandhubanyong, P., 2001 Study on The Effects Pulsed TIG Welding Parameters on Delta-Ferrite Content, Shape Factor and Bead Quality in Orbital Welding of AISI 316L Stainless Steel Plate, *Journal of Mater. Proc. Tech*., 110, 233- 238.

Lın, Y.C., Chen, P.Y., 2001 Effect of Nitrogen Content and Retained Ferrite on Residual Stress in Austenitic Stainless Steel Weldments, *Materials Science and Engineering A*, 307, pp. 165-171.

Clark, C.A.; Guha. P., 1982 Welding Characteristic of Duplex Satainless Steels, Duplex Satainless Steels, *Conference Proceeedings American Society For Metals*, Ohio, pp. 632.

Kerr, H. W., Leone, G. J., 1982 Ferrite to Austenite Transformation in Stainless Steels, *Welding Journal*, 61 (1), 13-17.

Gökmen, M., 2006 Paslanamaz Çeliklerin Gazaltı Kaynak Yöntemleri ile Kaynagına Koruyucu Gaz ve ilave Metalin Mekanik Özelliklere Etkisi, Sakarya Üniversitesi Fen Bilimleri Enstitüsü, Yüksek Lisans Tezi.

Kotecki, D.J. and Lippold, J.C., 2005 Welding metallurgy and weldability of stainless steels, John Wiley, Hoboken, New Jersey

Srinivasan, P.B., Sharkawy, S.W. and Dietzel, W., 2004 Hydrogen assisted stress-cracking behaviour of electron beam welded supermartensitic stainless steel weldments, *Materials Science and Engineering* A, 385, 6-12

Sun, Z., Han, Y.H., 1994 Weldability and properties of martensitic/austenitic stainless steel joints, *Materials Science and Technology*, 10/9, 823-829

Kumar, S., Chaudhari, G. P., Nath, S. K. and Basu,B., Effect of Preheat Temperature on Weldability of Martensitic Stainless Steel, Materials and Manufacturing Processes, 2012, 27:12, 1382-1386

Bilmes, P.D., Solari, M., Llorente, C.L., Characteristics and effects of austenite resulting from tempering of 13Cr–NiMo martensitic steel weld metals. Mater. Charact. 2001, 46, 285–296.

Lippold, J.C. 1981 Transformation and tempering behavior of 12Cr-1Mo-0.3 V martensitic stainless steel weldments, *Journal of Nuclear Materials*, 104, 1127–1131.

Afyon Kocatepe Üniversitesi Uluslararası Mühendislik Teknolojileri ve Uygulamalı Bilimler Dergisi

Afyon Kocatepe University International Journal of Engineering Technology and Applied Sciences

AKÜ IJETASVol**2**(2019) Haziran (20-28 s) AKU J.Eng.App.Sci. **Vol 2** (2019) June (20-28 pp)

AraştırmaMakalesi / Research Article

WC/Co-Ti Kompozitlerinin Isıl ve Elastik Özelliklerinin Ultrasonik Dalga Hızı ile İlişkisi

Vildan ÖZKAN BİLİCİ[1], İsmail H. SARPÜN[2], M. Selami KILIÇKAYA[3]

[1]*Department of Physics, AfyonKocatepe University, Faculty of Science and Literature, Afyonkarahisar, Turkey*

[2]*Department of Physics, Akdeniz University, Faculty of Science, Antalya, Turkey*

[3]*Department of Physics, EskişehirOsmangazi University, Faculty of Science and Literature, Eskişehir, Turkey*

[*]Corresponding author: *vildanozkan@aku.edu.tr*

GelişTarihi:21.03.2019; Kabul Tarihi:11.05.2019

Anahtar kelimeler

Kompozit; Young's Modülü; Darbe-Yankı; Daldırma; Isıl İletkenlik

Özet

Bu çalışmada, çeşitli kompozitler üretmek ve fiziksel özelliklerini ortaya koymak amaçlanmıştır. Toz metallurjisi ile WC-Co-Ti seramik-metal kompozitinin hazırlanmasında tungsten karbür (WC) tozu ve bağlayıcı faz olarak da kobalt (Co) ve titanyum (Ti) tozu kullanılmıştır. WC-Co-Ti kompozitlerinde mekanik dalga hızını ölçmek için iki farklı ultrasonik tahribatsız teknik kullanıldı. Çalışmada %60 ile %80 oranında farklı WC_xiçeriği ve 3:1, 1:1 ve 1:3 gruplarında Co/Ti içeriği ile çeşitli numuneler yapıldı.İncelenen malzemelerde WC_x içeriği standart tahribat analizi kullanılarak belirlenmiştir. Üretilen kompozitlerinYoungmodülü (E) ve ultrasonik hızları, ultrasonik darbe-yankı metodu ve daldırma metodu ile ölçüldü. Numunelerin termal iletkenliği, sıcak disk yöntemi ile ölçülmüştür.İki farklı yöntemle elde edilen ultrasonik dalga hızları ile Young's modülü değerleri ve ısıl iletkenlik arasındaki ilişki, fiziksel olarak incelenmiş ve sonuçlar literatür ile karşılaştırılmıştır.

The Relationship of Thermal and Elastic Properties with Ultrasonic Wave Velocity of WC/Co-Ti Composites

Keywords

Composite; Young's Modulus; Pulse-Echo; Immersion; Thermal Conductivity

Abstract

In this study,it is aimed to produce various composites and reveal their physical properties. Tungsten carbide (WC) powder and the two of cobalt (Co) and titanium (Ti) powders as binder phase have been used for the preparation of WC-Co-Ti ceramic-metal composite with powder metallurgy. Two different ultrasonic non-destructive techniques were employed to measure the mechanical wave velocity in WC-Co-Ti composites. The study was performed on various specimens with different WC_x content at the range from 60 to 80% and Co/Ti content in 3:1, 1:1 and 1:3 groups. The WC_x content in examined materials was determined using the standard destructive analysis. The Young modulus (*E*) of the produced composites and the ultrasonic velocity measured through ultrasonic pulse-echo method and immersion method. Thermal conductivity of samples has been measured via hot disk method. The relation between the Young modulus' values with ultrasonic wave velocity, which is obtained through two different methods and thermal conductivity has been physically examined and the results have been compared with the literature.

© AfyonKocatepeÜniversitesi

1. Introduction

A non-destructive testing technique, which is an ultrasonic technique, is used to qualitatively or/and quantitatively evaluate the physical and elastic properties of materials. Cracks, defects, faults and irregularities in the material can be detected by ultrasonic testing (Bouda et al., 2003; Krautkramer, 1977; Markham, 1957). The some material shows a

distinctly anisotropic response which somewhat complicates the experimental tests for the mechanical and physical characterization, especially if conventional testing techniques are used. Many difficulties can be overcome by adopting some non-destructive experimental approaches like, for example, the ultrasonic immersion techniques with pulse-echo. In particular, this ultrasonic experimental approach allows for the determination of all the elastic constants characterizing the mechanical response of a composite material starting from the measurement of the velocity of ultrasonic waves along suitable directions of propagation (Castellano et al., 2014-2016). Cemented carbides consist of the hard carbide phase (WC, TiC, and B_4C) and a transition metal binder (Co, Ni, Ti, Fe). Due to their high hardness (especially in high temperature), strength, excellent wear resistance and low thermal coefficient, cemented carbides are widely used for a variety of machining, cutting, drilling and other applications (Kursawe et al., 2001; Genga et al., 2013; Guo et al., 2008; Xu, 2011). The compatibility between the hard tungsten grains and the ductile cobalt and nickel binder phase enables the composites to have unique and superior combinations of mechanical properties (Hongsheng et al., 2012; Mohammadzadeh et al., 2015). Due to their technological importance these composites of WC have been subject to a great deal of investigation in order to optimize the compositions, the processing leading to the highest mechanical properties and a reduction of the manufacturing cost compared with the production method such as welding, plastic forming, extrusion, injection, casting (Fernandes et al., 2008). The possibility of complete or, at least, partial substitution of cobalt with nickel or other metals, alloys and composite in sintered WC-Co, WC-Ni and WC-Co-Ni cemented carbides has been investigated for years (Voitovich et al., 1996; Zhang et al.,2005; Krishnaveni et al., 2006; Shon et al., 2009). Tungsten cemented carbide was used to designate a metal matrix composite constituted by hard ceramic particles, normally WC, into a metallic matrix. Conventional tungsten carbide hard metal alloys consist of tungsten carbide with a soft and ductile metal Co as the binder phase. Also cobalt wets tungsten carbide well and has good mechanical properties (Fernandes et al., 2011; Konyashin et al., 2014; Gaoa et al., 2018). Recently, tungsten carbide (WC) reinforced metal matrix composites such as WC-Co (Zhong et al., 2011), WC-Ni (Zhang et al., 2015), WC-Fe (Zhong et al., 2016), WC-CoNi (Tarrago et al., 2015), WC-CoCr (Hong et al., 2016), WC-CoCu (Gu et al., 2007) and WC-Al (Lekatou et al., 2015) were obtained by adding components such as Ti, Ni, Cr, Al, Ta and Nb beside the Co matrix to improve the bonding properties (Ekroth et al., 2000). In this study, WC-Co-Ti composite samples obtained in 3:1, 1:1 and 1:3 groups using the powder metallurgy technique. Moreover, the research carried out a series of experimental tests to explore the characteristics and properties of the same sintering temperatures on different specimens with varying amounts of Co and Ti. Evaluation of thermal and elastic properties of composite materials obtained in this study was investigated by using ultrasonic and thermal hot-disk techniques. We have examined the relationship between thermal and elastic properties of WC / Co-Ti composites with ultrasonic wave velocity, as they provide information about the study of ultrasonic wave propagation in metals, alloys and composites on the microstructure, mechanical and physical properties of the material.

2. Materials and Methods

In this study, Tungsten carbide (WC) powders of 10 µm particle size with 99.5 % purity, Cobalt (Co) and Titanium (Ti) powders of -325 mesh particle size with 99.5 % -99 % purity were used in the form of powders and also were both provided from Alfa Aesar Company (Massachusetts, ABD). One of the purposes of this work is to reinforce WC ceramic powders with Co-Ti. Co and Ti powders were added in the mixture directly. In the experimental study, the samples were prepared through three different compositions. Co/Ti ratios were taken in 3:1, 1:1 and 1:3 groups depending on WC_xvolume ratio. All the samples were mixed homogenously for 24 h in a mixer following the weighing. The mixture was shaped by single axis cold hydraulic pressing using high strength steel die of 15 mm diameterand 5

mm height. A pressure of 305,9 kg/cm^{2}was used for compacting all the powder mixtures. The cold pressed samples underwent sintering at 1000 °C for 2 h in a traditional tube furnace using Argon gas atmosphere. The samples were cooled in the furnace after sintering and their longitudinal and transverse ultrasound velocity Young's modulus and thermal conductivity measurements were carried out using ultrasonic non-destructive testing which are pulse-echo and immersion methods for the longitudinal and transverse ultrasound (ultrasonic) velocity measurements and hot disk method for thermal conductivity measurements, respectively. Sintered composite samples were characterized using Leo 1430 VP equipped with Röntec energy dispersive X-ray (EDX) model scanning electron microscopy (SEM). Figure 1 shows the SEM microanalyses images of WC-Co-Ti composites.

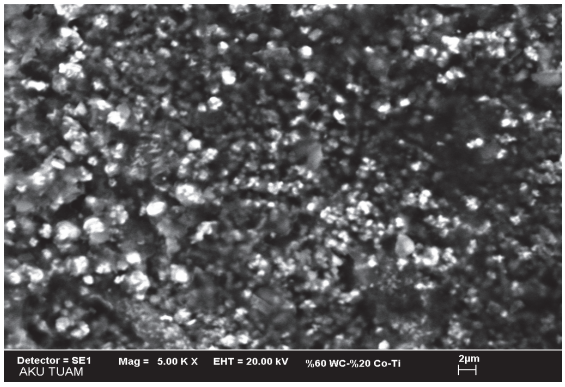

(a)

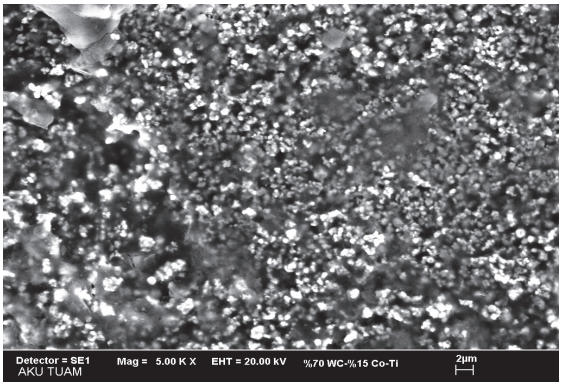

(b)

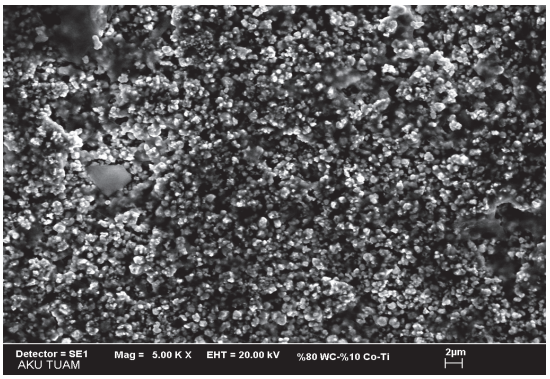

(c)

Figure 1. SEM pictures of a) $WC_{0.6}$+$Co_{0.2}$+$Ti_{0.2}$ b) $WC_{0.7}$+$Co_{0.15}$+$Ti_{0.15}$ c) $WC_{0.8}$+$Co_{0.1}$+$Ti_{0.1}$ samples.

In this study, a system combining immersion and pulse method was developed to measure the pass times of the samples in water and both the longitudinal and transverse ultrasound velocities of the samples. In pulse-echo method, a transducer serves as both a receiver and a transmitter. The ultrasound wave obtained by applying very short electrical signals to the transducer is sent to the material. As the ultrasound wave moves through the material, the same transducer starts to operate as a receiver. When the ultrasound wave reflected from the back wall of the sample reaches the transducer, the mechanical vibrations are converted into electrical signals. Velocity measurements were obtained by reflection peaks from the front and back surface of the ultrasound wave sent to the sample by the transducer. The determination of transmission velocity of ultrasonic waves through the composites were performed by a Panametrics 5800 model Olympus brand computer-controlled pulser-receiver (PR) and digital oscilloscope with Sonatest SLH4-102 T/R transducer probe to measure longitudinal velocities and GE Inspection Technologies MB-4Y T/R transducer probe to measure transverse velocities at the frequency of 4 MHz at the room temperature.Sonatestsonagel-W was used as interface between the transducers and composite samples, given the smoothness of the composite surfaces. In immersion testing, the transducer probe is placed in the water tank, above the test object, and a beam of sound is projected. When an ultrasound wave emitted within the water used in

the experimental setup strikes a solid object so that it normally has a certain angle of incidence, the incoming wave is divided into a transverse and longitudinal wave within the sample. Thus, necessary measurements were made over transverse and longitudinal waveforms. When the sample was placed between each of the Z4K53342-2324 transducer probe at the frequency of 5 MHz were obtained by combining pulse-echo and immersion methods. Density of all the sintered WC-Co-Ti composite samples was measured with Archimedes principle, later Young's modulus have been obtained with using calculated densities, ultrasonic longitudinal and transverse velocity. Young's modulus in medium can be found by the following equation (1):

$$E = \rho V_T^2 \frac{3V_L^2 - 4V_T^2}{V_L^2 - V_T^2} \qquad (1)$$

where V_L is the longitudinal wave velocity (m/s), V_T is the transversewavevelocity (m/s) and ρ is density. The thermal conductivity measurements of the WC-Co-Ti composite samples were obtained using the hot disk method to investigate the relationship between the Young's modulus and thermal conductivity. The well-established Hot Disk Thermal Constants Analyzer method allows rapid, accurate and non-destructive testing of thermal conductivity of most material types, all in a single measurement and also conductivity and diffusivity are tested directly. The sensors used in this test method which is sandwiched between two insulating specimen halves (Figure 2). In this study, using the basic theory of measuring the thermal conductivity of the heated plane sensor, the conductivity values have been read from the system (Ashraf, 2014; Yi, 2005).

transducers, the time taken for the wave passing through the track and the time taken for the wave moving between the transducers in the water between the transducers were taken and the speed in the water was determined. In this study, transverse and longitudinal ultrasonic measurements of GE Inspection Technologies

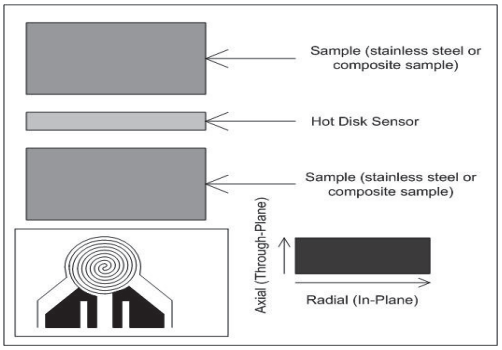

Figure 2.Schematic of samples and sensor for the Hot Disk.

3. Results and Discussion

Young's modulus and thermal conductivity of the prepared ceramic-metal composite material was physically tested. Experimental results obtained with ultrasound velocities, elastic modulus, thermal conductivity and density values belong to the samples prepared by adding Co and Ti binder into WC powder are given in Table 1. The variations in longitudinal and transverse ultrasound velocity with Young's modulus and thermal conductivity of WC-Co-Ti samples are shown in Figs. 3 and 4. When WC-Co-Ti composite samples obtained in 3:1, 1:1 and 1:3 groups is examined, there is a linear increase in the longitudinal and transverse ultrasound velocities.

Table 1.Ultrasound velocities, elastic modulus, thermal conductivity and density values of WC-Co-Ti composite sample.

	Pulse-Echo Method			*Immersion Method*			*Thermal Conductivity*	*Density*
Sample	V_L (m/s)	V_T (m/s)	E (GPa)	V_L (m/s)	V_T (m/s)	E (GPa)	(W/mK)	(g/cm^3)
$WC_{0.6}+Co_{0.3}+Ti_{0.1}$	4942	2249	94.2	4933	2362	102.5	6.82	6.8
$WC_{0.6}+Co_{0.2}+Ti_{0.2}$	5313	2501	110.4	5104	2532	111.4	6.98	6.5
$WC_{0.6}+Co_{0.1}+Ti_{03}$	5871	2721	133.2	5839	2870	145.8	7.59	6.6
$WC_{0.7}+Co_{0.225}Ti_{0.075}$	4633	2467	112.5	4777	2489	115.6	3.48	7.1
$WC_{0.7}+Co_{0.15}Ti_{0.15}$	5138	2636	123.0	4982	2683	125.0	4.40	6.7
$WC_{0.7}+Co_{0.075}Ti_{0.225}$	5653	2824	140.4	5281	3076	155.3	5.29	6.6
$WC_{0.8}+Co_{0.15}+Ti_{0.05}$	4438	2626	113.7	4586	2509	108.5	3.20	6.7
$WC_{0.8}+Co_{0.1}+Ti_{0.1}$	4934	2759	139.5	4747	2870	143.8	3.38	7.2
$WC_{0.8}+Co_{0.05}+Ti_{0.15}$	5380	2941	140.2	4915	3307	149.7	3.68	6.3

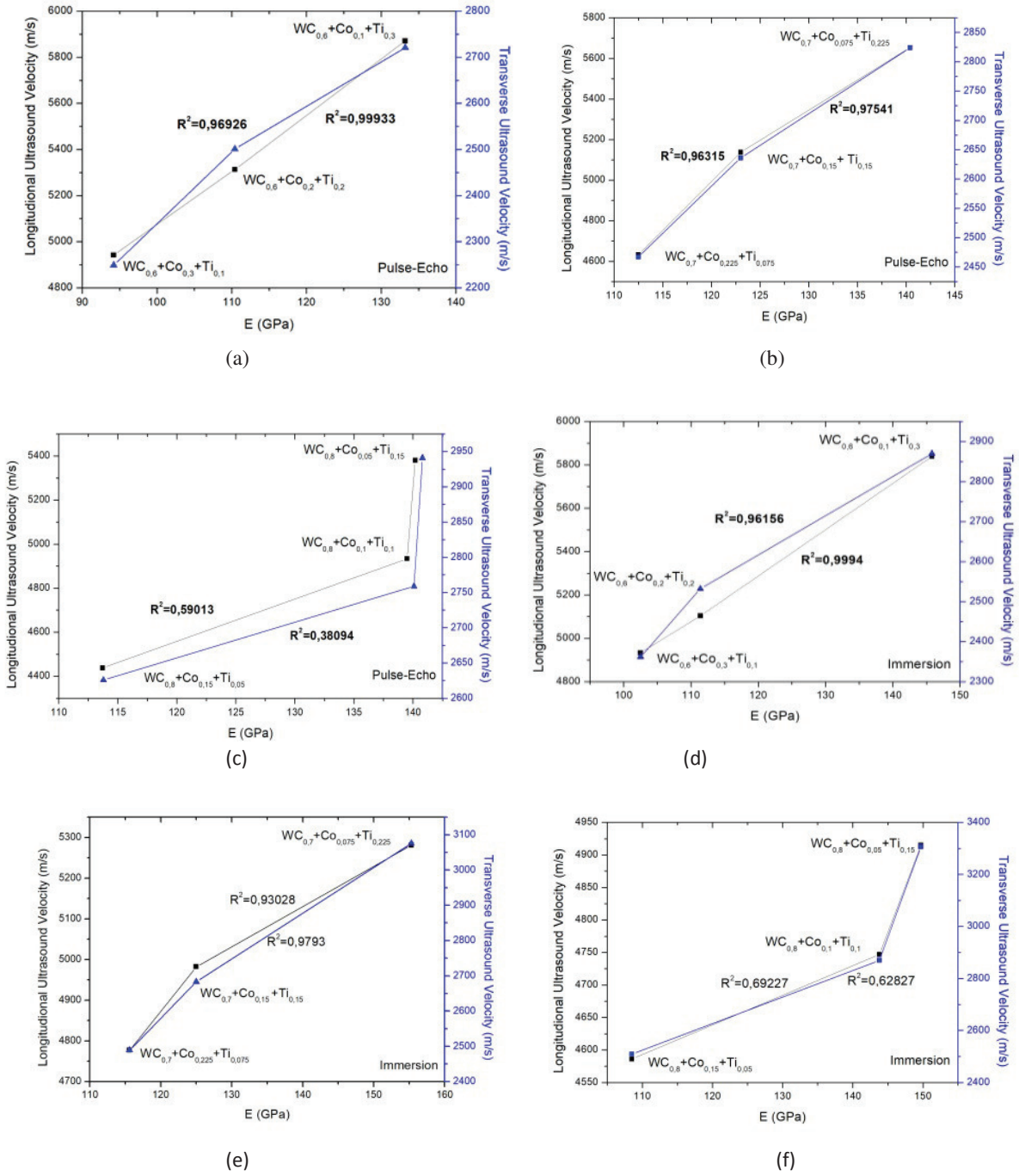

Figure 3.Variation in longitudinal and transverse ultrasound velocity with Young's modulus (a-c) Pulse-echo method and (d-f) Immersion method.

However, the situation is different when examined according to WC rate. A comparison showed that the results obtained for the wave velocity from pulse-echo and immersion method are in good agreement, indicating that both techniques can be considered as a quantitative non-destructives tool of mean grain size content evaluation. The results are presented in the form of linear relationships of wave velocity versus tungsten content in the composite materials. While longitudinal ultrasound wave velocity values of WC-Co-Ti composite sample decrease depending on WC_x volume ratio, there is an increase in transverse ultrasound wave velocity values. By considering size of WC particles in the structure, arrays of atoms in the strands in the longitudinal wave measurement performed parallel to the axis being smaller than the other

binding phases will effect homogeneous distribution, thus longitudinal wave velocity in the matrix element are observed to decrease. In addition, BiliciÖzkanet al. (2018) have investigated the relationship between thermal and elastic properties of WC-Fe-Ti composites in another study.They observed a modest increase in Young's modulus and thermal conductivity, as in WC-Co-Ti composites. Also,In Figures 5.a-c, Young modulus, as calculated depending onultrasound velocities and densities as previously described and thermal conductivity linearly increases. R^2 value of fit line in Figure 5.c is lower than the others. It is caused by Young modulus values of $WC_{0.8}+Co_{0.1}+Ti_{0.1}$ and $WC_{0.8}+Co_{0.05}+Ti_{0.15}$ compositions, being very close to each other for both ultrasound methods.

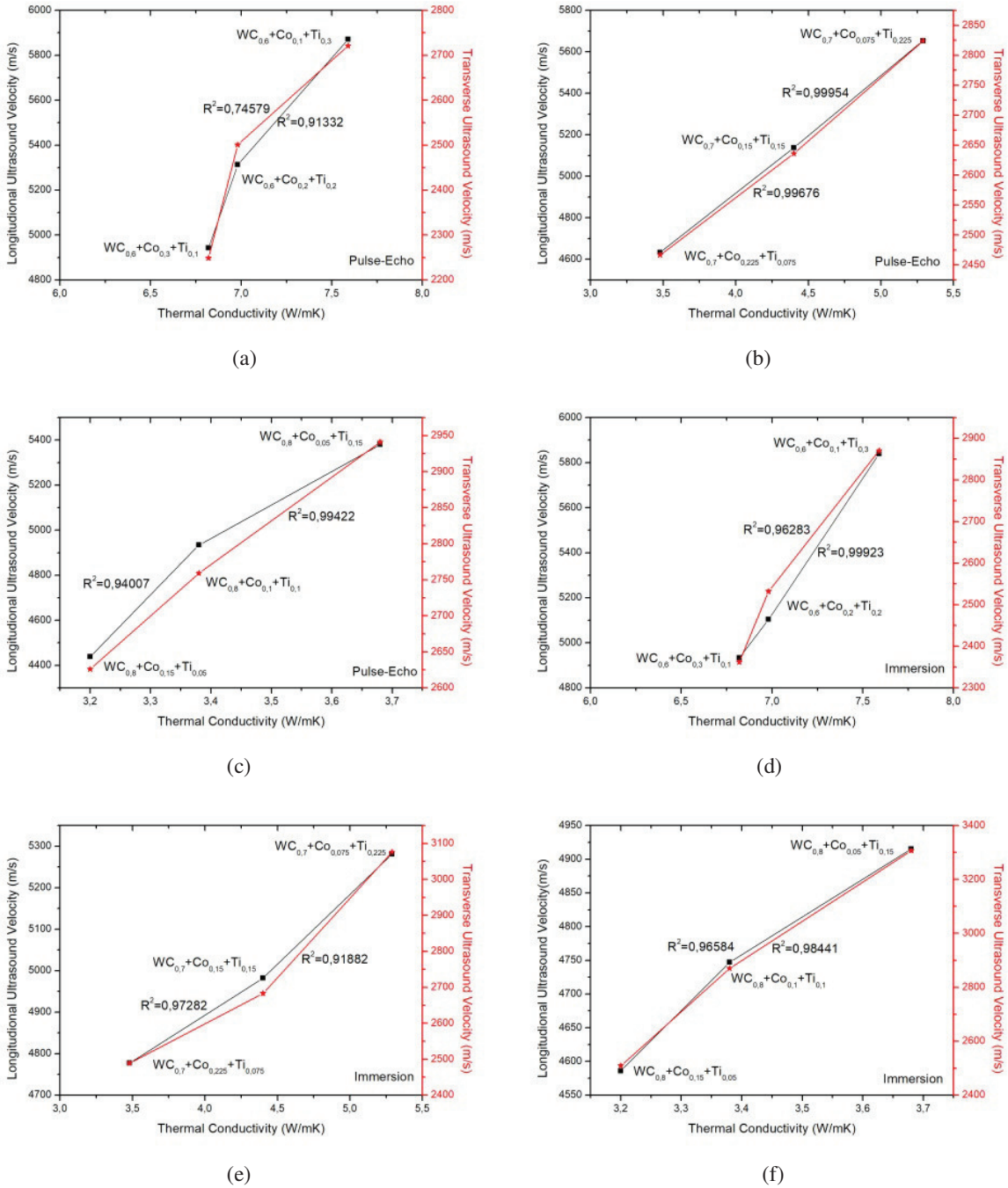

Figure 4.Variation in longitudional and transverse ultrasound velocity with thermal conductivity (a-c) Pulse-echo method and (d-f) Immersion method.

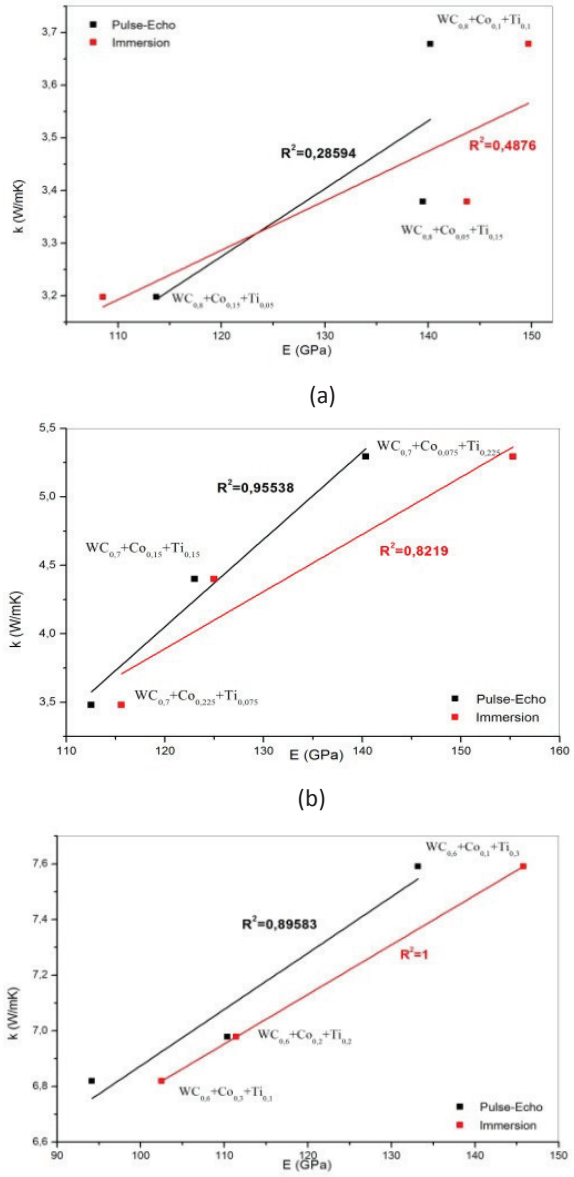

Figure 5.Thermal conductivity and Young modulus graph of (a) $WC_{0.6}$–Co–Ti, (b) $WC_{0.7}$–Co–Ti, (c) $WC_{0.8}$–Co–Ti composite sample.

R^2 value of fit line in Figure 5.c is lower than the others. It is caused by Young modulus values of $WC_{0.8}+Co_{0.1}+Ti_{0.1}$ and $WC_{0.8}+Co_{0.05}+Ti_{0.15}$ compositions, being very close to each other for both ultrasound methods. When SEM images are examined, considering that WC ceramic particles form a strong bond after sintering, grain growth is observed in Figures 5.a and 5.b and is a homogeneous structure. It can be seen that the structure includes two types of pores, small and large. In Figure 5.c, particle boundaries can be seen and the pores are very small and circular in shape.

4. Conclusions

In this study, two different ultrasonic non-destructive techniques were employed to measure the mechanical wave velocity in WC-Co-Ti composites and the relationship between thermal and elastic properties of WC-Co-Ti ceramic-metal composites was investigated. Two different methods (pulse-echo and immersion) have been used for ultrasonic velocity measurements and obtained values are consistent with each other. The main objective of this work was to study efficiency and ability of the pulse-echo ultrasonic in comparison with immersion technique to evaluate some physical properties in WC-Co-Ti composites. The variation of WC and Co/Ti content was clearly identified by the use of both considered techniques. Furthermore, pulse-echo proved to be a suitable method for the investigation of such materials, but it was also less time-consuming than the second considered ultrasonic technique. The described difficulties that can be expected using immersion technique suggest that in the cases where two sides of the composite are accessible, pulse-echo technique is recommended.

A good agreement between the results presented in this study, indicates that both ultrasonic techniques can be considered as a quantitative non-destructive assessment tools. It is therefore concluded that these methods can be used in the evaluation of physical properties in ceramic metal matrix composites, producing interpretable results. As the amount of porosity in the structure increases, the ultrasonic wave velocity propagation decreases (SEM images).

References

Ashraf, A. A., 2014. Measurement of thermal conductivity and diffusivity of different materials by the transient plane source method using hot disk thermal constants analyzer, 1–7.

BiliciÖzkan, V., Sarpün, İ. H. and Kılıçkaya, M. S., 2018, Evaluation of the Elastic and Thermal Properties of WC/Fe-Ti Ceramic-Metal Composites Fabricated by Powder Metallurgy, *International Journal of Scientific & Engineering Research,* 9(8), 10-14.

Bouda, A. B., Halimi, R., Benchaalaa, A. and Lebaili, S., 2003.Ultrasonic NDE of materials grain size and hardness, WCU, Paris.

Castellano, A., Foti, P., Fraddosio, A., Marzano, S. and Piccioni, M.D., 2014.Mechanical Characterization of CFRP Composites by Ultrasonic Immersion Tests: Experimental and Numerical Approaches, *Composites Part B: Engineering*, Vol. 66, 299-310.

Castellano, A., Foti, P., Fraddosio, A., Marzano, S. and Piccioni, M. D., 2016. The ultrasonic C-Scan technique for damage evaluation of GFRP composite materials*, International Journal of Mechanics*, Vol. 10, 206-212.

Ekroth, M., Frykholm, R., Lindholm, M., Andrén, H. O. and Ågren, J., 2000. Gradient zones in WC–Ti(C,N)–Co-based cemented carbides: experimental study and computer simulations, *ActaMaterialia*, 48, 2177–2185.

Fernandes, C. M., Senos, A. M. R., Vieira, M. T., Antunes, J. M., 2008. Mechanical characterization of composites prepared from WC powders coated with Ni rich binders, *International Journal of Refractory Metals and Hard Materials*, 26, 491.

Fernandes, C. M., Senos, A. M. R., 2011. Cemented carbide phase diagrams: A review, *International Journal of Refractory Metals and Hard Materials,* 29, 405 – 418.

Gaoa, Y., Luoa, B. H., Heb, K. J., Zhanga, W. W. and Baia, Z. H., 2018.Effect of Fe/Ni ratio on the microstructure and properties of WC-Fe-Ni-Co cemented carbides, *Ceramics International*, 44, 2030 – 2041.

Genga, R. M., Cornish, L. A. and Akdoğan, G., 2013. Effect of Mo_2C additions on the properties of SPS manufactured WC–TiC–Ni cemented carbides,*International Journal of Refractory Metals and Hard Materials,* 41, 12-21.

Guo, Z., Xiong, J., Yang, M., Song, X. and Jiang, C., 2008.Effect of Mo_2C on the microstructure and properties of WC–TiC–Ni cemented carbide,*International Journal of Refractory Metals and Hard Materials*, 26, 601-605.

Gu, D. D. and Shen, Y. F., 2007. Influence of reinforcement weight fraction on microstructure and properties of submicron WC-Co-p/Cu bulk MMCs prepared by direct laser sintering, *Journal of Alloys and Compounds,* 431, 112 – 120.

Hong, S., Wu, Y. P., Zhang, J. F., Zheng, Y. G., Zheng, Y. and Lin, J. R., 2016, Synergistic effect of ultrasonic cavitation erosion and corrosion of WC-CoCr and FeCrSiBMn coatings prepared by HVOF spraying, *Ultrasonics Sonochemistry*,31, 563 – 569.

Hongsheng, C., Keqin, F., Ji, X., Jianjun, L., Zhixing, G.and Hui, W., 2012.Characterization and forming process of a functionally graded WC–Co/Ni composite, *International Journal of Refractory Metals and Hard Materials,* 35, 306-310.

Konyashin, I., Lachmann, F., Ries, B., Mazilkin, A. A., Straumal, B. B., Kübel, C., Llanes, L. and Baretzky, B., 2014, Strengthening zones in the Co matrix of WC–Co cemented carbides, *ScriptaMaterialia*, 83, 17 – 20.

Krautkramer, J. H., 1977. *Ultrasonic Testing of Materials,* Springer–Verlag, Berlin.

Krishnaveni, K., Sankara, N. and Seshadri, S. K., 2006.Electrodeposited Ni–B coatings: Formation and evaluation of hardness and wear resistance, *Materials Chemistry and Physics,* 99 (2-3), 300-308.

Kursawe, S., Pott, P., Sockel, H. G., Heinrich, W., Wolf, M., 2001.On the influence of binder content and binder composition on the mechanical properties of hardmetals.*International Journal of Refractory Metals and Hard Materials,* 19,335–40.

Lekatou, A., Karantzalis, A. E., Evangelou,A., Gousia, V., Kaptay, G., Gacsi, Z., Baumli, P. and Simon, A., 2015. Aluminium reinforced by WC and TiC nanoparticles (exsitu) and aluminide particles (in-situ): Microstructure, wear and corrosion behavior, *Materials & Design*, 65, 1121 – 1135.

Markham, M. F., 1957. Measurement of elastic constants by the ultrasonic pulse method**,** *British Journal of Applied Physics***,** 6, 56 – 63.

Mohammadzadeh, H., Rezaie, H., Samim, H., Barati, M. and Razavizadeh, H., 2014.Synthesis of WC–Ni composite powders by thermochemical processing method based on co-precipitation, *Materials Chemistry and Physics*, 1-11.

Shon, I-J., Jeong, I-K., Ko, I-Y., Doh, J-M. and Woo, K-D., 2009. Sintering behavior and mechanical properties of WC–10Co, WC–10Ni and WC–10Fe hard materials produced by high-frequency induction heated sintering, *Ceramic International,* 35, 339-344.

Tarrago, J. M., Roa, J. J., Valle, V., Marshall, J. M. and Llanes, L., 2015. Fracture and fatigue behavior of WC-Co and WC-CoNi cemented carbides, *International Journal of Refractory Metals and Hard Materials,* 49, 184 – 191.

Voitovich, V. B., Sverdel, V. V., Voitovich, R. F. and Golovko, E. I., 1996.Oxidation of WC-Co, WC-Ni and WC-Co-Ni hard metals in the temperature range 500–800°C, *International Journal of Refractory Metals and Hard Materials,* 14, 289-295.

Yi, He, 2005.Rapid thermal conductivity measurement with a hot disk sensor Part 1.Theoretical considerations, *ThermochimicaActa,*436, 122 -129.

Zhang, Z. Q., Wang, H. D., Xu, B. S. and Zhang, G. S., 2015.Investigation on influence of WC-Ni addition on rolling contact fatigue behavior of plasma sprayed Ni-based alloy coating, *Tribology International,*90, 509 – 518.

Zhong, Y. and Shaw, L. L., 2011.Growth mechanisms of WC in WC-5.75wt %Co, *Ceramics International,* 37, 3591 – 3597.

Zhong, L. S., Zhang, X., Wang, X., Xu, Y. H., Wu, H. and Fu, Y. H., 2016.Growth kinetics of WC-Fe layer formed at the surface iron during solid-phase diffusion, *Ceramics International,*42, 16941-16947.

Xu, P. Q., 2011. Dissimilar welding of WC–Co cemented carbide to $Ni_{42}Fe_{50.9}C_{0.6}$ $Mn_{3.5}Nb_3$ invar alloy by laser–tungsten inert gas hybrid welding, *Materials and Design*, 32, 229-237.

Afyon Kocatepe Üniversitesi Uluslararası Mühendislik Teknolojileri ve Uygulamalı Bilimler Dergisi

Afyon Kocatepe University International Journal of Engineering Technology and Applied Sciences

AKÜ IJETAS Vol **2** (2019) Haziran (29-34 s) AKU J.Eng.App.Sci. **Vol 2** (2019) June (29-34 pp)

Araştırma Makalesi / Research Article

Tarımsal Atık Takviyeli Kompozitler: Sürdürülebilir Bir Çevre İçin Bir Çözüm

Meena Laad

[1]Department of Applied Sciences, Symbiosis Institute of Technology, Symbiosis International Deemed University, *Pune, Maharashtra, INDIA*

e-mail: meena@sitpune.edu.in

Geliş Tarihi: 14.05.2019; Kabul Tarihi: 31.05.2019

Anahtar kelimeler
Tarımsal atık; Prinç Kabuğu; Metal Matrils Kompozit; Karıştırma döküm tekniği; XRD; SEM

Özet

Tarımsal atıklar veya tarımsal atıklar, çiğ tarım ürünleri yetiştirildiğinde ve işlendiğinde elde edilen artıklardır. Tarım ürünleri sebze, meyve, et, mahsul, kümes hayvanları ve süt ürünlerini içermektedir. Her yıl ortaya çıkan tarımsal atıkları tahmin etmek zor ancak kuşkusuz tarımsal atık, tüm dünyada üretilen toplam atık maddesinin önemli bir bölümünü oluşturmaktadır. Bu makale, büyük miktarda tarımsal atık miktarını ve yeni kompozit malzemelerin ve diğer uygulamaların sentezlenmesinde rasyonel bir şekilde faydalanarak etkin bir şekilde nasıl yönetilebileceğini incelemektedir. Sadece bu büyük miktardaki tarımsal atığın elden çıkarılması sorununu çözmez, aynı zamanda sürdürülebilir çevre için bir çözüm sunar. Tarımdaki herhangi bir gelişmeye, daima farklı tarım yöntemleri ve işleme teknikleri tarafından üretilen atıklar eşlik eder. Tarımsal atıklar ekimde kimyasalların yaygın olarak kullanılması ve tarımsal atıkların yakılması veya toprağın doldurulmasıyla irrasyonel bertarafı nedeniyle de kullanılır. Çevreyi ve toprağın verimliliğini kötü etkiler. Bu yazıda ayrıca, daha güçlü, daha hafif ve düşük maliyetli olan ve çeşitli endüstriyel uygulamalar için kullanılabilen, matriks olarak Alüminyum ile metal matriksinin kompozit haline getirilmesinde takviye malzemesi olarak bir tarımsal atık Pirinç kabuğunun uygulanması anlatılmaktadır. Kompozitler karıştırma teknikleriyle sentezlenir ve yapısal özellikleri için XRD, SEM ve optik mikroskopi ile karakterize edilir. Pirinç Kabuğu Külü, takviye malzemesi olarak ağırlıkça% 3'lük Alüminyum metalinden alınmıştır. Sertlik, Young modülü gibi mekanik özellikler de Vicker'ın Sertlik test cihazı kullanılarak değerlendirilmiştir.

Agro Waste Reinforced Composites: A Solution For Sustainable Environment

Keywords

Agrowaste; Rice husk; Metal matrix composites; Stir cast technique; XRD; SEM.

Abstract

Agro- wastes or agricultural wastes are the residuals obtained when raw agriculture products are grown and processed. The agriculture products include vegetable, fruits, , meat, crops, poultry and dairy products. Its difficult to estimate the agriculture waste arising every year but undoubtedly agro waste constitutes a significant volume of the total waste matter generated in the entire world. This article reviews the huge amount of agro waste and how it can be managed effectively by making rational use in synthesizing novel composite materials and other application. It not only solves the major problem of disposal of this huge amount of agro-waste but also offers a solution for sustainable environment. Any development in agricultural is always accompanied by wastes generated by different farming methods and processing techniques. Agro waste is also generated because of extensive use of chemicals in cultivation and irrational disposal of agro waste by burning or land filling. It badly affects the environment and the fertility of the soil. This paper also describes the application of an agro –waste Rice husk as reinforcement material in making metal matrix composite with Aluminium as matrix which is stronger, lighter and low cost and can be used for various industrial applications. The composites are synthesized by stir cast techniques and characterized by XRD, SEM and optical microscopy for their structural properties. The Rice Husk Ash was taken as 3% wt of the Aluminium metal as reinforcement material. The mechanical properties like Hardness, Young's modulus etc are also evaluated using Vicker's Hardness tester.

© Afyon Kocatepe Üniversitesi

1.Introduction

Agro- wastes or agricultural wastes are the residuals obtained when raw agriculture products are grown and processed . The agriculture products include vegetable, fruits, , meat, crops, poultry and dairy products (Obi et al.2016). Agro-waste includes animal waste (manure, animal carcasses), food processing waste for example only 20% of maize is canned while 80% is discarded as waste, crop waste such as corn stalks, sugarcane bagasse etc and toxic agricultural waste which includes insecticides, pesticides, and herbicides, etc. According to a research study it is estimated that about 998 million tonnes of agricultural waste is produced annually (Agamuthu 2009).

Agro-wastes which are the by-products ofagricultural produce, can be husk, straw, cobs or fiber (Abubakar and Ahmad 2010, Zurina et al.2004).Various agricultural activities generate waste such as cultivation, livestock production, aquaculture etc. The agro waste materials can be managed properly using 3R principle of Agriculture Waste Management System. "3Rs" stands for Reduce, Reuse and Recycle of the waste. These wastes can be transformed into useful materials for human and agricultural usage. With the huge amount of waste being produced, it has become essential to take necessary steps to save environment from further damage by unthoughtful disposal of such waste.

The agro – wastes are generated by any of the following activities:

- Wastes from Cultivation Activities
- Wastes from Livestock Production
- Waste utilization routes
- Fertilizer Application
- Anaerobic Digestion
- Adsorbents in the Elimination of Heavy Metals
- Pyrolysis
- Animal feed
- Direct combustion

Almost 52.5% of the agro waste materials are used as land fillings , 25.8% are recycled, 8.9 are used for composting and 12.8% are used for combustion process. However, Agro-wastes can be used for the production of Biogas, bio fertilizer, extraction of various minerals etc. Some more applications of agro wastes are as mentioned below:

- Rice Husk Ash - As reinforcement material Additive in cement mixes, Water glass manufacture, Active carbon, synthesis of composite materials
- Banana Peel & Sugarcane fibers –In making Paper pulp
- Onion skin, Groundnut husk – To remove heavy metals
- Husk, Straw, Cow Dung – Biogas production, Electricity generation
- Animal waste(dung) – Compost, fertilizer

Use of Agro – waste as fillers in Composite Materials

With the advancement in technology, there is a huge demand for novel materials with improved and customised properties which are not offered by traditional materials. Material scientists are researching for new materials and processing techniques of hybrid and composite materials which are stronger, lighter and with so many other properties and are highly functional (Laad and Jatti, 2015) Composites materials comprise of two or more types of materials with different properties and the properties of the composite material is superior to the properties of constituent materias. The composites with agro waste and natural fibers exhibit improved water and oxygen barrier, enhanced mechanical strength,

better dimensional stability, higher thermal, chemical and wear resistance etc (Ates et al. 2008). In industrial applications, agro waste fiber reinforced thermoplastic composites are very popular construction and automobile industries, and other consumer applications because of their improved properties and low cost (Dominiqueet al. 2012, Panthapulakkal 2005). A research study has shown that underutilized agro-waste are significant resources of lignocelluloses materials, such as millet, rice, wheat, corn straw, cocoa husk, corncobs and fiber (Tsai et al. 1998, Wang and Sun 2002, Yang et al., 2006). Natural fibres, such as hemp, flax, jute and kenaf have good strength and stiffness, and much lighter in comparison with other reinforcement materials such as glass fibres. The use of natural fibers in making composite materials grew rapidly specially in construction industry. The use of agro-waste for developing novel composite materials to be used for various industrial applications provides a solution which not only reduces the use of natural resources but also saves energy. In this research study the reinforcement material is rice husk ash which is added to the aluminium alloy matrix to synthesize a metal matrix composite.

Rice husk (RH) is a major source of silica, which is naturally available through agricultural by-product advocates the sustainable development. In most of the rice producing countries, the rice husk, which is obtained after the processing of rice is either burnt as fuel in the boilers or used in the landfills. (Laad et al. 2015) .Applicability of RH in metalworking will be contemporary, eco-friendly and will complement the industries. For the most part RH gets desolated by either dumping or burning, but recently many practices have emerged for its equitable applications. A technique, to utilise RH as reinforcement for Metal Matrix Composite was explored to obtain a hybrid material, which incorporated the preparation of RHA (Rice Husk Ash) and the stir casting method to attain the MMC. Aluminium was used as the base metal for the metal matrix which was melted and RHA was added along with Magnesium.

2. **Materialsand Methods**

The synthesis of Al-RHA requireed Aluminium alloy in powder form, Rice Husk Ash and Magnesium as wetting agent. The synthesis of metal matrix composite involved following steps.

2.1 Preparation of Rice Husk Ash (RHA)

The Rice husk was sieved using mesh size of 300 microns to remove the impurities like Rice particles, Rice plant particles. The Rice Husk was burned in an electrical furnace at 600 ^{0} C for 2 hours till all the organic, volatile material present in the Rice husk was burnt and the husk turned white in colour. The ash obtained was almost 20% of the total weight of the rice husk which was burnt in the furnace. Rice Husk Ash was then sieved using sieves of different mesh size. Different size of RHA was obtained, which were 180 microns, 110 microns, 90 microns, 45 microns. About 30% of the total RHA was of size 45 microns, 50% of 90 microns and 20% above 90 microns.

2.2 Preparation of Metal Matrix Composites reinforced with Rice husk ash

For synthesis of MMC with Aluminium as matrix metal, RHA was taken 3% wt and Magnesium powder 1.5 wt % of Aluminium alloy. Initially, Al alloy was charged into the graphite crucible and heated to about 750 ^{0}C till the entire alloy in the crucible was melted.The reinforcement particles (RHA) were preheated to 800^{0}C for 30 minutes before incorporation into the melt. As wetting agent 1.5 wt % magnesium was also added to the melt simultaneously. A stirrer was used to stir the molten metal at a speed of 500 -700 rpm for uniform distribution of rice husk ash in the moltem metal. The preheated RHA particles were added into the molten metal at a constant rate during the stirring time. The mixture was poured into the mould uniform solidification. Using this process 3% RHA particle-reinforced composites were produced. The Vicker's Hardness tests were performed on the Aluminium and on the composite to evaluate the mechanical properties and results were compared. The composite sample were subjected to Optical microscopy, SEM and

XRD to know the composition and structural properties.

3 Results and Discussion

3.1 Hardness Measurement

Vickers hardness tester was used to measure the hardness of Al-RHA composite. A significant increase in hardness of the alloy matrix was seen with addition of RHA. It suggests that the presence of RHA in the aluminium alloy matrix improved the overall hardness of the composite material. It can be concluded that the presence of stiffer and harder RHA as filler material is responsible for the increase in resistance to plastic deformation of the matrix. The hardness of Aluminium alloy was measured to be 23.17 VHN which increased to 26.93 VHN when reinforced with rice husk ash. Young's modulus also found to be improved from 137.315 MPa to 151.493 MPa

3.2 XRD Measurement

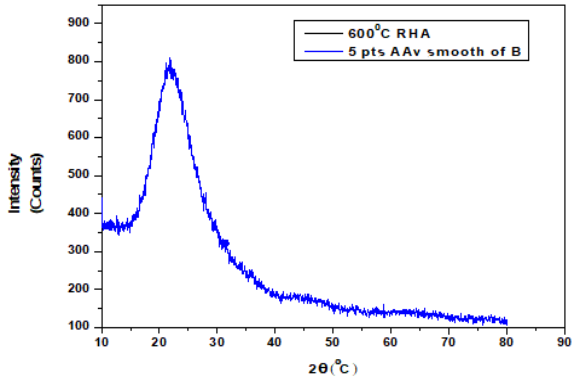

Figure 1. The Al-RHA composite of XRD peaks.

The major constituent of RHA is silica. It was observed that the crystallinity of silica in RHA depends upon incineration temperature. As per the XRD spectroscopy at 600^0C, it shows the amorphous character of silica in RHA. Its due to the fact that at temperature 600^0 C, the ash obtained had some residual half burnt carbonious material. When rice husk is burnt in the furnace, the volatile matter such as lignin, cellulose, hemicelluloses do not burn completely at this lower temperature. That's the prime reseason for the amorphous character of Rice husk when insinerated at lower temperatures. The brittle behaviour of RHA can be attributed to its glass like amorphous structure.

3.3 Surface Morphology & Micro structural Study of RHA using SEM

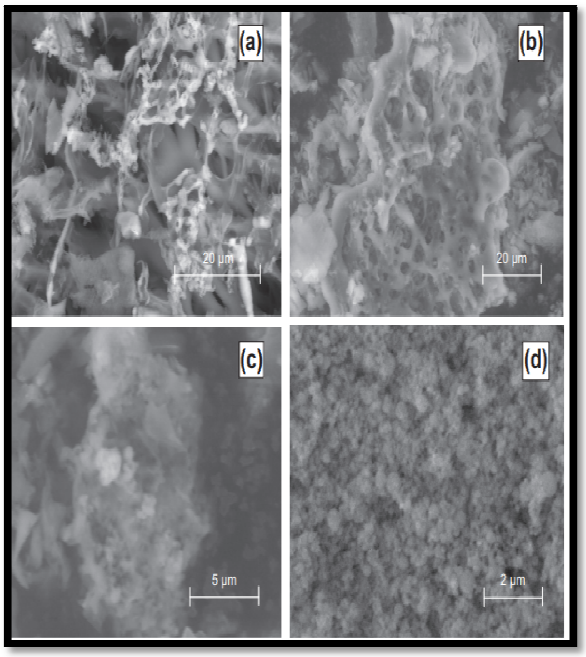

Figure 2. Micro structural Study of RHA using SEM

SEM image of RHA shows the presence of irregular, sharp edges with angular and cuboidal shaped particles with size varying from 5 micrometer to 10 micrometer. It has highly porous structure with homogeneous particle distribution. The presence of micron size particles is also observed together with some other bigger particles.

3.4 Optical Microscopy

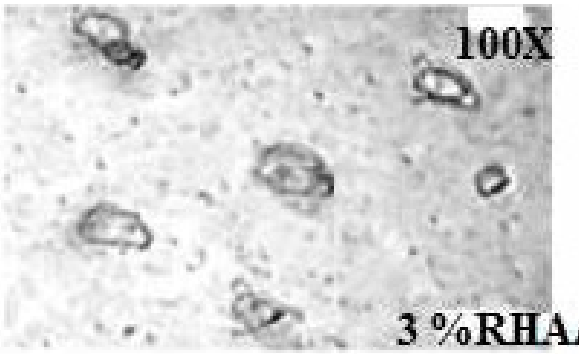

Figure 3. Micro structural Study of RHA using Optical Microscopy

Above figure shows the optical micrograph of Al-RHA composite. It shows that RHA is uniformly distributed in the Al alloy matrix.

4. Conclusion

The rate and volume with which the contribution of agro waste is growing in the total waste matter of the world, its alarming situation which calls for serious thought on the rational waste management techniques and use of agro waste in the best possible manner which will constructively help the human kind and animals and also save the environment. The agro-waste rice husk which is abundantly available in all the rice producing countries is successfully used for extraction of rice husk ash and lighter and stronger Aluminium alloy-RHA composites were synthesized which were characterized for their composition, structural and mechanical properties using various techniques. The hardness of Al alloy –RHA composite was found to be increased in comparison with that of unreinforced Al alloy. Also it was revealed that RHA reinforced composites had higher hardness value and lesser in density compared to Al alloywhich indicates that the composite reinforced with RHA is lighter than the aluminium alloy. Thus the Al alloy-RHA composites have improved mechanical and structural properties and may find applications in automobile, aerospace,construction and biomedical industries where materials with increased mechanical strength but lighter in weight are much in demand. Moreover, due to partial replacement of the expensive metal alloy with RHA the cost of the composite will also be significantly reduced. Thus, RHA can not only be used as reinforcement material in the fabrication of lighter, low cost and high performance MMCs but also it will solve the problem of disposal of this abundantly available agro waste and save the environment. This study paves the way for finding suitable applications of all the available agro- waste and save our environment.

5. References

Abubakar, M.S., Ahmad, D., 2010. Pattern of Energy Con- sumption in Millet Production for Selected Farms in Ji- gawa, Nigeria. *Australia Journal of Applied Sciences*, 4, 4, 665-672.

Agamuthu, P., 2009. Challenges and opportunities in Agrowaste management: An Asian perspective. *Inaugural meeting of First Regional 3R Forum in Asia* 11 -12 Nov., Tokyo, Japan.

Ates,S., Ni Y., Tozluoglu, A., 2008. Characterization and Evaluation of Paulownia Elongata as a Raw Material for Paper Production. *African Journal of Biotechnology*, 7, 22, 4153-4158.

D. Wang, D., Sun, X.S.,Low, 2002. Density Particle Board from Wheat Straw and Corn Pith, *Journal of Industrial Crops Product,* 15, 1, 43-50.

H. S. Yang, H., S., Kim, H. J., Park, H. J., Lee J, Hwang,T.S.,(2006).Water Absorption Behaviour and Mechanical Properties of Lignocellulosic Filler—Polyolefin Bio-Com- Posites, *Journal of Composite Structures*, 72, 4,429-437.

Laad, M., Jatti, V.K., 2015. Investigation into the effect of Aluminium powder on Mechanical, Tribological and Electrical properties of Al-ABS composites Wseas, *Transactions on Applied and Theoritical Mechanics*, 10, 47-53.

Laad, M., Jatti, V.S., Yadav, S. 2015. Comparative Study between SiC between Al 64430 metal matrix composites and RHA reinforced Al64430 metal matrix composites. *Advanced Materials Research,* 1119, 234-238.

M. R. Dominique, M.R., Georget, D.M.R., Elmoneim,O., A. E. O. Elkhalifa, A.E. Q., Beltom, P.O., 2012. Structural Changes in Kafirin Extracted from a White Type II Tannin Sor-ghum, *Journal of Cereal Science*, 57, 48, 106-111.

Panthapulakkal, S., Sain, M., Law, S., 2005. Enhancement of Processability of Rice Husk Filled High Density Polyeth- ylene Composites Profiles, *Journal of Thermoplastic Composite Material*, 18, 5, 445-459.

Tsai, W.T., Chang, C.Y., Lee, S.L., 1998. A Low Cost Absorbent from Agricultural Wastes Corn Cob by Zinc Chloride Activation, *Journal of Biotechnology*, 64, 34, 211-217.

Zurina, M., Ismail H., Bakar A.A., 2004. Rice Husk Filled Powder Polystyrene/Styrene Butadiene Rubber Blends, *Journal of Applied Polymer Science*, 81, 63, 2004, pp. 742-753.

Afyon Kocatepe Üniversitesi Uluslararası Mühendislik Teknolojileri ve Uygulamalı Bilimler Dergisi

Afyon Kocatepe University International Journal of Engineering Technology and Applied Sciences

AKÜ IJETAS Vol **2** (2019) Haziran (34-44 s) AKU J.Eng.App.Sci. **Vol 2** (2019) June (34-44 pp)

Araştırma Makalesi / Research Article

Küresel Bombeli Basınçlı Kap Analiz ve Tasarımı

Hasan Huseyin OZKAN[1], Safa OZHAN[1], Garip GENC[2]

[1]*Cimtas Pipe Fabrication and Trading Ltd. Co. R&D Center, Bursa Free Zone, Gemlik/Bursa, Turkey*
[2]*Marmara University, Technology Faculty, Mechatronics Engineering Department, Istanbul, Turkey*

e-posta: ggenc@marmara.edu.tr

Geliş Tarihi:29.04.2019 ; Kabul Tarihi:30.05.2019

Anahtar kelimeler
İç Basınca Maruz Basınçlı Kaplar; Sonlu Elemanlar Yöntemi; Formüller ile Tasarım; Analiz ile Tasarım

Özet

Bu çalışmada küresel bombe merkezinde ve kaynaklı plaka ile takviyelenmiş bir nozul açıklığı iç basınç yüklemesi altında sonlu elemanlar yöntemiyle tasarım prosedürünü anlamak amacıyla incelenmiştir. Bu prosedür ASME Boiler and Pressure Vessel Code Section VIII Division 2 standardına göre ele alınmıştır. Bu standart ilki "Formüller ile Tasarım" ve ikincisi "Analiz ile Tasarım" olmak üzere basınçlı kap tasarımı için iki farklı kısım içerir. ASME standardı referans alınarak, "Plastik Çökme" ve "Lokal Hasar" hasar modlarına karşı dayanımı doğrulamak için aksisimetrik sonlu eleman modelleri ile elastik, limit yük ve elastik-plastik analiz yöntemleri kullanılmıştır. Maksimum izin verilen basınçlar bu analiz yöntemlerine göre elde edilmiş ve değerlendirilmiştir. Elastik ve limit yük analiz metodlarına göre elde edilen plastik çökme sonuçları birbirine çok yakındır. Bunun yanında plastik çökme hasar modu için elastik analiz yönteminin elastik-plastik analiz yöntemine göre daha konservatif sonuçlar verdiği gözlemlenmiştir. Diğer yandan, lokal hasar modu için elastik-plastik analiz yönteminin elastik analize göre nispeten konservatif olduğu gözlemlenmiştir.

Analysis and Design of Hemispherical Head Pressure Vessel

Keywords
Internally Pressurized Pressure Vessels; Finite Element Method; Design by Rules; Design by Analysis

Abstract

In this study, a hemispherical head with pad reinforced central nozzle opening that subjected to uniform internal pressure was investigated using Finite Element Methods (FEM) to understand the design procedure. This procedure is handled according to the ASME Boiler and Pressure Vessel Code Section VIII Division 2. This standard contains two parts for the design of pressure vessels, the first part is Design by rules and the second part is Design by analysis. With reference to the ASME standard, axisymmetric finite element models for Elastic, Limit Load and Elastic-Plastic Analysis are used to demonstrate protection against plastic collapse and local failure. Maximum allowable pressures are obtained in accordance with the mentioned design methods and discussed. According to the elastic and limit load analysis methods, obtained plastic collapse results are very close. Besides, the elastic analysis method is observed to be more conservative than the Elastic-Plastic method regarding the evaluation of plastic collapse. On the other hand, for the local failure results, Elastic-Plastic Analysis is observed to be slightly conservative than the Elastic Analysis.

© Afyon Kocatepe Üniversitesi

1 Introduction

The pressure vessels, which are subjected to internal or external pressure, are used to store fluids such as oil, petroleum, and chemical. The risks which depending on the usage places of pressure vessels make these structural elements important engineering equipment. The failure of pressure vessels may cause serious damage; therefore, pressure vessel design criteria and design steps gain significance. ASME standards are widely used for the design of these kinds of tubes. When the literature is examined, many studies

have been done to design pressure vessels using ASME codes (Bhagyashri and Mishra, 2015; Dhalla and Jones, 1986; Sunil Kumar and Suhas, 2016; Thakkar and Thakkar, 2012). Also, valuable studies which focused on design parameters of pressure tubes (such as their geometries) are found in the literature. For example, Agrawal and Ganesh Narayanan (2018) studied on an analysis of pull-out tests of Mild Steel tube stainless sheet joint fabricated by tube end forming. They observed that the end formed joint fails by joint unlocking, while it is a physical failure in case of the welded structure. Olszewski et al. (2018) carried out the analysis, project, and experimental examination of an original rigid riser for Coil Tubing Pipes. According to the present conclusion in this study, the theoretical and experimental examination has shown that the designed riser meets all adopted design assumptions, which proves its serviceability. Sharifi et al. (2018) focused on the effect of dome geometrical shape such as hemispherical, torispherical, and ellipsoidal domes, on mechanical deformation and cracked length of laminated woven reinforced polymer composite pressure vessels under low-velocity impact and internal pressure. According to the presented results in this study, the maximum and the minimum crack lengths also take place in torispherical and hemispherical domes, respectively. In another study of Sharifi et al. (2016), strain deformation of three types of internally pressurized laminated composite shells (hemispherical, ellipsoidal, and torispherical) with two types of woven roving stacking sequence was carried out numerically and experimentally in this study. According to the presented results in this study, laminated hemispherical shells were also found to be the preferred choice against mechanical failure while laminated torispherical shells were found to be the least choice.

In this study, a hemispherical head with a pad reinforced nozzle opening subjected to the uniform internal pressure is designed in accordance with Part 4 requirements. Then, the same design is evaluated with Part 5 Design by Analysis methods of (ASME, 2017c) in order to compare the different design methods provided by this ASME standard.

2 Material and Method

A finite element model is developed in order to apply the design by analysis methods. Details of the FEM model such as geometry, mesh modeling, boundary conditions, material properties are briefly explained. All applicable loads on the component shall be considered when performing a design-by-analysis. The load case definition shall be included in the User's Design Specification. For this problem, two load cases are evaluated. For the first load case, design pressure, 3.6 MPa, is considered at 300°C. The second load case is shutdown case at 20°C. It should be noted that the effects of deadweight and hydrostatic pressure are neglected.

2.1 Finite Element Model

The details of the finite element model are provided within this section. The same finite element model is used as elastic, limit-load, elastic-plastic analysis models except for that magnitude of the applied internal pressure, material properties and exclusion of the nonlinear geometric effects are defined in conjunction with the corresponding analysis method.

In this section, the development stages of the finite element model starting with the geometry basis to analysis is explained. Abaqus software is used for modeling, preprocessing and post-processing of the model.

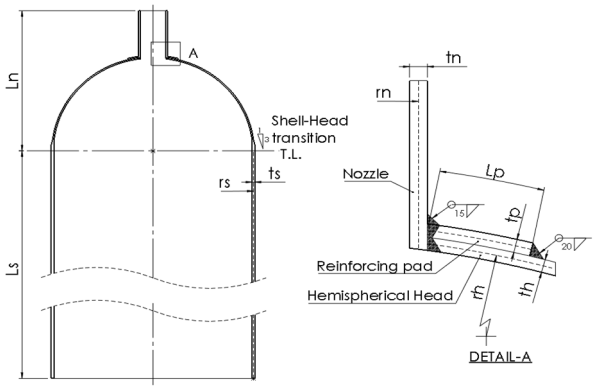

Figure 1. Geometry details basis to analysis

In Figure 1, the geometry and dimensional notation of the hemispherical head and the nozzle opening is shown. Values of these dimensions are also defined in Table 1.

Table 1. Dimensions of the model

Definition	Dimension [mm]
t_h: thickness of the hemispherical head	20
t_n: thickness of the nozzle	25.4
t_p: thickness of the reinforcing pad	20
t_s: thickness of the cylindrical shell	40
r_h: mean radius of the spherical shell	1420
r_n: mean radius of the round nozzle	190.5
r_s: mean radius of the cylindrical shell	1420
L_n: nozzle projection distance from the tangent line	2130
L_s: cylindrical shell length from the tangent	8000
L_p: width of the reinforcing pad	150

An axisymmetric finite element model is developed for this geometry. Axisymmetric elements provide for the modeling of the bodies of revolution under axially symmetric loading conditions. For this problem, the internal pressure loading and geometry is suitable for axisymmetric modeling. Axisymmetric elements are described in cylindrical polar coordinates r, z, θ denoted by 1, 2, 3 respectively. Cross-sectional model is developed in θ=0. The radial and axial coordinates of a point on this cross-section are denoted by r and z, respectively. At θ=0, the radial and axial coordinates coincide with the global Cartesian X and Y coordinates. The elements in this problem have following degree of freedoms; translations about Cartesian X (U1) and Cartesian Y (U2) directions and rotation about Cartesian Z direction (UR3) only.

Boundary conditions applied to the model are shown in Figure 2. Axial lengths of the cylindrical shell (L_s) and nozzle (L_n) are kept long enough in order to remove the effects of boundary conditions on the stress results obtained at the nozzle-head junction and shell head-transition regions. A hemispherical cap is modeled at nozzle end in order to involve the pressure thrust load acting on the junction.

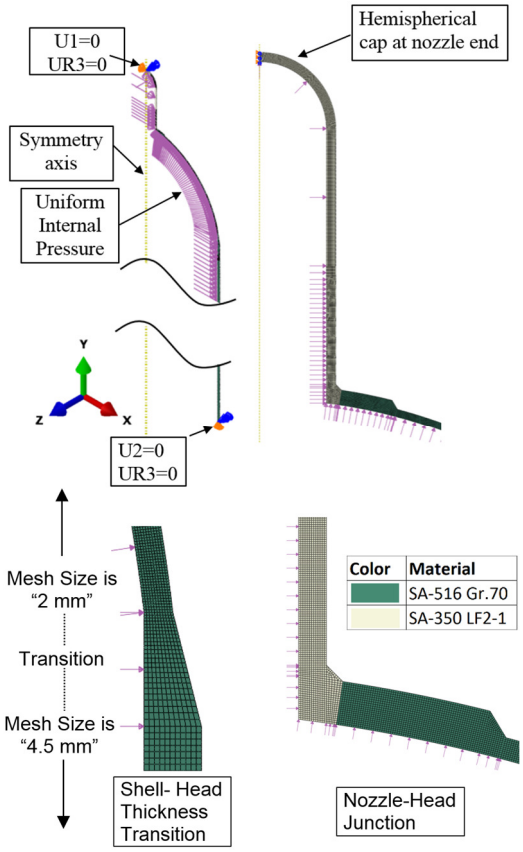

Figure 2. Finite Element Model

Materials assigned to the model regions are also shown in Figure 2. The material properties assigned to these material regions and applied internal pressures are given under corresponding design by analysis method. The reinforcing pad is assumed to be integral with the head. For the nozzle weld, considering the allowable stress of the materials, property of the weaker one of the connecting materials is assigned. Also, weld joint efficiency per (ASME, 2017c) is 1.0; therefore it is neglected in the evaluations.

CAX8R 8-node biquadratic, reduced integration axisymmetric solid elements used for mesh modeling. A global mesh size of "2 mm" for the regions above shell-head transition and a global mesh size of "4.5 mm" is used regions under the shell-head transition. The total number of elements used in the model is 37916, and average aspect ratio of all element is 1.16. The aspect ratio for all elements is less than 2.0.

2.2 *Elastic Analysis Method*

By the Elastic analysis method, protection against plastic collapse and local failure are demonstrated. Also, a ratcheting assessment is required even if the equipment is not in cyclic service.

An internal pressure load equal to the design pressure, 3.6 MPa, is applied to the pressure boundaries. Linear, elastic and isotropic material properties are utilized for this method. Considering the carbon content of the materials listed by (ASME, 2017a) and according to the Table TM-1 and Table PRD of (ASME, 2017b), assigned modulus of elasticity is 185000 MPa, and the Poisson's ratio is 0.3 for both materials.

A static-stress displacement analysis is run neglecting the nonlinear geometric effects. Initial and deformed shapes of the model and the maximum stress location are shown in Figure 3.

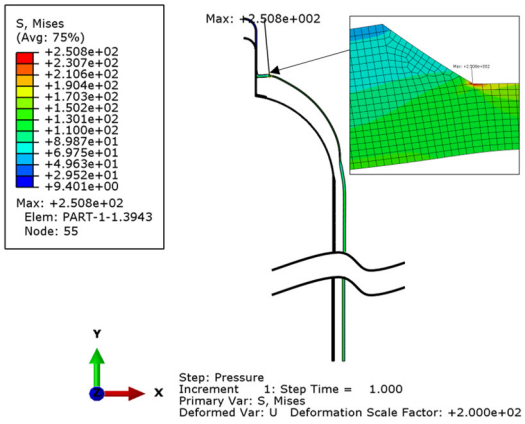

Figure 3. Elastic Nodal Averaged Stress and Displacement (x200 scaled) Results

As seen in Figure 3, the nozzle end is free only in the axial direction, and shell bottom edge is free only in the radial direction in accordance with the applied boundary conditions.

If a detailed stress analysis such as finite element analysis performed using a numerical method, the stress results typically provide a combination of P_L+P_b (at locations away from discontinuities) and P_L+P_b+Q+F (at structural discontinuities or stress concentrations) directly. In order to derive the membrane, bending and peak components of stress distribution, stress linearization shall be performed. There are several options regarding the stress linearization procedure which are listed by (ASME, 2017c) and WRC429 (Hechmer and Hollinger, 1998). Structural stress method based on stress integration is recommended by (ASME, 2017c); this method is applied for stress linearization.

To produce valid membrane and bending stresses, there are some guidelines in Annex 5-A of (ASME, 2017c) for selecting the appropriate locations and orientations of SCLs. Regarding the orientation of the SCLs, the endpoints of the line should be chosen so that the section is normal to the interior and exterior surfaces of the model. This orientation minimizes problems with shear stresses since they will be approximately zero at the ends of the line (ASME, 2017c). Applied stress linearization lines along the model are shown in Figure 4.

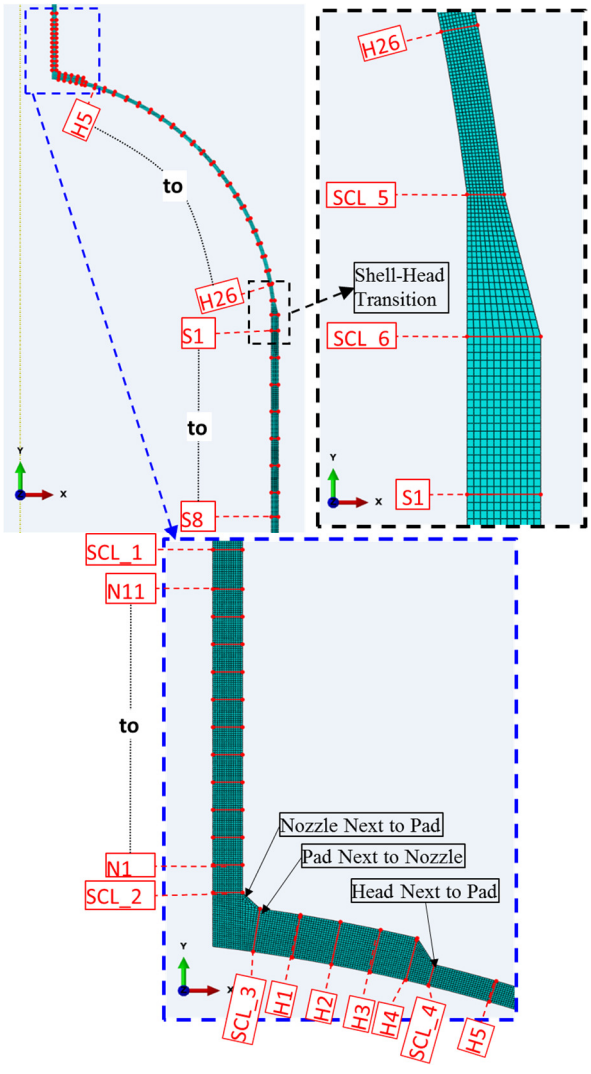

Figure 4. Stress Classification Lines (SCLs)

Obtained Von Mises equivalent linearized stresses and the allowable limits (S, SPL, SPS) along the model are depicted in Figure 5. The allowable limit "S" on general primary membrane equivalent stress (P_m), and the allowable limit "SPL" on local primary membrane (P_L) and primary general or local membrane plus primary bending equivalent stresses (P_L+P_b) are to be satisfied in order to demonstrate protection against plastic collapse. Secondary equivalent stress (Q) and additional equivalent stress produced by a stress concentration and above the nominal "P+Q" stress level (F) do not need to be determined to evaluate protection against plastic collapse. However, these equivalent stresses are needed to be evaluated for fatigue and ratcheting evaluations.

The allowable limits S, SPL and SPS on corresponding equivalent stresses are obtained in accordance with (ASME, 2017c). The hot (300°C) and cold (20°C) load cases are considered for the calculation of these allowable limits. Considering the internal pressure & hot loading case and cold & shutdown case, SPS is calculated in order to demonstrate protection against ratcheting.

Calculated values S, SPL, SPS parameters in accordance with (ASME, 2017c) are given in Table 2. The subscript "n" denotes for the nozzle and the material SA-350 Gr. LF-2 Cl.1, the subscript "s" denotes for head and shell and the material is SA-516 Gr.70.

Table 2. Values of S, SPL, SPS

Parameter	Value (MPa)
S_n	129
S_s	136
SPL_n	194
SPL_s	204
SPS_n	442.0
SPS_s	466.5

Computed linearized equivalent stresses along the SCLs depicted by Figure 4 and the allowable limits S, SPL, SPS for stress categories are demonstrated in Figure 5. For membrane plus bending, membrane plus bending plus peak equivalent stresses and the sum of principals are calculated at inside and outside locations for each classification line, but only the governing of these values are plotted in Figure 5. Membrane equivalent stress obtained by "load controlled loads" are either classified as primary general or local membrane stress, i.e., P_m or P_L. Similarly, obtained membrane plus bending stresses are either classified as P_L+P_B for locations away from structural discontinuities or P_L+P_B+Q at local structural discontinuities.

Membrane equivalent stresses at structural discontinuities are classified as local primary membrane stress if the following rule of Part 5 of (ASME, 2017c) applies, A region of stress in a component is considered as local if the distance over which the equivalent stress exceeds 1.1S does not extend in the meridional direction more than $(r*t)^{0.5}$. This rule is also demonstrated in Figure 5, $(r*t)^{0.5}$ distances are marked for nozzle, head and shell locations. Bending stresses within structural discontinuities are evaluated as secondary.

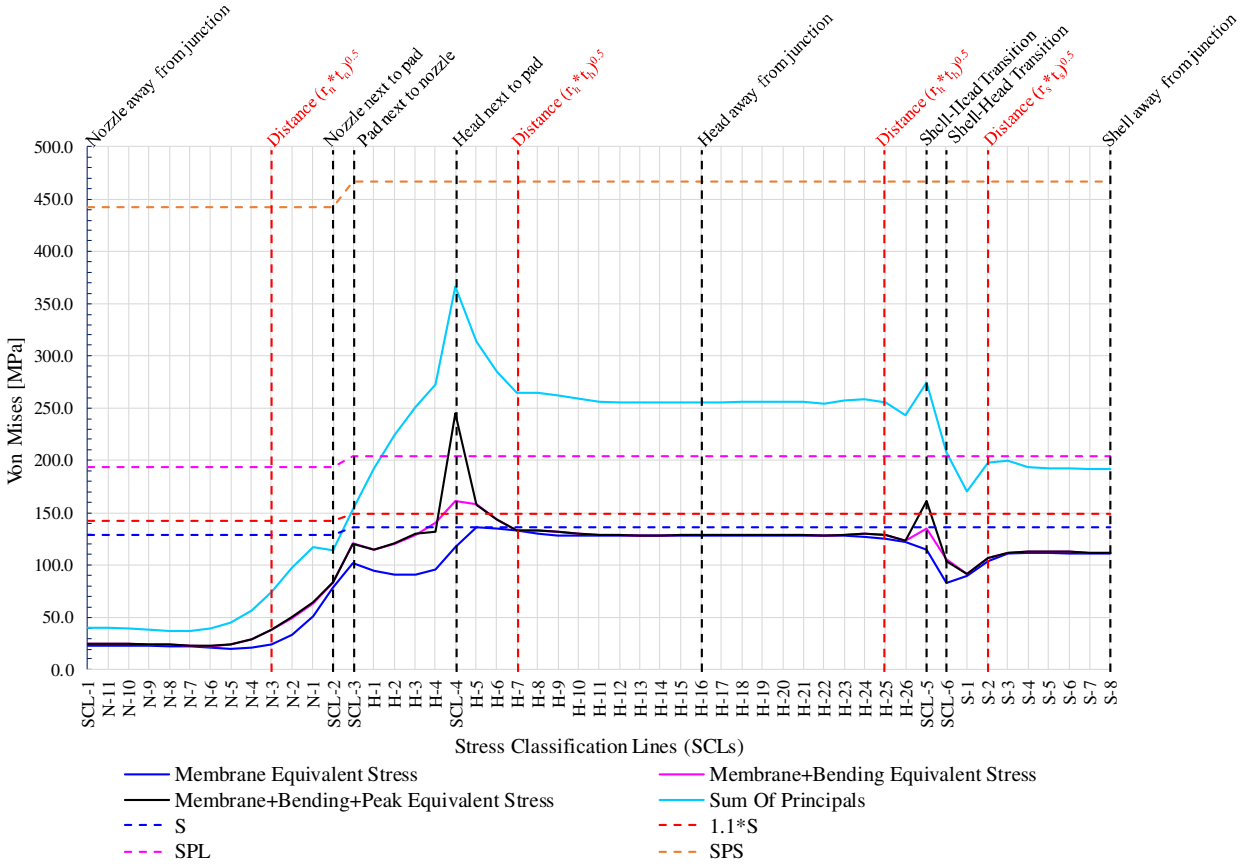

Figure 5. Distribution of the Linearized Equivalent Stresses along the Model

As seen in Figure 5, Membrane (P), membrane plus bending (P+B) and membrane plus bending plus peak (P+B+F) equivalent stresses are nearly coincident at the locations away from structural discontinuities, which shows the general membrane stress characteristics. (P), (P+B) stresses are higher next to the nozzle-pad junction, pad-head and shell-head transition regions which are structural discontinuities. Especially for SCL-4 and SCL-5 (P+B+F) stresses are generated in excess of (P+B) stresses indicate the local stress concentration regions.

Table 3. Elastic Analysis Method: Protection against plastic collapse and ratcheting assessment

SCL	Definition	Membrane equivalent stress				Membrane plus bending equivalent stress			
		Category	Limit	Stress [MPa]	% Uti.	Category	Limit	Stress [MPa]	% Uti.
SCL-1	Nozzle away from junction	P_m	S_n	23.4	18.1	P_L+P_b	SPL_n	24.9	12.9
SCL-2	Nozzle next to pad	P_L	SPL_n	78.9	40.7	P_L+P_b+Q	SPS_n	83.6	18.9
SCL-3	Pad next to nozzle	P_L	SPL_s	101.9	50.0	P_L+P_b+Q	SPS_s	120.9	25.9
SCL-4	Head next to pad	P_L	SPL_s	117.4	57.6	**P_L+P_b+Q**	SPS_s	161.5	**34.6**
H-16	Head away from junction	**P_m**	S_s	127.8	**94.0**	P_L+P_b	SPL_s	128.7	63.1
SCL-5	Shell-Head Transition	P_L	SPL_s	115.2	56.5	P_L+P_b+Q	SPS_s	135.0	28.9
SCL-6	Shell-Head Transition	P_L	SPL_s	82.7	40.5	P_L+P_b+Q	SPS_s	105.4	22.6
S-8	Shell away from junction	P_m	S_s	110.6	81.3	P_L+P_b	SPL_s	112.2	55.0

Categorized stresses and comparison of these stresses to their corresponding allowable limits are summarized in Table 3. In Table 3, primary stress evaluations (P_m, P_L, and P_L+P_b) are satisfied to demonstrate the protection against plastic collapse. The P_L+P_b+Q stress evaluations are for ratcheting assessment.

The protection against local failure is demonstrated in Table 4. It should be noted that

elastic local failure assessment uses only the primary membrane plus bending stresses.

Table 4. Elastic Analysis Method: Protection against local failure

SCL	Definition	Elastic Local Failure Criteria		
		Limit	Sum of Principals [MPa]	% Uti.
SCL-1	Nozzle away from the	$4S_n$	40.4	7.8
SCL-2	Nozzle next to pad	$4S_n$	113.6	22.0
SCL-3	Pad next to the nozzle	$4S_s$	153.4	28.2
SCL-4	Head next to pad	**$4S_s$**	**366.2**	**67.3**
H-16	Head away from the	$4S_s$	255.5	47.0
SCL-5	Shell-Head Transition	$4S_s$	274.0	50.4
SCL-6	Shell-Head Transition	$4S_s$	208.2	38.3
S-8	Shell away from the	$4S_s$	191.8	35.3

The protection against local failure may not be demonstrated if the design details are in accordance with Part 4 of (ASME, 2017c). However, all parts designed in accordance with Part 5 of (ASME, 2017c) shall be protected against local failure. In other words, protection against local failure shall be demonstrated for non-standard design details.

2.3 Limit Load Analysis

For the limit load analysis (LLA), elastic-perfectly plastic (no strain hardening behavior) material models are utilized as shown in Figure 6. 1.5*S yield strength is assigned for each of the materials in construction. The small-displacement theory is used for analysis; in other words, nonlinear geometric effects are not considered. This is mainly due to that pressure loading causes the structures to stiffen, and LLA method is not recommended for the cases which stiffness of the structure reduces by the applied loading.

LLA is essentially an alternative to the elastic analysis to perform protection against plastic collapse to limit the primary stresses. For the internal pressure loading, the load factor to apply is 1.5 in accordance with (ASME, 2017c).

The pressure load causes the solver to diverge is the lower bound limit load of the structure. The equilibrium conditions are not satisfied for a small increase in the load, i.e., if the yield strength is reached over an entire cross-section, calculated displacements are infinite since the tangent modulus is zero.

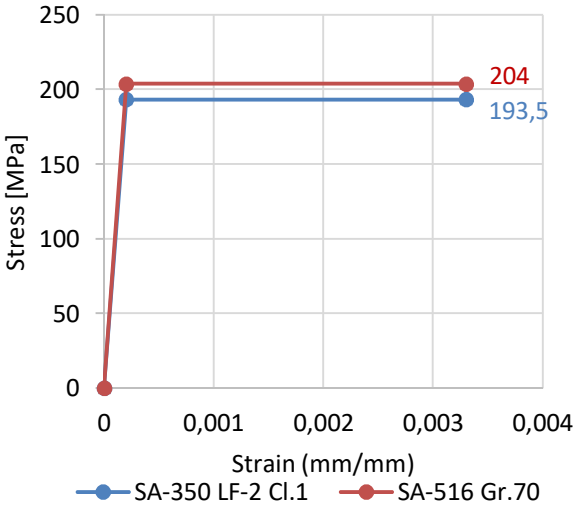

Figure 6. Limit Load Analysis: Material Models

In order to determine the limit load, ten times the design pressure, 36 MPa, is applied to the structure. Considering the minimum required limit load, the plastic collapse utilization is calculated as the 1.5 times the design pressure divided by the determined limit load. Protection against plastic collapse by LLA method is demonstrated as shown in Table 5.

Table 5. Limit Load Analysis Method: Plastic Collapse Utilization

Design Pressure (MPa)	Min Req'd (MPa)	Diverged Pressure (MPa)	Plastic Collapse % Utilization
3.6	5.4	5.75	93.9

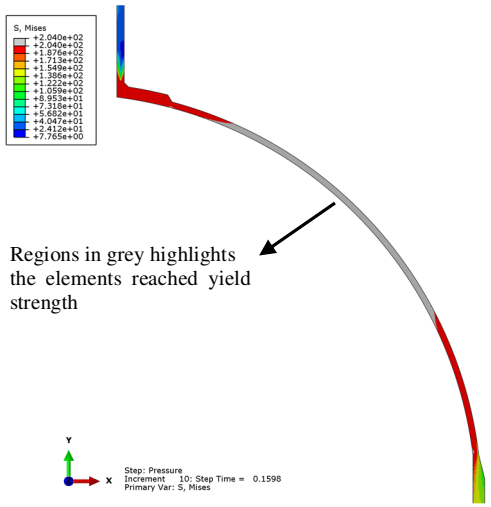

Figure 7. Limit Load Analysis: Divergence location

The region shown in grey in Figure 7 denotes the elements reached the yield strength at collapse pressure. The figure indicates that the head fails due to the general membrane stress.

2.4 Elastic-Plastic Analysis

Elastic-Plastic analysis method is utilized to demonstrate protection against plastic collapse, local failure, and ratcheting. For plastic collapse and local failure evaluation, the isotropic elastic-plastic material behavior involving strain hardening is used by the rules provided in Annex 3-D of (ASME, 2017c) and recommendations in (Peters et al. 2013). The strain of the proportional limit for the elastic-plastic material curves 1E-8. At that limit, true plastic strain is zero. Beyond the true ultimate stress, perfectly plastic material behavior is considered.

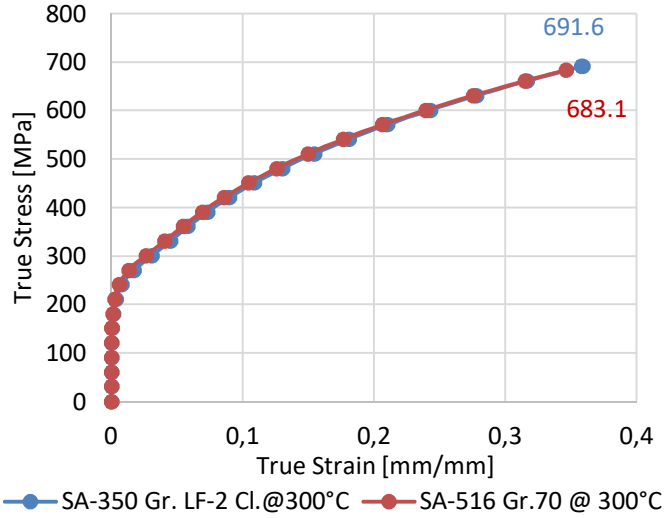

Figure 8. Elastic-Plastic Analysis: True Stress-Strain Curves

Table 6. Elastic-Plastic Analysis Method: Plastic Collapse Utilization

Design Pressure (MPa)	Min Req'd (MPa)	Diverged Pressure (MPa)	Plastic Collapse % Utilization
3.6	8.64	12.33	70.1

The pressure load factor for an elastic-plastic analysis is 2.4, which gives the minimum required pressure to be demonstrated for protection against plastic collapse. The diverged pressure column in Table 6 indicates that the internal pressure load causes the overall structural instability. The ratio of the minimum required collapse pressure, and the diverged pressure gives the plastic collapse utilization per the elastic-plastic analysis method.

In Figure 9, plastic strain distribution at plastic collapse pressure is shown. The elements in grey show the region has reached the plastic strain at true ultimate stress which shows the plastic collapse location.

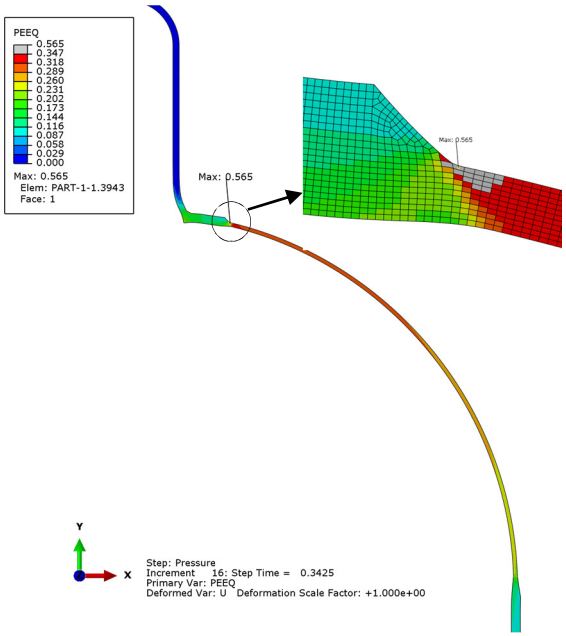

Figure 9. Elastic-Plastic Analysis: Plastic Strain distribution at collapse load

For protection against local failure, strain damage parameter is calculated at gauss points and extrapolated to the nodes for each element. For calculating the strain damage parameter (SLDR), the following are defined in the postprocessor in accordance with (ASME, 2017c).

$(\varepsilon_{peq} + \varepsilon_{cf}) \leq \varepsilon_L$ where,

$$\varepsilon_L = \varepsilon_{Lu} \cdot exp\left[-\left(\frac{\alpha_{sl}}{1+m_2}\right)\left(\left\{\frac{\sigma_1+\sigma_2+\sigma_3}{3\sigma_e}\right\}-\frac{1}{3}\right)\right] \quad \textit{Eq. 1}$$

ε_L: limiting triaxial strain

$\sigma_1, \sigma_2, \sigma_3$: Principal stress components for each point in component

σ_e: Von Mises stress

α_{sl}: 2.2

$m_2 = 0.6 * (1 - R)$, where R is the ratio of yield and ultimate tensile strengths of the material

$\varepsilon_{Lu} = m_2$

ε_{peq}: *total equivalent plastic strain*

ε_L: *limiting triaxial strain*

ε_{cf}: cold forming strain, assumed to be zero

$\left\{\frac{\sigma_1+\sigma_2+\sigma_3}{3\sigma_e}\right\}$ stands for stress triaxiality.

$$SLDR = \frac{(\varepsilon_{peq} + \varepsilon_{cf})}{\varepsilon_L} \leq 1.0 \quad \textit{Eq. 2}$$

The load factor recommended for the elastic-plastic local failure evaluation is 1.7 per (ASME, 2017c). Figure 10 shows the computed local failure ratio at 1.7 times the design pressure. Calculating the strain damage parameter and satisfying the Eq. 2 per the required load cases is sufficient for demonstrating protection against local failure. However, for the purpose of this paper, the limit pressure for the elastic-plastic local failure is also obtained.

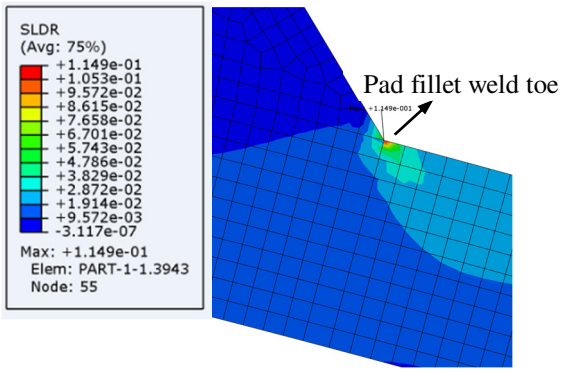

Figure 10. Elastic-Plastic Analysis: Maximum Strain Limit Damage Ratio (SLDR) Location at 6.12 MPa

The SLDR is computed for all the nodes in the model; Figure 10 shows its maximum location.

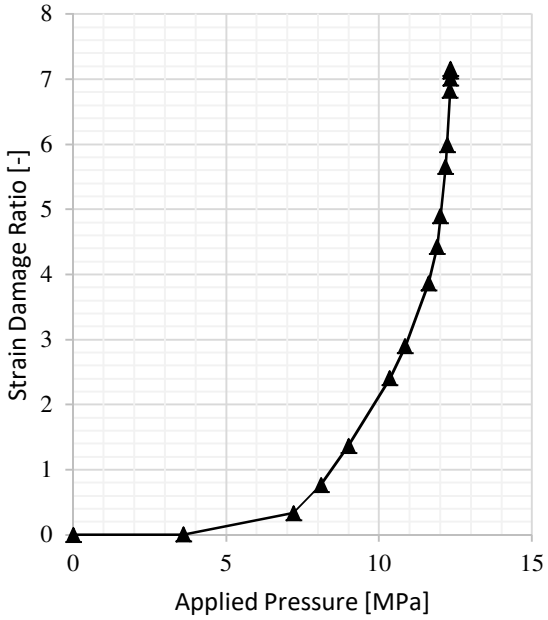

Figure 11. Elastic-Plastic Analysis: Strain Damage Parameters vs Pressure

The pressure load at which strain damage parameter is 1.0 is roughly obtained by calculating the parameter with increasing pressure loading as shown in Figure 11. According to that evaluation, the limiting pressure for local failure evaluation is estimated as 8.4 MPa.

An elastic-plastic ratcheting assessment is also performed. For this evaluation, the design pressure is applied to the model, and elastic-perfectly plastic material behavior is utilized with the Von Mises yield function and flow rule. Also, the effects of non-linear geometry are considered in the analysis. Three pressure cycles are applied to the model as a minimum required several cycles by (ASME, 2017c).

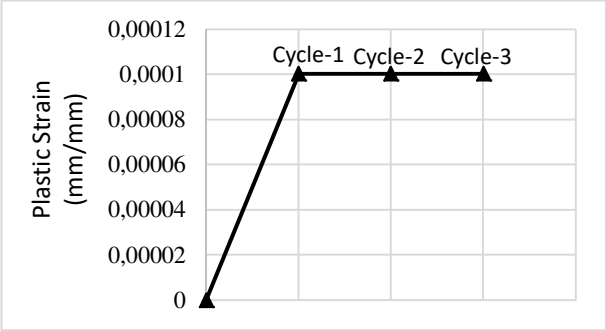

Figure 12. Elastic-Plastic Analysis Method: Ratcheting Assessment, Plastic Strain by Pressure Cycles

As shown in Figure 12, the magnitude of plastic strain does not propagate by pressure cycling; therefore, protection against ratcheting is demonstrated.

2.5 Part 4, Design By Rule Evaluation

For design by rule evaluation in accordance with Part 4 of (ASME, 2017c), only the maximum allowable pressure results are provided as given in Table 7.

Table 7. The maximum allowable pressure computed by Design by Rule requirements

Component	Design Pressure (MPa)	Design Temp. (°C)	Maximum Allowable Pressure (MPa)
Head	3.6	300	3.831
Cylinder	3.6	300	3.824
Nozzle	3.6	300	3.814

3 Results

The protection against plastic collapse and local failure are demonstrated by elastic, limit load and elastic-plastic design by analysis (DBA) methods. Also, ratcheting is assessed by Elastic and Elastic-Plastic analysis methods.

Table 8. Obtained Maximum Allowable Pressure by each Design Method

Design Method	Plastic Collapse % Uti.	Local Failure % Uti.	Maximum Allowable Pressure (MPa)
Elastic Analysis	94.0	67.3	3.83
Limit Load Analysis	93.9	67.3*	3.84
Elastic-Plastic Analysis	70.1	72.9	4.94
Design by Rule	-	-	3.814

(*): Local failure criteria check for a limit-load analysis is same as elastic analysis.

The utilization of the applied design pressure and the maximum allowable pressures obtained by each of the design by analysis methods and the design by rule requirements are tabulated in Table 8.

4 Conclusion

According to the elastic and limit load analysis methods, obtained plastic collapse results are very close. Besides, the elastic analysis method is observed to be more conservative than the Elastic-Plastic method regarding the evaluation of plastic collapse. On the other hand, for the local failure results, Elastic-Plastic Analysis is observed to be slightly conservative than the Elastic Analysis. It should be noted that all three methods may be used to qualify a component in accordance with (ASME, 2017c), however, the elastic-plastic method is the most realistic DBA regarding the more realistic material input and included nonlinear geometric effects in the analysis.

The stress linearization and categorization processes for an elastic analysis are more complex compared to the post-processing of other methods and require more effort. Also, it may produce non-conservative results for thick walled ($R/t \leq 4$) pressure vessels. However, preprocessing and solver time for an elastic analysis are lesser compared to the other methods.

Limit load analysis method is shown to be excellent for demonstrating the protection against plastic collapse and may be used for general component sizing. However, similar to the elastic analysis, nonlinear geometric effects are excluded, and the buckling failure mode is not detected by this analysis method.

Predicted plastic collapse load in accordance with the elastic-plastic analysis method is considerably higher compared to the other analysis methods given the involved strain hardening behavior of the ductile material and applied pressure load factor.

Acknowledgment

This research is supported by Cimtas Pipe Fabrication and Trading Ltd. Co. with project number 9208-34.

5 References

Agrawal, A. K., and Ganesh Narayanan, R., 2018. Pull-out tests on tube to sheet joints fabricated by endforming. *Journal of Constructional Steel Research, 144*, 186-197. doi:10.1016/j.jcsr.2018.01.027

ASME. 2017a. Boiler and Pressure Vessel Code, Section II: Materials - Part A: Ferrous Material Specifications. In (Vol. ASME BPVC.II.A-2017): ASME International.

ASME. 2017b. Boiler and Pressure Vessel Code, Section II: Materials - Part D: Properties. In (Vol. ASME BPVC.II.D.C-2017): ASME International.

ASME. 2017c. Boiler and Pressure Vessel Code, Section VIII, Division 2: Alternative Rules. In (Vol. ASME BPVC.VIII.2-2017): ASME International.

Bhagyashri, U., and Mishra, H., 2015. A review on design and analysis of pressure vessel. *International Journal of Advance Research and Innovative Ideas in Education, 1*(2), 348-353.

Dhalla, A. K., and Jones, G. L., 1986. ASME code classification of pipe stresses: A simplified elastic procedure. *International Journal of Pressure Vessels and Piping, 26*(2), 145-166. doi:https://doi.org/10.1016/0308-0161(86)90038-4

Hechmer, J. L., and Hollinger, G. L. (1998). 3D Stress Criteria Guidelines for Aapplication. In *Welding Research Council Bulletin* (Vol. WRC - Bulletin 429): Welding Research Council.

Olszewski, A., Wodtke, M., and Wójcikowski, A., 2018. FEM Analysis and Experimental Tests of Rigid Riser Hanging System. *Polish Maritime Research, 25*(2), 108-115. doi:10.2478/pomr-2018-0061

Peters, D. T., Haley, K., and Padmala, A. (2013). *ASME Section VIII-Division 3 Example Problem Manual*.

Sharifi, S., Gohari, S., Sharifiteshnizi, M., Alebrahim, R., Burvill, C., Yahya, Y., and Vrcelj, Z., 2018. Fracture of laminated woven GFRP composite pressure vessels under combined low-velocity impact and internal pressure. *Archives of Civil and Mechanical Engineering, 18*(4), 1715-1728. doi:10.1016/j.acme.2018.07.006

Sharifi, S., Gohari, S., Sharifiteshnizi, M., and Vrcelj, Z., 2016. Numerical and experimental study on mechanical strength of internally pressurized laminated woven composite shells incorporated with surface-bounded sensors. *Composites Part B: Engineering, 94*, 224-237. doi:10.1016/j.compositesb.2016.03.020

Sunil Kumar, D., and Suhas, B., 2016. Design and Evaluation of Pressure Vessel as per ASME Section VIII Division 2. *International Journal of Innovative Research in Science, Engineering and Technology, 5*(10), 17989-18002.

Thakkar, B. S., and Thakkar, S. A., 2012. Design of Pressure Vessel Using ASME Code, Section VIII, Division 1. *International Journal of Advanced Engineering Research and Studies, 1*(2), 228-234.

Afyon Kocatepe Üniversitesi Uluslararası Mühendislik Teknolojileri ve Uygulamalı Bilimler Dergisi

Afyon Kocatepe University International Journal of Engineering Technology and Applied Sciences

AKÜ IJETAS Vol **2**(2019) Haziran (46-54 s) AKU J.Eng.App.Sci. **Vol 2** (2019) June (46-54 pp)

Araştırma Makalesi / Research Article

Mobil Haberleşme Combo Antenleri için Genişband Elektromanyetik Sönümlendirici

Niyazi K. Uluaydın[1], Selim Ş. Şeker [2]

[1] *Electrical and Electronics Engineering Department, Engineering Faculty, Boğaziçi University, Bebek, Istanbul, Turkey.*
[2]*Electronics Engineering, Faculty of Engineering and Natural Sciences, Üsküdar University, Altunizade Mh. Haluk Türksoy Sk. No:14, Üsküdar, İstanbul, Turkey.*
e-posta:korkut.uluaydin@boun.edu.tr, selim.seker@uskudar.edu.tr

Geliş Tarihi:30.04.2019 ; Kabul Tarihi:30.05.2019

Anahtar kelimeler
5J; 4J; 3J; Elektromanyetik Dalga Sönümleme; Baz İstasyonu; Mobil Haberleşme.

Özet

Mobil Şebeke İşletmecileri (MŞİ) farklı jenerasyon mobil teknolojilerinin farklı sıklık aralıklarında düzgün çalışmasını sağlamak zorundadırlar. Öte yandan, elektromanyetik (EM) kirlilik, ki daha çok mobil telefonlar ve mobil baz istasyonları tarafından kaynaklanır, toplumda sağlık kaygıları yaratmaktadır. Bu sebeple, MŞİler birçok anten çubuğunu tek bir radomeda saklayan combo antenleri kullanmaktadırlar. Bu çalışmada, araştırmacılar mobil şebeke baz istasyonu combo antenleri için genişband bir elektromanyetik sönümlendirici önermektedirler. Araştırmacılar bunun için çok katmanlı Jaumann sönümlendirme (JS) ve Salisbury ekranlama prensiplerini mikrometrik ve milimetrik grafit ve nanometrik karbon siyahı malzemeleri üzerine uygulamıştır. Buna ek olarak, ileri teknoloji gümüş ve nikel kaplanmış seramik kürecikler de sönümlendirici kalınlığını azaltmak üzere EM saçılımını arttırmak ve sönümlenmeyi iyileştirmek için kullanılmıştır. Son olarak, gümüş kaplı naylon kumaş da salisbury ekranlamasının en yenilikçi şekli ile sönümlendiriciye dik iplikçiklerle yerleştirilerek ısınma sorununu çözmüştür. Laboratuvar testlerinden sonra, sönümlendirici sahada test edilmiştir. Doksan milimetre kalınlığındaki bir sönümlendirici uygulaması istenmeyen radyo frekans (RF) sinyalini mobil şebekenin çalışmasını engellemeden ve anten yayınım şeklini değiştirmeden 18 dB azalmiştir. Bu tip bir sönümlendirici istenmeyen elektromanyetik dalgaların yayılmasını engellemeye yardımcı olabilir ve bütün mobil şebeke RF gürültüsünü ve EM kirliliğini her iki yayın yönünde de azaltabilir.

A Broadband Electromagnetic Absorber for Mobile Telecommunication Combo Antennas

Keywords
5G; 4G; 3G; Electromagnetic Wave Absorption; Base Station; Mobile Telecommunication.

Abstract

Mobile network operators (MNOs) have to sustain the interworking of different generations of mobile technologies in different frequency bands. On the other hand, electromagnetic (EM) pollution, which is caused mainly by the mobile devices and mobile network base stations, also raises public health concerns. Thus, MNOs use combo antennas, which encapsulate multiple antenna rods in a single radome. In this study, the authors propose a broadband electromagnetic absorber for the mobile network base station (BS) combo antennas. They have merged the multi-layer Jaumann absorber (JA) and Salisbury screen principles along with the merits of off-the-shelf micrometric and millimetric graphite and nanometric carbon black. Advanced silver and nickel coated nanometric cenospheres were also used to decrease the absorber thickness and to improve EM scattering and absorption. And finally, silver fabric was used as the salisbury screen with novel perpendicular threads into the absorber body as heat sink. After the laboratory tests, the absorber has also been tested in the field. The application of the absorber has reduced the unwanted radio frequency (RF) signal around 18 dB in the tested frequency range without any network affecting disturbances or without any noticeable antenna pattern deformation with only a thickness of ninety millimeters. Such an absorber may also help containing the unwanted spread of electromagnetic waves from BS antennas; and, in return, decrease the overall mobile network RF noise and electromagnetic pollution both in uplink and downlink frequency bands.

© Afyon Kocatepe Üniversitesi

1. Introduction

The mobile telecommunication has become an essential part of our daily life. With the increasing number of users, the mobile network operators (MNOs) have to use more mobile base stations (BS). The mobile technology has also advanced parallel to increasing demands of users. Thus, MNOs have deployed newer mobile technologies over the existing ones further increasing the number of BS antennas broadcasting in different spectrum bands [1]. On the other hand, this increasing use of wireless technologies has raised public health concerns [2-14].

There has been extensive research performed on the EM shielding and absorption [7-21]. Compact devices with multiple EM transmitters are available, and there can be EM interferences between them and with other devices. So, it becomes more important to contain the unwanted signals, and the EM absorbers gain popularity [9].

In our BS case, the urban sites are generally co-located with other MNOs. MNOs also have to use more than one mobile technology because of financial, regulatory, and compliance reasons. Therefore, there are clusters of antennas in each urban site. These clusters may interact with each other and with other antennas on different sites negatively affecting the performance of the overall mobile radio network.

The MNOs use different technologies in different parts of the spectrum. A single BS antenna does not necessarily cover the entire spectrum, and in general, different antennas are used to broadcast in different bands. For these reasons, the number of antennas per urban site dramatically increases. So, the MNOs use combo antennas, where three or more antenna pairs are encapsulated within a single radome. In order to avoid these disruptive interactions, EM absorbers can be used to limit the spread of unwanted EM signals. Such an EM absorber should, therefore, be able to operate over the range of all those frequencies that the combo antenna operates [1].

Materials with high enough complex dielectric coefficients are preferable for the absorption of the electromagnetic (EM) energy and for converting it into heat. These materials are used for wide-band EM energy absorption applications such as in anechoic chambers [22]. But in mobile BS case, there are different constraints for an EM absorber such as wind load, weight, thickness, and cost.

In this study, authors propose a broadband EM absorber, which can operate with multiple rod combo antennas and upcoming massive multi-input multi-output (MIMO) 5th generation mobile telecommunication antennas without overheating.

2. EM Absorption

There are two fundamental loss mechanisms in shielding theory: reflection loss and absorption loss. An EM plane wave arriving on a uniform slab obstacle can undergo reflection, absorption, and transmission. When such a plane wave comes across the slab, the transmitted and the reflected parts of electrical and magnetic components are the same [7]. But there is a serious difference here to note that the primary transmission of the magnetic component occurs at the initial interface while the primary transmission of the electrical component occurs at the final interface. In other words, it is much easier to reflect the electrical component in the first boundary, and that makes dielectric absorption not an easy task, at all.

2.1 Magnetic and dielectric loss mechanisms

The electromagnetic radiation in mobile telecommunication spectrum can be absorbed by its dielectric and magnetic components. The absorber domain should be designed in order to allow the EM waves in, and attenuate them as the waves penetrate further. The waves will have propagation constant in the absorber domain as Equation 1:

$$\gamma = (j\omega\mu^* (\sigma + j\omega\varepsilon^*))^{1/2} \quad (1)$$

where μ* is the magnetic permeability; ε* is electrical permittivity; σ is the conductivity (1/m or "mhos/m"); ω is radial frequency, ω = 2πf (f frequency in Hz) [7]. The main factors affecting the absorption of the EM waves are the absorber domain complex permittivity (ε*= ε' - ε''), the complex permeability (μ*= μ' - μ''), and EM

impedance match, which is related with former two factors and the conductivity σ [7]. The real parts of the complex permittivity and permeability represent the energy storage capacity of the absorber domain, whereas the imaginary parts show the loss of electric and magnetic energy in the absorber domain [7]. Therefore, the ratio of imaginary to real part for the absorber material's permittivity and permeability shows the capacity of absorption for electric and magnetic parts, respectively.

2.2Salisbury screen mechanism

The Salisbury screen mechanism is a narrowband applicable shielding method working with the principle of out of phase cancellation of the incoming wave through a single absorber layer followed by a good conductor. In order to have the reflecting wave to be in totally out of phase with the incoming wave, the thickness of the absorber should be carefully arranged to the quarter wave effective inside the absorber. The propagating wave within the absorber will have the wavelength as such Equation 2:

$$\lambda = \frac{\lambda_o}{\sqrt{|\varepsilon||\mu|}} \qquad (2)$$

where λ_o is the wavelength in free space, and $|\varepsilon|$ and $|\mu|$ are the modulus of permittivity and permeability of the absorber material, respectively [10]. This mechanism can be applied within the range of 0.25-0.30 λ in practical applications with dielectric absorbers [10, 22].

2.3 Jaumann absorber mechanism

The JA uses the mechanism of multiple layers of absorbers tuned to return minimum reflection. The wave would attenuate both by the transmission through multiple absorber layers as well as the multiple in-bound reflections within these absorber layers. Another important property of JA mechanism is that the layers are arranged with increasing dielectric values focusing waves into the axis perpendicular to the absorbers' axis. This is a great benefit for the absorption of waves with different polarizations and incoming directions and provides a wider absorption range [10].

The JA layers are generally followed by a good conductor and the total thickness is arranged for the effective quarter wave length depth in order to benefit from the Salisbury screen mechanism. For a designated range of frequencies, this thickness can be arranged for the lowest operating, or the dominant frequency of operation of the Jaumann absorber, or any other preference in design [10, 23].

3. Material Development of Dielectric Absorbers

Our design steps included a narrowband absorber development followed by a broadband absorber development. We preferred a dielectric only absorber design in order keep our design simple and our cost low in order to fulfil our constraint set for the telecom mobile radio network.

3.1 Narrowband Absorber Development

We have chosen polyester free form acoustic sponge with open-cell structure as our matrix material. This material has the following advantages: low cost; ease of reach; easy to shape; easy to impregnate, and most importantly it comes in almost all sizes.

The designated frequency range greatly affects the size and dimensions of a narrowband absorber [23]. We have chosen micrometric, millimetric, and nanometric carbon as our base materials having good properties for impregnation. A micrometric and millimetric graphite (G) and nanometric carbon black (CB) mixture is prepared using a water-based binder; and, the matrix material is soaked with this mixture. So, having two different carbon materials with different properties, one can choose between the high thermal and electric conductivity of the graphite, and radiation absorption and electrical conductivity of carbon black [24].

We have made lab measurements on a Rohde&Schwarz ZVA 40 vector network analyser (VNA) using ridged microwave antennas from 2.3 to 2.6 GHz band with sweep on 1 MHz steps with time domain gating (Figure 1). The measurements

were all done in close proximity to resemble our field test conditions. Time domain gating used according to VNA vendor specification in order to avoid multipath reflections and wrap around energy release.

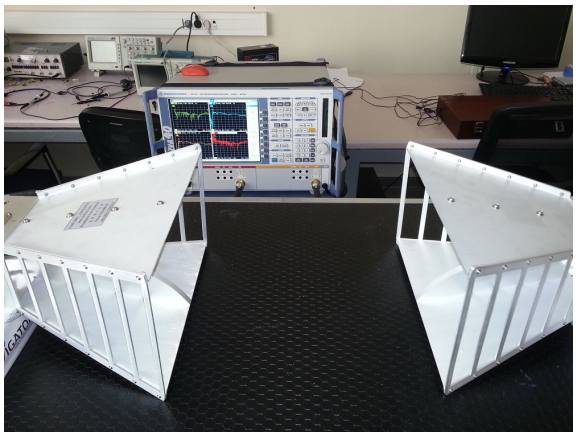

Figure 1. Measurement set-up with R&S ZVA 40 vector analyser with ridged horn antenna pair.

Using matrix sponge with planar and pyramid shapes and different mixtures, 1 set (5 pieces) and 1 set with Chebyshev pyramids (3 pieces) with increasing loading were prepared, respectively. The loading ratios for the planar set were as follows: 1%-0%; 1.5%-0%; 1%-1%; 1.5%-1%; 2%-1%, CB-G by weight. The loading ratios for the pyramidal set were as follows: 1%-0%; 1%-1%; 2%-1%, CB-G by weight. The pyramid shapes had λ/4 height tuned for 2.45 GHz at 3cm with 1 cm base thickness.

The first set has provided the benefits of a gradual dielectric change while the second set provided the benefits of gradual surface change. S_{11} and S_{22}values represent the reflection amounts back to transmitter while S_{12} and S_{21} values represent the transmission amounts in Figure 2, Figure 3, and Figure 4 [9,17]. The absorption (A) is related with the transmission (T) and the reflection (R) with the equation: A=1-R-T, where R and T can be determined by $R=|S_{11}|^2$ and $T=|S_{21}|^2$, respectively [17]. So, one should minimize both the reflection and the transmission values at the same time [25].

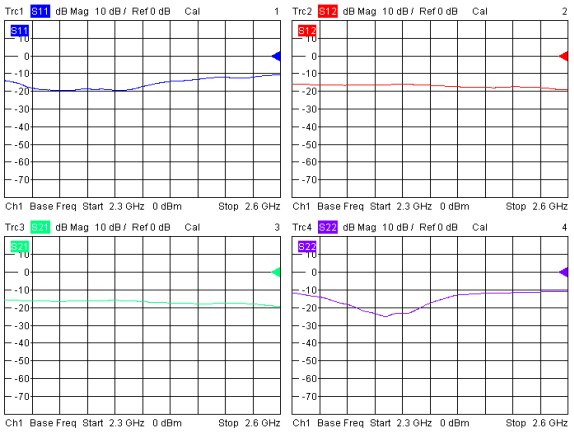

Figure 2.1% CB loaded flat layer.

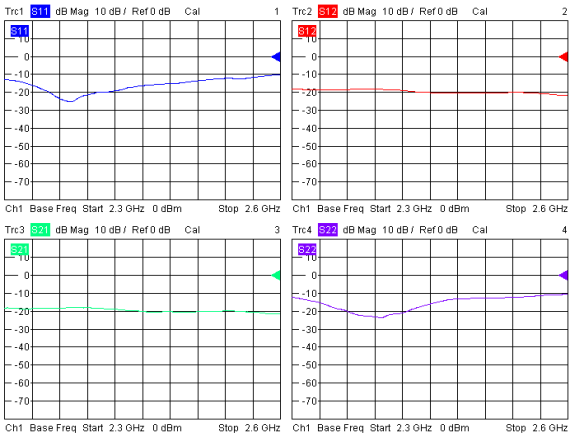

Figure 3.1% CB and 1% G loaded flat layer.

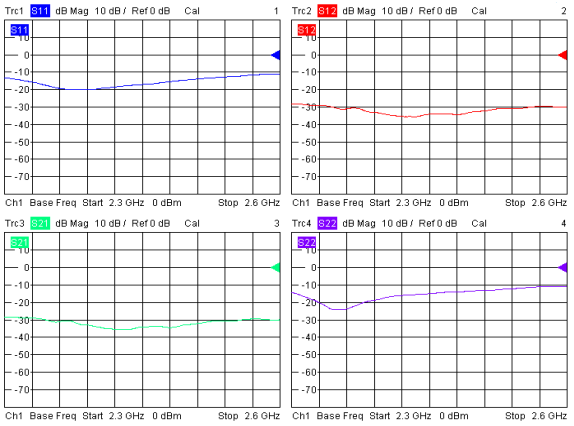

Figure 4.2% CB and 1% G loaded flat layer and Chebyshev pyramid structure together.

The 1% CB loaded flat layer (Figure 2) was approximately 3 dB better on the average than the nominal free transmission in S_{11} and S_{21}. The 1% CB and 1% G loaded layer (Figure 3) was approximately 5 dB better on the average than the nominal in S_{11} and S_{21}. The mutual effect of Chebyshev pyramids together with a flat layer was approximately 15 dB better on the average than

the nominal in S_{21} when both were 2% CB and 1% G loaded (Figure 4).

We have tested the Chebyshev pyramid model in a 5 kW commercial 2.45 GHz operating microwave (MW) oven.The material has shown good load properties minimizing the reflections back to magnetron. This test also demonstrated the importance of the homogeneity of the materials based on the observations of the temperature distribution after a short exposure (Figure 5). Non-homogeneous parts were hotter and one hot spot has also suffered thermal runaway. The commercial MW oven has also been used to test and the load/impedance match of the overall model.

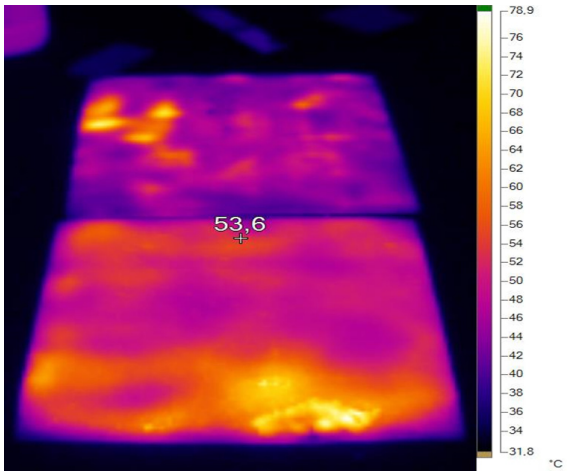

Figure 5. Thermal picture of pyramid absorbers in bottom-up formation in commercial MW oven after a short exposure (temperature scale in degrees Celcius).

3.2 Broadband Absorber Development

For a good broadband absorber performance, good attenuation should be attained while keeping a gradual change of dielectrics to avoid reflection of the electrical field in the designated frequency band. Having these two constraints in mind, a multilayer strategy and gradually changing dielectric constant with depth strategy was chosen at the same time. Other granular materials were used either to maximize the attenuation of the wave or to increase the scattering of the wave within the absorber matrix.

Combo antennas range from 700 MHz up to 3.5 GHz and can support 2nd, 3rd, and 4th generation mobile telecommunication technologies, concurrently. This can readily explain the need for the broad band performance. Another issue in the absorption performance is the source to absorber distance. Our absorber antenna distance falls in the near field range in our case.

Multiple layers with gradual change of dielectrics with nanometric CB and micrometric and millimetric graphite are used with our initial experience. Silver and nickel cenospheres were added between the layers to increase the scattering and increase magnetic attenuation, respectively.

CB provides attenuation across all frequencies. Its nanometric scale does not increase the conductivity of the composite material significantly, whereas micrometric and millimetric graphite pieces may add up to the conductivity, if used in high amounts. These two materials are used in layers in increasing amounts. Stacking the different layers, the best performance has been tuned by the help of commercial MW oven reflection measurements both for impedance match and minimum reflection. As a final surface, silver coated nylon mesh fabric was used as a flexible conductor with a shielding effectiveness of 66 dB at 900 MHz according to IEEE STD-299 (Figure 6).

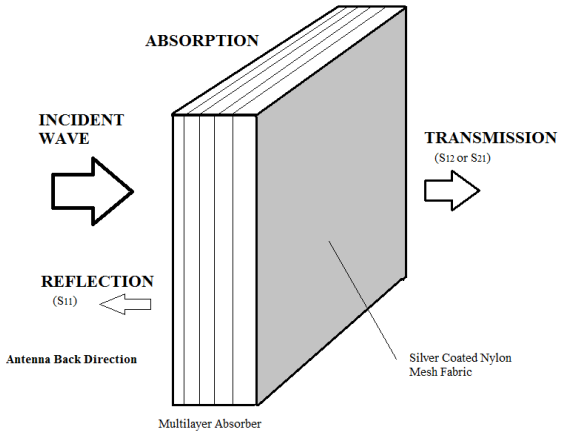

Figure 6. Illustrative absorber and its cross section with the mentioned material and their designated location.

The final absorber consisted of four layers: one flat (1% CB), two pyramidal layer (pyramids facing each other, 1%CB-1%G to 2%CB-1%G), and the final one cast with silver mesh fabric (2%CB-1%G+cenospheres+silver coated nylon threads perpendicular to wave front) (Figure 7).

Figure 7. The second layer and the fourth and final layer left-to-right.

3.3 Measurements and Field Tests

The final prototype was measured with the same set-up. The S_{11} was around 20 dB and the S_{21} was around 55 dB on the 1-10 GHz range (Figure 8, Figure 9). The shielding performance was around 20-30 dB less than expected because of the near field positioning compared to IEEE STD-299 values for the silver coated mesh fabric [25].

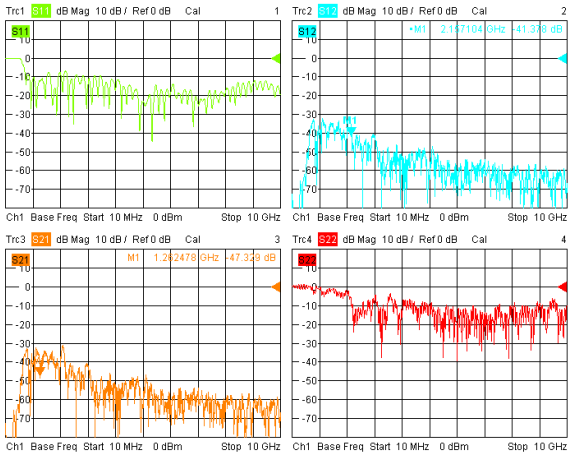

Figure 8. The S-parameter measurement of the prototype.

Then the prototype has been tested in the field with an MNO, which wanted to test the absorber in the front lobe of the antenna in order to evaluate the performance under harder conditions. The absorber was positioned on the radome itself without any space in between. The voltage standing wave ratio (VSWR) performance was used to assess the load match. The measurements were recorded with drive tests before and after the montage of the absorber to the antenna.

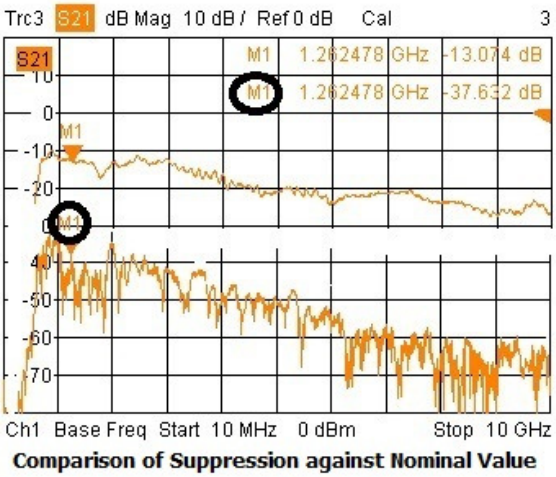

Figure 9. Measurement marker at 1.26 GHz with 24.5 dB suppression.

The initial test drive was taken without any absorber (Figure 10) to observe normal propagation of the signal. The average suppression of the front lobe of the antenna was around 18 dB (12-28 dB) in 900 MHz - 1800 MHz - 2150 MHz range.

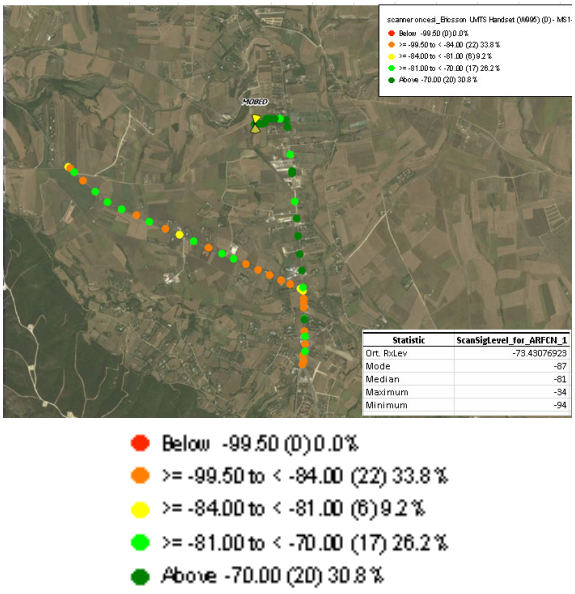

Figure 10. The first drive test to measure nominal signal strength and its related percentage in colour legend.

This performance was way over the mobile operator's 6 dB expectation (Figure 11). There was not any VSWR related alarm on the BS operation and maintenance system.

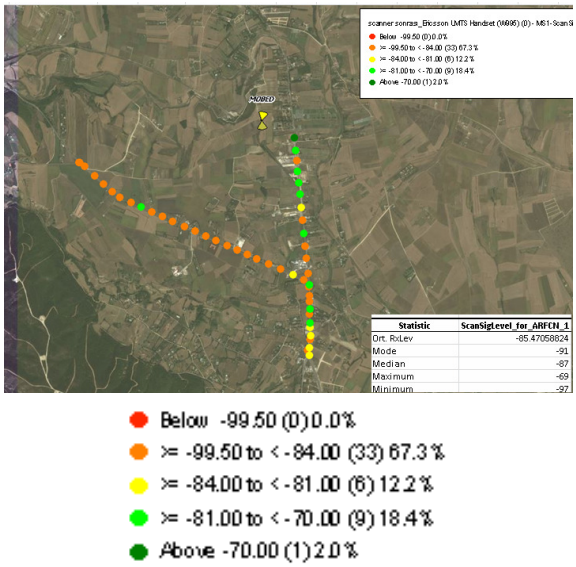

Figure 11. The second drive test results to measure the signal strength through the absorber and its related percentage in colour legend.

4. Results and Discussion

Open cell polyester matrix with CB and graphite of appropriate size was an efficient and sufficient solution for suppressing the unwanted back and side lobe signals of mobile telecommunication combo antennas. Open cell structure of polyester acoustic sponge was easily impregnatable with materials up to 100 micrometer without loss of homogeneity. Our selection of CB and graphite provided us with the availability of off-the-shelf industrial materials. Although this combination does not necessarily give the best absorption per thickness performance [7-10;15-17], it was cost-wise very successful together with the matrix selection. The disadvantage in thickness was partially related with the open cell structure of our matrix since even after loading the matrix still contained void areas. If loading ratios were increased even higher, then there would be more of the inhomogeneity related issues. Thus, we have utilized nanometric nickel and silver coated cenospheres in between layers to increase the scattering and magnetic attenuation to contain the thickness related issue.

The absorber layers were light and flexible. The final layer was supported with a silver coated nylon fabric to resemble the good conductor effect. The total multilayer structure still kept its flexibility, though. This was a great advantage over the wider area of combo antennas' surfaces.

The field performances were slightly less than the laboratory measurements. There are two details to be mentioned. Firstly, the shielding and absorption performances degrade in very close proximity [17]. Secondly, the antenna absorber interaction was in the near field, and one could expect capacitive effects. Thus, we believe capacitive effects and frontal lobe testing could have lowered the field performance with higher power output of the antenna.

The field test also revealed three distinct advantages. Firstly, the absorber can withstand even the front radiation of telecommunication antenna without any thermal runaway. The second advantage is that a lower noise level will either improve the radio network quality or increase the frequency reuse pattern, on which mobile network planning is mainly based. The third and final one is in the uplink telecommunication channel part, where unrelated mobile terminal signals will no longer be received by the back lobe of the antenna. In 3rd and 4th generation mobile radio technologies, the absorber would also lessen the unnecessary breathing cell feature utilization. This, in turn, serves the customer masses in front of the antenna with a spectrum efficient focus providing higher data throughput by the second advantage. In the 5th generation mobile telecommunications, the absorber can handle the immense power of massive MIMO antennas and suppress the backlobe EM pollution.

5. Conclusion

As a result of this study, one may deduct that the mobile radio networks may benefit an average noise suppression of 9-18 dB by the mass utilization of such absorbers.

The prototype lessens the mobile telecom industry's one of the hardest challenges in radio network optimization. It can be used for optimum performance in urban areas between coverage and quality in all available spectrums concurrently, where 80% of the whole data and speech traffic take place.

For our future studies, we are planning to investigate different ways of utilizing nanometric cenospheres of nickel, copper and silver coatings [22]. Ferromagnetic material addition to the absorber looked promising to absorb the magnetic component of the antenna radiation and to further decrease the overall energy spread on back-lobe [26].

Acknowledgements

The authors would like to thank Boğaziçi University for supporting this study as part of the scientific research project BAP-9860.

6. References

[1]Mukherjee, S., 2014. Analytical Modeling of Heterogeneous Cellular Networks. 1st ed., Cambridge University Press, 20-30.

[2]Ibey, B.L.,P. B. Ledwig, Roth, C.C.,et al., 2016. Cellular effects of acute exposure to high peak power microwave systems.*Morphology and toxicology, Bioelectromagnetics*, 37, **1**, 141-151.

[3]Calvente, I., Núñez, M. I.,Pérez-Lobato,R. et al., 2016. Does exposure to environmental radiofrequency electromagnetic fields cause cognitive and behavioural effects in 10-year-old boys? *Bioelectromagnetics*, 37, **1**, 25-36.

[4]Diao, Y., He,Y.,Leung,S.-W. et al., 2016. Detailed modeling of palpebral fissure and its influence on SAR and temperature rise in human eye under GHZ exposure.*Bioelectromagnetics*, 37, **4**, 256-263.

[5]Corre,Y., Plets,D.,Varsier,N. et al., 2015. A novel methods to assess human population exposure induced by a wireless cellular network.*Bioelectromagnetics*, 36, **6**,451-463.

[6]Dlugosz,T., 2015. Bioelectromagnetic effects measurements – SAR and induced current.*Bio-Medical Materials and Engineering*, 25, 1-7.

[7]Chen, L.,Ding,J., Li,Q. et al., 2016. Open-cell phenolic carbon foam and electromagnetic interference shielding properties.*Carbon*, 104, 90-105.

[8]Chung,D. D. L.,Hong,X., 2017.Carbon nanofiber mats for electromagnetic interference shielding.*Carbon*, 111,529-537.

[9]Bailly,C., Danlée,Y., Huynen,I., 2014. Thin and flexible multilayer polymer composite structures for effective control of microwave electromagnetic absorption.*Composites Science and Technology*, 100, 182-188.

[10]Abbas,Z., Hashim,M.,Idris,F. M. et al., 2016. Recent developments of smart electromagnetic absorbers based polymer-composites at gigahertz frequencies.*Journal of Magnetism and Magnetic Materials*, 405, 197-208.

[11]Chen, Y.,Su,C., Yuan, Q. et al., 2016. Electromagnetic Shielding Performance of Nickel-Plated Expanded Graphite/Wood Fiber Composite.*BioResources*, 11, **2**, 5083-5099.

[12]Dhawan, R., Kumar,R.,Kumari,S. et al., 2015. Mesocarbon microsphere composites with Fe3 O4 nanoparticles for outstanding electromagnetic interference shielding effectiveness.*Rsc Advances*, 5, **54**, 43279-43289.

[13]Jiang, W., Sun,M.,Wu,F. et al., 2016. A self-assembly method for the fabrication of a three-dimensional (3D) polypyrrole (PPy)/poly (3, 4-ethylenedioxythiophene) (PEDOT) hybrid composite with excellent absorption performance against electromagnetic pollution.*Journal of Materials Chemistry C*, 4, **1**,82-88.

[14]He, J. Z.,Wang,X. X.,Zhang, Y.L. et al., 2016. Small magnetic nanoparticles decorating reduced graphene oxides to tune the electromagnetic attenuation capacity.*Journal of Materials Chemistry C*, 4, **29**, 7130-7140.

[15]Ding, Y., Wang,C.,Zhu, J. et al., 2016. Multifunctional three-dimensional graphene nanoribbons composite sponge.*Carbon*, 104, 133-140.

[16]Micheli, D., Pastore,R.,Vricella, A. et al., 2016. Ballistic and electromagnetic shielding behaviour of multifunctional Kevlar fiber reinforced epoxy composites modified by carbon nanotubes.*Carbon*, 104, 141-156.

[17]Azizi,H., Ghasemi, I.,Zakiyan,S.E., 2017. Influence of chain mobility on rheological, dielectric and electromagnetic interference shielding properties of poly methyl-methacrylate composites filled with

graphene and carbon nanotube.*Composites Science and Technology*, 142, 10-19.

[18]Qi, K., Wang, Y., Yuan, X., 2016. Stealth mechanism analysis of the Phase-Modulated Surface.*IEEE InProgress in Electromagnetic Research Symposium (PIERS)*, Shangai, 3726-3729.

[19]Asadchy,V.S.,Ra'di,Y.,Tretyakov,S.A., 2013.Total absorption of electromagnetic waves in ultimately thin layers.*IEEE Transactions on Antennas and Propagation*, 61, **9**, 4606-4614.

[20]He,J.Z., Wang,X.X., Zhang,Y.L. et al., 2016. Small magnetic nanoparticles decorating reduced graphene oxides to tune the electromagnetic attenuation capacity.*Journal of Materials Chemistry C*, 4, **29**,7130-7140.

[21]Reynolds,C.B., Saito, R.,Ukhtary,M. S. , 2016. Absorption of THz electromagnetic wave in two mono-layers of graphene.*Journal of Physics D: Applied Physics*, 49, **19**, 195306.

[22]Cheng, X.L.,Hu,Y.J.,Zhang,H.Y. et al., 2011. The Influence of Electroless-Silver Coated Cenosphere Powders on the Electromagnetic Shielding Interference Effectiveness and Mechanical Properties of the Silicone Rubber.*Advanced Materials Research*, 152, 1360-1365.

[23]Yan, N.,Ying,W., Yong-Zhi,C. et al., 2013. Design and Experiments of Low-frequency Broadband Metamaterial Absorber based on Lumped Elements.*Acta Physica Sinica*, 62, 1-5.

[24]Lins, P.R., Rocha,J.S.,da Silva,E.F. et al., 2005. Characterization of electromagnetic radiation absorber materials.*Microwave and Optoelectronics, SBMO/IEEE MTT-S Int. Conf.*, Brasilia, 326-329.

[25]Cerezci, O., Yener, S.C., 2016. Material analysis and application for radio frequency electromagnetic wave shielding. *Acta Physica Polonica A*, 129, **4**, 635-638.

[26]Hong,T., Jiang,W., Wang, F. et al., 2014. Radar cross section reduction of wideband antenna with a novel wideband radar absorbing materials.*IET Microwaves, Antennas & Propagation*, 8, **7**,491-497.

AFYON KOCATEPE ÜNİVERSİTESİ ULUSLARARASI MÜHENDİSLİK TEKNOLOJİLERİ ve UYGULAMALI BİLİMLER DERGİSİ

Afyon Kocatepe Üniversitesi
Ahmet Necdet Sezer Kampüsü
Teknoloji Fakültesi
AFYONKARAHİSAR
Tel: +90 272 228 14 46
Belgegeçer: +90 272 228 14 49
E-posta: ijetas@aku.edu.tr

www.ijetas.aku.edu.tr